申 报	系列：教学科研型
	专业：机械工程
	职称：副教授

业绩成果材料

（申报人的业绩成果材料包括论文、科研项目、获奖以及其他成果等）

单　位（二级单位）　工程学院

姓　名　黄光文

材料核对人：　　　　　　单位盖章：

核对时间：

华南农业大学制

目　录

一、教学研究业绩

二、科研项目

三、论文、著作等

2.以通讯作者发表本专业论文情况

四、科研成果

1.知识产权

1.1.专利授权证书：适用农业机械装卸转场的轨道运输机及

五、其他业绩

1.指导学生学科竞赛

2.个人荣誉

3.社会服务

华南农业大学文件

华南农教〔2025〕57号

关于公布华南农业大学2025年度校级本科教学质量与教学改革工程项目立项名单的通知

各学院、部处、各单位：

根据《关于开展2025年度校级本科教学质量与教学改革工程项目申报工作的通知》精神，经项目负责人申请、所在单位推荐、本科生院审核、学校组织专家评审和公示（无异议）等程序，决定立项“善境伦理学与风景园林专业实践教学深度融合的探索与实践”等127个项目为2025年度校级本科教学改革项目，立项“筑基·焕新·赋能：食品质量与安全专业‘新工科’建设暨工程教育认证提质创新工程”等52个项目为2025年度校级本科质量工程项目。具体名单见附件。

请各项目负责人按照项目建设任务及要求，及时开展各项改

革工作；各单位要切实履行项目建设主体责任，加强对项目建设的督促、指导，以确保项目建设任务高质量完成。

特此通知。

附件：1. 2025年度校级本科教学改革项目立项名单
2. 2025年度校级本科质量工程项目立项名单

华南农业大学
2025年10月14日

（联系人：孙齐胜；电　话：85288020）

公开方式：主动公开

华南农业大学党政办公室　　2025年10月15日印发

2025年度校级本科教学改革项目立项名单

序号	项目编号	项目名称	级别	所在单位	项目负责人	项目组成员
1	JG2025001	善境伦理学与风景园林专业实践教学深度融合的探索与实践	重点	林学与风景园林学院	翁殊斐	高伟、李自若、李剑、冼丽铧
2	JG2025002	基于“AI赋能·科创融合”《中药鉴定学》教学改革探索与实践	重点	林学与风景园林学院	李雁群	白玫、谭建文、何韩军、李镇魁
3	JG2025003	基于OBE理念的“数字赋能、思政融合、产教协同”的《制药设备与工艺设计》课程育人模式研究与实践	重点	材料与能源学院	林雅铃	宋高鹏，聂燕芳，霍理坚
4	JG2025004	面向智慧国土空间规划的《区域规划》　数智化教学改革	重点	公共管理学院	李玮	高艳梅、孙传谆、武侠、刘卓君
5	JG2025005	基于批判性思维培养的公共管理类专业课“GenAI+”教学模式探索——以投资学课程为例	重点	公共管理学院	李韵婷	贾海薇、段 静、周丽云、杨明旭
6	JG2025006	“AI赋能-人机协同”课堂互动重构研究—以C语言课程为例	重点	数学与信息学院、软件学院	彭利民	李双娟，杨磊，吴理华，司国东
7	JG2025007	思政引领和业财融合导向的《中级财务会计》智慧教学改革与实践	重点	经济管理学院	陈晓敏	陈艳艳，牟小容，何艳玲
8	JG2025008	基于智能设备与线上平台的HIIT混合式体育教学创新设计与实践	重点	体育教学研究部	单宇	麦粤徽、张波、吕立、张晓萍
9	JG2025009	“AI+专业知识库”驱动的生态学实验创新设计教学：批判思维培养与实践范式应用	重点	资源环境学院	赵本良	章家恩、余光伟、危晖、李荣华
10	JG2025010	数字孪生与AI融合的《动物组织学与胚胎学》课程体系数智化升级与实践	重点	兽医学院	梁晓欢	马勇江、张媛、叶亚琼、李冰心
11	JG2025011	融合科学家精神与科研思维的《细胞生物学》“双核育人”改革与实践	重点	动物科学学院	冯敏	邓小娟、杨婉莹、胡豆豆、易辉玉
12	JG2025012	《食品标准与法规》创新能力培养体系的构建与应用研究	重点	食品学院	林晓蓉	郑倩望、李梦婷
13	JG2025013	轻量化AI驱动大学英语听说教改：POA-SOLO双轨分级训练模式	重点	外国语学院	王莹	钟志英、苏君、黄净、王世龙
14	JG2025014	基于深度学习的大学生高阶思维能力培养的教学模式改革与实践研究—以《作物育种学》为例	重点	农学院	陈婷婷	马启彬、张雷、黄君、夏辉
15	JG2025015	数智AI赋能高校形象设计教学“三化五全”育人模式的探索	重点	艺术学院	郑丽娜	王羊羊、郝丽、米平平、李若衡
16	JG2025016	《车用电机及控制技术》课程“仿真驱动-问题探究”教学模式改革与实践	重点	工程学院	吴双龙	李庆、林彩霞、肖博一
17	JG2025017	数智化转型中《无机及分析化学》课程思政与 AI 赋能教学融合路径探索	重点	材料与能源学院	高琼芝	高琼芝，刘英菊，刘海峰，张声森，杨思源
18	JG2025018	校地协同视域下环境工程本科人才实践能力培养路径优化	重点	资源环境学院	林云琴	陈杨梅　梁瑜海　郑芊　赖文威
19	JG2025019	“产教+科教”双融合下设计类专业创新型复合人才培养模式探索	重点	艺术学院	陈薇薇	黄鑫、冯悦、杨翠钰、李春阳
20	JG2025020	AI赋能高校精准化学业指导路径研究	重点	本科生院	倪妙珊	吴银宝、王金凤、李晨光、张佳琛
21	JG2025021	智慧教学背景下OBE导向的英语专业实践类课程的转型与重构	重点	外国语学院	朱婕	严晓蓉、苏君、林绿、杨敏
22	JG2025022	与极飞科技产教融合的人工智能人才培养探索	重点	电子工程学院（人工智能学院）	熊万杰	邓小玲、徐海涛、刘景峰、董昕

44	JG2025044	野生动物与自然保护区管理专业（长隆班）实践课程创新研究	自筹	林学与风景园林学院	佟富春	彭友贵、潘新园、刘方明、邓皓洋
45	JG2025045	现象学视角下的风景园林专业大一设计基础课程教学改革	自筹	林学与风景园林学院	林毅颖	胡盛劼、李自若、张玉竹、徐锐
46	JG2025046	城市更新背景下风景园林规划与设计 I 课程教学改革—— “学生-技术-项目”三位一体教学模式研究	自筹	林学与风景园林学院	古德泉	夏宇、李剑、黄家平、江帆影
47	JG2025047	AI赋能促进《生物统计学》深度 学习的教学新模式探索	自筹	林学与风景园林学院	林元震	骈瑞琪、李青粉
48	JG2025048	新农科背景下技术赋能与能力导向融合的实验教学改革——以《药用植物生态学实验》为例	自筹	林学与风景园林学院	龙凤玲	赵倩、马玲
49	JG2025049	基于“docker+WSL”轻量化构架的混合教学模式在《基因组学与生物信息学实验》中的应用	自筹	园艺学院	曾灶海	夏瑞、郝彦伟、方倩、徐婧
50	JG2025050	AI音乐赋能园艺疗法与大学生心理健康教育的融合研究	自筹	园艺学院	李伟	杨向晖、苏蔚、张大山、李坤阳
51	JG2025051	新农科背景下基于三茶融合视角的思政教学课程融合与路径探索——以《茶艺与茶文化学》为例	自筹	园艺学院	李丹	张凌云、晏嫦妤
52	JG2025052	《智慧树平台与影像病例库协同驱动的影像学教学创新与实践 —— 基于兴趣激发与学习效果双维度优化》	自筹	兽医学院	陈昪蕾	廖建昭、陈义洲、傅叶琪
53	JG2025053	通过临床案例学习解剖学消化系统下消化道章节	自筹	兽医学院	许丹	剡海阔、王衡、于静、吴志文
54	JG2025054	人工智能赋能的家畜行为学课程教学改革与实践	自筹	动物科学学院	张玲娜	王丽娜、谭成全
55	JG2025055	安全心理学视域下高校科研实验室安全管理的干预机制与路径研究	自筹	资源环境学院	谢洁芬	郑少燕、黎平、林媛、 陈超
56	JG2025056	面向全栈化与智慧化的《网络GIS》课程教学体系优化研究与实践	自筹	资源环境学院	谢健文	谢健文 陈永康 吴小芳 钟晓兰 袁兰
57	JG2025057	基于实景三维中国建设背景下测绘综合应用实习教学改革	自筹	资源环境学院	陈俊林	姚朝龙、万欢、陈鹏
58	JG2025058	基于创新能力培养的《水产动物营养与饲料》课程教学改革与实践	自筹	海洋学院	陈世俊	甘炼、谢帝芝、吴坤、徐超
59	JG2025059	数智化背景下《海洋环境化学》的教学改革探索与实践	自筹	海洋学院	黄玉妹	王俊、公晗、钟丽香、张梦环
60	JG2025060	人工智能赋能基因工程智慧教学模式改革	自筹	生命科学学院	陈亮	易继财、周海、刘振兰
61	JG2025061	AI赋能“新农科”背景下植物生理学课程改革的探索与应用	自筹	生命科学学院	刘宇婷	张雪莲、刘太波、刘慧丽
62	JG2025062	学科交叉融合助推卓越农林人才培养 --以传感器与检测技术课程为例	自筹	工程学院	黄培奎	胡炼、赵润茂、舒灿伟、何杰
63	JG2025063	基于AI赋能的《机械制造基础》课程“三位一体”贯通式教学改革与实践	自筹	工程学院	曹亚超	王红军、刘天湖、王慰祖、甄文斌
64	JG2025064	“AI+教学”模式下控制理论课程思政教学体系构建与实践	自筹	工程学院	邢航	李继宇、漆海霞、施琳琳、金济
65	JG2025065	基于OBE理念的混合AI智慧教学模式在机械制造工艺学和夹具设计课程中的应用与实践探索	自筹	工程学院	黄光文	李君、辛伯来、黄成杰、曹亚超
66	JG2025066	科研反哺教学在《食品包装学》课程中的探索与实践	自筹	食品学院	葛文娇	岳淑丽、刘涛、曹黎明、向红
67	JG2025067	虚拟仿真实验技术在“食品微生物检验实验”教学中的应用探索	自筹	食品学院	邹苑	王丽、郑倩望
68	JG2025068	城市更新导向的智能数字化城市设计课程教学体系改革研究	自筹	水利与土木工程学院	屈寒飞	韦未，陈晓佳、陈乃华、许媛媛

华南农业大学文件

华南农教〔2024〕7号

关于公布华南农业大学2023年度课程思政示范项目建设名单的通知

各学院、部处、各单位:

根据《华南农业大学课程思政实施方案》(华农党发〔2022〕26号)精神和《关于开展2023年度校级课程思政示范建设项目申报工作的通知》要求,学校组织开展了2023年度课程思政示范项目评选工作。

经项目负责人申请、所在单位遴选推荐、学校组织专家评审、校内公示等程序,决定立项建设华南农业大学2023年度课程思政示范项目125项,其中包括工程学院等课程思政试点学院3个、农学专业课程思政教学示范团队等课程思政示范团队7个、《电机学》等课程思政示范课程24门、《“数值分析”第四章第一节拉格朗日插值法》等课程思政示范课堂31个、《现实主义电影:

从意大利“新现实主义”到当下华语电影中的“温暖现实主义”》等课程思政典型案例60个（名单详见附件），现予以公布。

本次立项的示范项目建设期至2025年12月，建设期内示范项目原则上不允许更换负责人或变更项目团队成员。各项目团队要严格按照项目建设任务及要求及时开展工作，加快推进课程思政改革，确保高质量完成建设目标。

请各学院充分认识课程思政改革的重要意义，认真贯彻《华南农业大学课程思政实施方案》，加强对教师的相关培训、指导、引领和支持，带动教师全员积极参与课程思政教学改革，持续深入抓典型、树标杆、推经验，全面提升本科人才培养质量。

附件：华南农业大学2023年度课程思政示范项目建设名单

华南农业大学
2024年1月21日

公开方式：主动公开

华南农业大学党政办公室　　2024年1月23日印发

附件

华南农业大学2023年度课程思政示范项目建设名单

序号	**类别**	**项目名称**	**单位**	**项目负责人**	**团队成员（不含负责人）**
kcsz2023001	试点学院	课程思政试点学院	工程学院	李　君	
kcsz2023002	试点学院	课程思政试点学院	植物保护学院	闫笑久	
kcsz2023003	试点学院	课程思政试点学院	食品学院	魏剑波	
kcsz2023004	示范团队	农学专业课程思政教学示范团队	农学院	刘自强	马启彬、王少奎、周玉亮、王小龙、王兰、冯发强、吴锦文、汪文毅
kcsz2023005	示范团队	集成电路课程群课程思政示范团队	电子工程学院（人工智能学院）	刘洪山	谢家兴、梁亨茂、代秋芳、罗霞、王建、张宇、赵懿琨
kcsz2023006	示范团队	以农史教育为特色的中国史课程思政教学团队	人文与法学学院	刘玲娣	杨品优、赵艳萍、衷海燕、王福昌、翟麦玲、周晴、余格格、陈志国
kcsz2023007	示范团队	《大学数学》课程思政示范团队	数学与信息学院、软件学院	杨德贵	肖莉、何婧、付银莲、李凤、周燕、杨志程、丁仕虹、夏英俊、李朗

kcsz2023078	典型案例	基于“三位一体”目标导向的食品分析及实验课程思政教学实践研究——以“酸度的测定”为例	食品学院	温　棚	徐振林、 沈玉栋、徐小燕、杨金易、肖治理、 罗林
kcsz2023079	典型案例	感悟生命 追寻价值—大学生生命教育	海洋学院	苏　婉	
kcsz2023080	典型案例	《植物分类与标本制作技术》实验课程 —— “腊叶标本的制作”思政教学案例	基础实验与实践训练中心	郑明轩	
kcsz2023081	典型案例	免疫检测技术“课程思政”教学案例	食品学院	李向梅	雷红涛、徐振林、沈兴
kcsz2023082	典型案例	《跨文化交际》Chapter 12 Barriers and Bridges 12. 1 Barriers in Intercultural Communication	外国语学院	李　雅	
kcsz2023083	典型案例	“小”药片蕴含“大”民生——湿法制粒压片制备阿司匹林片	材料与能源学院	胡　洋	倪春林、周武艺、霍理坚、高永峰
kcsz2023084	典型案例	《机械制造工艺学》第一章第一节：机械制造工程学科的发展	工程学院	黄光文	
kcsz2023085	典型案例	生涯思政双融双促，培养德法兼修法治人才（ 有“划”好好说——生涯意识唤醒）	人文与法学学院	陈　琦	
kcsz2023086	典型案例	C 语言程序设计-循环结构	数学与信息学院、软件学院	杨　磊	
kcsz2023087	典型案例	叶绿体色素的提取、分离、理化性质及含量测定	基础实验与实践训练中心	李淮源	

荣誉证书

唐光文同志：

在 2024 年工程学院青年教师教学大赛中，表现突出，成绩显著，荣获

二等奖

特发此证，以资鼓励。

工程学院

2024 年 10 月 24 日

117

项目批准号	52305258
申请代码	E0506
归口管理部门	
依托单位代码	51064208A0499-0932

523052581001742

国家自然科学基金

资助项目计划书

（包干制项目）

资助类别：青年科学基金项目

亚类说明：

附注说明：

项目名称：汽芯同面结构超薄均热板内腔的液体传输机制及创新设计研究

资助经费：30万元　　执行年限：2024.01-2026.12

负 责 人：黄光文

通讯地址：广东省广州市天河区五山483号

邮政编码：510642　　电　　话：

电子邮件：huanggw@scau.edu.cn

依托单位：华南农业大学

联 系 人：唐家林　　电　　话：020-85280070

填表日期：2023年08月27日

国家自然科学基金委员会制

328

Version：1.001.742

简表

<table>
<tr><td rowspan="6">项目负责人信息</td><td>姓名</td><td>黄光文</td><td>性别</td><td>男</td><td>出生年月</td><td></td><td>民族</td><td>汉族</td></tr>
<tr><td>学位</td><td colspan="3">博士</td><td>职称</td><td colspan="3">讲师</td></tr>
<tr><td>是否在站博士后</td><td colspan="2">否</td><td colspan="2">电子邮件</td><td colspan="3">huanggw@scau.edu.cn</td></tr>
<tr><td>电话</td><td colspan="2"></td><td colspan="2">个人网页</td><td colspan="3"></td></tr>
<tr><td>工作单位</td><td colspan="7">华南农业大学</td></tr>
<tr><td>所在院系所</td><td colspan="7">工程学院</td></tr>
<tr><td rowspan="3">依托单位信息</td><td>名称</td><td colspan="5">华南农业大学</td><td>代码</td><td>51064208A0499</td></tr>
<tr><td>联系人</td><td colspan="2">唐家林</td><td colspan="2">电子邮件</td><td colspan="3">kycjhk@scau.edu.cn</td></tr>
<tr><td>电话</td><td colspan="2">020-85280070</td><td colspan="2">网站地址</td><td colspan="3">http://kjc.scau.edu.cn/</td></tr>
<tr><td rowspan="2">合作单位信息</td><td colspan="8">单位名称</td></tr>
<tr><td colspan="8"></td></tr>
<tr><td rowspan="7">项目基本信息</td><td>项目名称</td><td colspan="7">汽芯同面结构超薄均热板内腔的液体传输机制及创新设计研究</td></tr>
<tr><td>资助类别</td><td colspan="3">青年科学基金项目</td><td colspan="2">亚类说明</td><td colspan="2"></td></tr>
<tr><td>附注说明</td><td colspan="7"></td></tr>
<tr><td>申请代码</td><td colspan="3">E0506:机械设计学</td><td colspan="4"></td></tr>
<tr><td>基地类别</td><td colspan="7"></td></tr>
<tr><td>执行年限</td><td colspan="7">2024.01-2026.12</td></tr>
<tr><td>资助经费</td><td colspan="7">30万元</td></tr>
</table>

项目摘要

中文摘要：

随着便携式电子产品进一步向高性能和轻薄化发展，超薄均热板逐渐成为解决其散热难题的主力产品。申请人前期研究发现汽芯同面结构超薄均热板的传热性能优于传统分层结构，但尚存在蒸汽微通道内液滴阻塞和吸液芯液体传输性能不足两个关键问题。因此，本项目首先提出在蒸汽微通道壁面设置亲疏水组合图形的新方法，通过研究微通道的壁面亲疏水组合图形和尺寸等因素对其内部液滴的调控与传热影响机制，合理设计微通道以解决液滴阻塞问题；其次，借鉴竹秆内高效水分传输性能的导管结构，设计新型吸液芯并探明其结构参数对液体侧向吸入和纵向传输性能的影响机制，确定参数以突破现有吸液芯的传输极限；最后，综合研制超薄内腔可视化均热板，利用可视化实验分析其传热传质耦合关系，并探究新型超薄均热板关键参数对其传热性能的影响规律，总结形成设计准则。研究成果将为超薄均热板极限传热性能的突破提供理论支撑，为解决未来高性能轻薄电子产品的散热难题提供新方法。

Abstract:

With the further development of portable electronic products towards high performance, lightweight and thinness, ultra-thin vapor chambers have gradually become the main product to solve their heat dissipation problems. Our preliminary research found that the heat transfer performance of ultra-thin vapor chambers with vapor-wick co-planar structure is superior to that of the conventional layered structure, but there are still two key issues of droplet blockage inside the vapor microchannel and insufficient liquid transfer inside the wick. Firstly, this project proposes a new method to combine hydrophilic and hydrophobic patterns on the wall of the vapor microchannel. The microchannel is reasonably designed to tackle the droplet blockage issue by studying the flow regulation and heat transfer coupling mechanism through factors such as the hydrophilic-hydrophobic combination pattern and the cross-sectional size. Secondly, a novel wick is developed based on the vessel structure of bamboo culms with high-efficiency liquid transfer performance. The mechanism of the wick structural parameters on the liquid lateral inhalation and longitudinal transfer performance is investigated, and the preferred parameters of the wick are determined to break the existing liquid transfer limits. Finally, ultra-thin internal cavity visualization vapor chambers are developed comprehensively. The coupling relationship of heat and mass transfer is analyzed by visualization experiments, and the influence law of key parameters of the new ultra-thin vapor chamber on the heat transfer performance is investigated, which is summarized to form a design guideline. The results of the research will provide not only a theoretical support for the breakthrough of the ultimate heat transfer performance of ultra-thin vapor chamber, but also a new method for solving the heat dissipation challenges of future high-performance thin and light electronic products.

关键词(用分号分开)：概念设计；仿生设计；散热；汽芯同面；超薄均热板

Keywords(用分号分开)：Conceptual design; Bionics design; Heat dissipation; Vapor-wick co-planar; Ultra-thin vapor chamber

报告正文

研究内容和研究目标按照申请书执行。

国家自然科学基金项目负责人、依托单位承诺书

国家自然科学基金项目负责人承诺书

本人郑重承诺：我接受国家自然科学基金的资助，严格遵守中共中央办公厅、国务院办公厅《关于进一步加强科研诚信建设的若干意见》《关于进一步弘扬科学家精神加强作风和学风建设的意见》《关于加强科技伦理治理的意见》等规定，及国家自然科学基金委员会关于资助项目管理、项目资金管理等各项规章，在《计划书》填写及项目执行过程中：

（一）按照《批准通知》《国家自然科学基金资助项目计划书填报说明》的要求填写《计划书》，未自行降低、更改目标任务或约定要求，或缩减研究（研制）内容；

（二）树立“红线”意识，严格履行科研合同义务，按照《计划书》负责实施本项目（批准号：52305258），切实保证研究工作时间，按时报送有关材料，及时报告重大情况变动，不违规将科研任务转包、分包他人，不以项目实施周期外或不相关成果充抵交差；

（三）遵守科研诚信、科技伦理规范和学术道德，认真开展研究工作，对资助项目发表的论著和取得的研究成果按规定进行标注，不在非本项目资助的成果或其他无关成果上标注本项目批准号，反对无实质学术贡献者“挂名”，不在成果署名、知识产权归属等方面侵占他人合法权益，并如实报告本人及项目组成员发生的违背科研诚信要求的任何行为；

（四）尊重科研规律，弘扬科学家精神，严谨求实，追求卓越，反对浮夸浮躁、投机取巧，不人为夸大学术或技术价值，不传播未经科学验证的现象和观点；

（五）将项目资金全部用于与本项目研究工作相关的支出，并结合科研活动需要，科学合理安排项目资金支出进度；

（六）做好项目组成员的教育和管理，确保遵守以上相关要求。

如违背上述承诺，本人愿接受国家自然科学基金委员会和相关部门做出的各项处理决定。

项目负责人（签字）：黄光文

2023年 8 月 29 日

国家自然科学基金项目依托单位承诺书

我单位同意承担上述国家自然科学基金项目，将保证项目负责人及其研究队伍的稳定和研究项目实施所需的条件，严格遵守国家自然科学基金委员会有关资助项目管理、项目资金管理、科研诚信管理和科技伦理管理等各项规定，并督促实施。

依托单位（公章）

华南农业大学

2023年 9 月 18 日

国家自然科学基金资助项目签批审核表

<table>
<tr><td rowspan="2">本栏目由自然科学基金委填写</td><td>科学处审查意见：
同意按计划执行。
叶鑫
负责人（签章）：
2023年11月16日</td></tr>
<tr><td>科学部审查意见：
同意科学处意见
负责人（签章）：
2023年11月16日</td></tr>
</table>

受理编号： c222019102400001066

项目编号： 2022A1515110724

文件编号： 粤基金字〔2022〕18号

广东省基础与应用基础研究基金项目

任务书

项目名称： 基于亲疏水表面和仿生吸液芯的超薄均热板传热传质机制研究

项目类别： 区域联合基金-青年基金项目

项目起止时间： 2022-10-01 至 2025-09-30

管理单位（甲方）： 广东省基础与应用基础研究基金委员会

依托单位（乙方）： 华南农业大学

通讯地址： 广东省广州市天河区五山路483号

邮政编码： 510642 **单位电话：** 020-85283435

项目负责人： 黄光文 **联系电话：**

（广东科技微信公众号） （查看任务书信息） （受理纸质材料二维码）

广东省基础与应用基础研究
基金委员会
二〇二〇年制

四、项目总经费及省基金委经费预算

（一）省基金委经费下达总额：　（大写）壹拾万圆整；（小写　）10万元；					
（二）省基金委经费年度下达计划：					
年度	2022 年	年	年	年	年
经费(万元)	10.00				

五、人员信息

项目负责人								
姓名	证件号码	年龄	性别	职称	学历	在项目中承担的任务	所在单位	签名
黄光文	[redacted]	[redacted]	男	未取得	博士研究生	项目负责人	华南农业大学	黄光文

六、工作分工及财政经费分配

承担/参与单位名称（盖章）	工作分工	省级财政科技资金分配（万元）
华南农业大学	华南农业大学作为唯一单位独立承担全部研究内容。	10
	合计	10

八、本任务书签约各方

管理单位（甲方）：　广东省基础与应用基础研究基金委员会　（盖章）

科技项目合同专用章

法定代表人（或法人代理）：　曾路　曾路　（签章）

2023 年　01 月　30 日

依托单位（乙方）：　华南农业大学　（盖章）

法定代表人（或法人代理）：　刘雅红　刘雅红　（签章）

联系人（项目主管）姓名：　倪慧群　倪慧群　（签章）

Email：　kjcgxk@scau.edu.cn

电话：　020-85283435　/　[redacted]

华南农业大学科学研究院

开户单位名称：　华南农业大学

开户银行名称：　广东广州工行五山支行

开户银行帐号：　3602002609000310520

2023 年 2 月 7 日

联系人（项目负责人）姓名：　黄光文　（签名）　黄光文

Email：　huanggw@scau.edu.cn

电话：　[redacted]

2023 年 2 月 7 日

子课题编号： 2025YFD1700505-06 **密　级：公开**

国家重点研发计划
子课题任务书

子课题名称： 柑橘类果园智能施药装备研发与示范

所属课题： 果园系列化智能施药装备集成与示范应用

所属项目： 智能精准农药施用装备研发与产业化

课题牵头承担单位： 中国农业大学

子课题承担单位： 华南农业大学

子课题负责人： 黄光文

执行期限： 2025 年 12 月 至 2028 年 11 月

2025 年 12 月 20 日

子课题基本信息表

子课题名称	柑橘类果园智能施药装备研发与示范					
子课题编号	2025YFD1700505-06					
所属课题	果园系列化智能施药装备集成与示范应用					
所属项目	智能精准农药施用装备研发与产业化					
密级	■公开 □秘密 □机密	单位总数	1			
子课题类型	□基础前沿 □重大共性关键技术 ■应用示范研究 □其他					
子课题活动类型	□基础前沿 ■应用研究 □试验发展					
子课题研究所属学科	农业工程					
子课题成果应用的主要国民经济行业	农、林、牧、渔业 农业 水果种植					
子课题的社会经济目标	环境保护、生态建设及污染防治 环境污染预防					
经费预算	总经费 30.00 万元，其中中央财政专项资金 30.00 万元					
子课题周期节点	起始时间	2025 年 12 月	结束时间	2028 年 11 月		
	实施周期	共 36 个月	预计中期时间点	2027 年 06 月		
子课题承担单位	单位名称	华南农业大学	单位法定代表人姓名	薛红卫		
	单位性质	大专院校/私营企业/事业型研究单位/其他事业单位	组织机构代码	10564		
	单位主管部门	广东省教育厅	隶属关系	地方		
	单位所属地区	广东省	地市（市、自治州、盟）	广州市		
	通信地址	广州市天河区五山路 483 号	邮政编码	510642		
	单位开户名称	华南农业大学				
	开户银行（全称）	中国工商银行股份有限公司广州五山支行	汇入地点	广东省广州市		
	银行账号	3602002609000310520	银行机构代码	102581000546		
子课题负责	姓 名	黄光文	性 别	■男□女	出生日期	1989.12.20

人	证件类型	身份证	证件号码	
	所在单位	华南农业大学		
	最高学位	■博士 □硕士 □学士 □其他		
	职 称	□正高级 □副高级 ■中级 □初级 □其他	职务	无
	电子邮箱	huanggw@scau.edu.cn	移动电话	
子课题联系人	姓 名	辛伯来	电子邮箱	b.xin@scau.edu.cn
	固定电话	无	移动电话	
	证件类型	身份证	证件号码	
子课题财务负责人	姓 名	肖斐	电子邮箱	xiaofei@scau.edu.cn
	固定电话	020-85288032	移动电话	
	证件类型	身份证	证件号码	
其他参与单位	序号	单位名称	单位性质	组织机构代码
	无	无	无	无
子课题参加人数	9 人。其中：	高级职称 2 人，中级职称 2 人，初级职称 0 人，其他 5 人；		
		博士学位 4 人，硕士学位 0 人，学士学位 5 人，其他 0 人。		
子课题简介(限 500 字以内)	子课题针对柑橘品种多，受种植地区气候条件影响，施药频繁的特点，结合丘陵山地柑橘果园地形地貌、栽种方式和果树品种特性，优化设计喷雾系统与智能控制模块，通过集成冠层靶标识别传感、变量喷雾等控制技术，研制丘陵山地柑橘果园智能对靶变量喷雾装备，提升对复杂地形和不同果树长势的适应性。			

一、目标及考核指标、考核方式/方法

请填写下表。

子课题目标、预期成果与考核指标表

子课题目标[1]	预期成果				考核指标[2]				考核方式（方法）及评价手段[4]
	预期成果名称			预期成果类型	指标名称	立项时已有指标值/状态	中期指标值/状态[3]	完成时指标值/状态	
针对柑橘品种多，受种植地区气候条件影响，施药频繁的特点，结合丘陵山地柑橘果园地形地貌、栽种方式和果树品种特性，优化设计喷雾系统与智能控制模块，通过集成冠层靶标识别传感、变量喷雾控制等技术，研制柑橘果园智能对靶变量喷雾装备，提升复杂地形和不同果树长势适应性。	**主要成果**	1	柑橘果园智能对靶变量喷雾装备	□新理论 □新原理 ■新产品 □新技术 □新方法 □关键部件 □数据库 □软件 ■应用解决方案 □实验装置/系统 □临床指南/规范 □工程工艺 □标准 ■论文 ■发明专利 □其他	1.1 数量指标	/	柑橘果园智能对靶精量喷雾装备 1 套； 申请多气象条件下的柑橘果园精量低污染施药作业规程 1 项；发明专利 1 项	多气象条件下的柑橘果园精量低污染施药作业规程 1 项； 论文 1-2 篇； 发明专利 1 项； 软件著作权 1-2 项； 培养研究生 2 人	规程全文;论文全文与检索报告;专利授权证书或受理证明
					1.2 技术指标	具备施药量人工调节功能	冠层靶标探测准确度≥80%；对靶喷药系统亩均施药误差15%；地面流失量减少10%以上；技术就绪度达到 5 级	冠层靶标探测准确度≥90%；对靶喷药系统亩均施药误差≤5%；地面流失量减少 20%以上；技术就绪度达到 8 级	第三方检测机构检测报告或专家现场测评

<table>
<tr><td></td><td></td><td></td><td></td><td></td><td>1.3 推广应用指标</td><td>/</td><td>/</td><td>节省劳动力成本80%；
亩均药量施用减少25%；
果园示范面积≥1000亩</td><td>用户应用证明或专家现物、照片、视频等场考查实</td></tr>
<tr><td rowspan="5">科技报告考核指标</td><td colspan="3">序号</td><td>报告类型[5]</td><td>数量</td><td colspan="3">提交时间</td><td>公开类别及时限[6]</td></tr>
<tr><td colspan="3">1</td><td>年度科技报告</td><td>3</td><td colspan="3">2026年12月、2027年12月、2028年12月</td><td>延期公开，3年</td></tr>
<tr><td colspan="3">2</td><td>中期进展报告</td><td>1</td><td colspan="3">2027年10月</td><td>延期公开，3年</td></tr>
<tr><td colspan="3">3</td><td>最终科技报告</td><td>1</td><td colspan="3">2028年12月</td><td>延期公开，3年</td></tr>
<tr><td colspan="3">4</td><td>最终执行情况报告</td><td>1</td><td colspan="3">2028年12月</td><td>延期公开，3年</td></tr>
<tr><td colspan="10">其他目标与考核指标：无</td></tr>
</table>

九、子课题参加人员基本情况表

填表说明： 1.专业技术职称：A、正高级　B、副高级　C、中级　D、初级　E、其他；

2.投入本子课题的全时工作时间（人月）是指在子课题实施期间该人总共为子课题工作的满月度工作量；累计是指子课题组所有人员投入人月之和；

3.子课题固定研究人员需填写人员明细；

4.是否有工资性收入：Y、是　N、否；

5.人员分类代码：B、子课题负责人　C、课题/子课题骨干　D、其他研究人员；

6.工作单位：填写单位全称，其中高校要具体填写到所在院系。

序号	姓名	性别	出生日期	证件类型	证件号码	专业技术职称	职务	最高学位	专业	投入本子课题的全时工作时间（人月）	人员分类代码	在子课题中分担的任务	是否有工资性收入	工作单位
1	黄光文	男		身份证	44 1	C、中级	无	博士	机械工程	18	B、子课题负责人	负责子任务“柑橘类果园智能施药装备研发与示范”；承担丘陵山地柑橘果园智能对靶精量喷雾装备优化与创制	是	华南农业大学
2	辛伯来	男		身份证	23 2	B、副高级	无	博士	机电一体化工程	18	C、子课题骨干	参加子任务“柑橘类果园智能施药装备研发与示范”；承担多气象条件下	是	华南农业大学

												柑橘果园精量低污染施药方法研究		
3	**范鸿滔**	男		身份证		E、其他	无	学士	控制工程	18	D、其他研究人员	参加子任务“柑橘类果园智能施药装备研发与示范”，承担丘陵山地果园施药装备关键技术的研究与应用示范	否	华南农业大学
4	**兰长瑜**	男		身份证		E、其他	无	学士	控制工程	18	D、其他研究人员	参加子任务“柑橘类果园智能施药装备研发与示范”，承担丘陵山地果园施药装备关键技术的研究与应用示范	否	华南农业大学
5	**马宇辰**	男		身份证		E、其他	无	学士	机械工程	18	D、其他研究人员	参加子任务“柑橘类果园智能施药装备研发与示范”，承担丘	否	华南农业大学

十、经费预算

子课题预算表

表 B1　子课题编号：2025YFD1700504-06　　子课题名称：柑橘类果园智能施药装备研发与示范

金额单位：万元

序号	预算科目名称	金额
	（1）	（2）
1	**一、中央财政专项资金**	**30.00**
2	（一）直接费用	25.00
3	1.设备费	0
4	其中：购置设备费	0
5	2.业务费	19.50
6	3.劳务费	5.50
7	（二）间接费用（自动计算）	5.00
8	**二、其他来源资金**	**0**
9	**三、合计**	**30.00**

注：1.间接费用无需编制预算说明；2.绩效支出在间接费用中无比例限制。承担单位在统筹安排间接费用时，要处理好合理分摊间接成本和对科研人员激励的关系，绩效支出安排与科研人员在子课题工作中的实际贡献挂钩。

子课题单位经费预算明细表

表 B3　子课题编号：2025YFD1700504-06　　子课题名称：柑橘类果园智能施药装备研发与示范　　金额单位：万元

填表说明：1.单位类型分子课题承担单位、子课题参与单位；

2.组织机构代码指企事业单位国家标准代码，单位若已三证合一请填写单位统一社会信用代码，无组织机构代码的单位填写“000000000”。

序号	单位名称	组织机构代码-统一社会信用代码		单位类型	任务分工	研究任务负责人	合计	中央财政专项资金		其他来源资金
								小计	其中：间接费用	
	（1）	（2）	（3）	（4）	（5）	（6）	（7）	（8）	（9）	（10）
1	华南农业大学	统一社会信用代码	124400004554165634	子课题承担单位	柑橘类果园智能施药装备研发与示范	黄光文	30.00	30.00	5.00	0
累计							30.00	30.00	5.00	0

课题牵头承担单位（甲方）：

法定代表人签字（签章）：

中国农业大学
合同专用章
（科技）

（公章）

2025年12月26日

课题负责人签字（签章）：

2025年12月26日

子课题承担单位（乙方）：

法定代表人签字（签章）：

（公章）

2025年12月24日

子课题负责人签字（签章）：

2025年12月24日

任务书编号：2024A04J4133

广州市科技计划项目
任务书

项目名称：	新型吸液芯液体传输机制及其均热板传热性能研究
承担单位：	华南农业大学
项目负责人：	黄光文
计划类别：	基础研究计划
专题名称：	2024年度基础与应用基础研究专题
支持方向：	青年博士“启航”项目
组织单位：	华南农业大学
起止时间：	2024-01-01 至 2025-12-31
主管处室：	基础研究处

广州市科学技术局制

二〇二四年

一、项目基本信息

项目基本信息	项目名称	新型吸液芯液体传输机制及其均热板传热性能研究
	申请市财政科技经费	5(万元)
	研究期限	2（年）
项目摘要	均热板是解决电子设备等散热难题的理想元件，其内部吸液芯结构是决定其传热性能的关键。本项目研究耐热型植物高效水分传输性能的导管结构，探究导管的液体传输机制，研究其结构参数对液体侧向吸入和纵向传输性能的影响规律，并设计新型吸液芯以突破现有吸液芯的传输极限。然后，研制新型超薄均热板并研究关键参数对其传热性能的影响规律，总结形成设计准则。研究成果将为解决未来高性能轻薄电子产品的散热问题提供理论支撑。	

二、项目单位情况

项目承担单位	单位名称	华南农业大学	统一社会信用代码	1244000004554165634
	注册时间	1952-01-01	单位类型	高等院校
	注册地址	广东省广州市天河区五山路483号		
	办公地址	广东省广州市天河区五山路483号		
	联系人	姓名	倪慧群	
		手机号码		
		电子邮箱	kjcgxk@scau.edu.cn	
	开户银行	广东广州工行五山支行		
	开户户名	华南农业大学		
	银行账号	3602002609000310520		

三、项目负责人信息

姓名	黄光文	证件类型	身份证
证件号码		性别	男
出生日期		民族	汉族
国籍	中国	学历	博士研究生
学位	博士	学位授予国家（或地区）	中国
职务	讲师	职称	无
所学专业	机械工程	手机号码	
办公电话	0754-87451602	电子邮箱	939461139@qq.com

四、项目经费信息

本项目总投入：¥（5）万元，其中，市财政科技经费：¥（5）万元，自筹经费：¥（0）万元。

经费下达计划			
资金来源	小计	市财政科技经费	自筹经费
2024	5	5	0
总计	5	5	0

（单位：万元）

注：本专题纳入“包干制”，市财政科技经费按市科技计划项目经费“包干制”相关规定执行。

任务书签署

甲乙丙三方根据《广州市科技计划项目管理办法》《广州市科技计划项目经费管理办法》《广州市科技计划科技报告管理办法》等有关文件规定，以及有关法律、政策和管理要求，签署本任务书。

签订地点：广州市越秀区

广州市科学技术局（甲方）：广州市科学技术局
局项目经办人：蒋韬略　　　　　联系电话：83124150
责任处室负责人：麦胜文

合同专用章
4401040029985

2024年01月17日

项目承担单位（乙方）：华南农业大学
二级部门：华南农业大学工程学院
项目负责人：黄光文
项目经费汇入账号
账户名：华南农业大学　　账号：3602002609008310520
开户银行：广东广州工行五山支行
财务负责人：肖斐

（4）
合同专用章
4401060369544

2023年12月16日

组织单位（丙方）：华南农业大学
项目经办人：倪慧群

（4）
合同专用章
4401060369544

2023年12月18日

HXKJW/20242602

合同编号：

技术开发（委托）合同

项目名称：高性能超薄均热板研发与制造

甲　　方：广东新创意科技有限公司

乙　　方：华南农业大学

签订时间：2024-11-01

签订地点：华南农业大学

有效期限：2024 年 11 月 1 日-2028 年 12 月 30 日

中华人民共和国科学技术部印制

技术开发（委托）合同

甲　方：广东新创意科技有限公司

住所地：广州市天河区东莞庄一横路 116 号 410 室

法定代表人：陈创新

项目联系人：陈韩荫

联系方式：[redacted]

通讯地址：广州市天河区东莞庄一横路 116 号 410 室

电话：020-38457012　传真：021-51507176

电子信箱：chenhy@863cn.com

乙　方：华南农业大学

住所地：广东省广州市天河区五山路 483 号

法定代表人：薛红卫

项目联系人：黄光文

联系方式：[redacted]

通讯地址：广州市天河区五山路 483 号华南农业大学工程学院

电话：020-85282860　传真：020-85282860

电子信箱：huanggw@scau.edu.cn

本合同合作各方就共同参与研究开发 高性能超薄均热板研发与制造 项目事项，经过平等协商，在真实、充分地表达各自意愿的基础上，根据《中华人民共和国民法典》的规定，达成如下协议，并由合作各方共同恪守。

第一条 本合同合作研究开发项目的要求如下：

1．技术目标： 针对高性能超薄均热板研发与制造，合作交流，提出设计和制造方案；根据测试结果做出高性能超薄均热板性能研究报告。

2．技术内容：① 合作双方进行常规化的技术交流，探讨并制定高性能超薄均热板研发与制造方案；② 制造并测试高性能超薄均热板传热性能；③ 根据测试数据计算超薄均热板传热系数。

3．技术方法和路线：甲方提供超薄均热板研发所需实验材料、制造设备及测试平台，乙方根据甲方提供的材料和实验平台进行超薄均热板制造与性能研究。

第二条 本合同合作各方在研究开发项目中，分工承担如下工作：

乙方：

1．研究开发内容： ① 开展常规化的技术调研和合作交流，探讨高性能超薄均热板的技术需求； ② 提供高性能超薄均热板的设计方案和技术支持；③进行高性能超薄均热板的制造和性能测试，根据测试数据撰写研究报告。

2．工作进度： 2025 年 1 月 15 日前，提供高性能超薄均热板研发方案。2026 年 1 月 15 日前，完成高性能超薄均热板的初步设计和制造。2027 年 6 月 15 日前，完成传热性能优化和制造工艺制定。2027 年 6 月 15 日前，完成性能测试并撰写研究报告。

3．研究开发期限：2024 年 11 月 1 日-2028 年 12 月 30 日。

4．研究开发地点：乙方住所地及甲方制造中心所在地。

第三条 合作各方确定，各自为本合同项目的研究开发工作提供以下技术资料和条件：

甲方：（1）提供制造高性能超薄均热板所需材料、制造设备和测试设备；（2）按乙方指导进行性能测试和数据收集。

乙方：（1）提供高性能超薄均热板的设计方案和技术支持；（2）提供测试数据给甲方；（3）撰写高性能超薄均热板研发和性能测试研究报告。

第四条 合作各方确定，按如下方式提供或支付本合同项目的研究开发经费及其他投资：

甲方：

1．提供或支付方式：双方签订合同书后 20 天内，甲方需付足乙方 100%的技术开发服务费，支付方式为银行转账。

2. 支付或折算为技术投资的金额：人民币 壹万元整（￥10,000）。

户名：华南农业大学

银行账号： 3602002609000310520

开户行：广州工行五山支行

地址：广州市天河区五山路 483 号

第五条 本合同的变更必须由合作各方协商一致，并以书面形式确定。但有下列情形之一的，合作一方或多方可以向其他合作方提出变更合同权利与义务的请求，其他合作方应当在 3 日内予以答复；逾期未予答复的，视为同意：

1．发生了使合同基础发生变化的客观情况；

2．主要人员变动、国家政策变动等使原合同的继续履行显失公平或合同无法履行；

3．法律法规规定的合同可以变更的情形出现；

4．考虑双方合作过程中可能发生的变更，为维护双方利益，应留下空间。

第六条 合作各方确定因履行本合同应遵守的保密义务如下：

甲方：

1.保密内容（包括技术信息和经营信息）：①涉及本合同的技术文件、资料、经营信息和商业秘密；

2．涉密人员范围：直接或间接涉及本合同技术的相关人员。

3．保密期限：依法保密。

4．泄密责任：依照法律法规承担责任。

5．甲方在使用该项目研究结果时，不得随意夸大获得的测试数据。如因此对乙方造成负面影响时，乙方有权要求甲方赔偿相关的名誉损失。

乙方：

1.保密内容（包括技术信息和经营信息）：①涉及本合同的技术文件、资料、经营信息和商业秘密；②本合同技术标的及应用方向；③本技术的销售市场和方向。

2．涉密人员范围：①直接或间接涉及本合同技术的有关人员；②乙方的研究开发人员；③涉及与该技术成果的相关人员。

3．保密期限：依法保密。

4．泄密责任：依照法律法规承担责任。

第七条 合作各方确定按以下方式交付研究开发成果，按以下标准及方法对本合同最终完成的研究开发工作成果进行验收：

乙方：

1．研究开发成果交付的形式：研究开发成果交付的形式：根据

甲方项目需求提出工程技术问题，开展高性能超薄均热板的研发和性能测试，测试数据分析，根据测试结果撰写研究报告。

2．研究开发成果交付的时间及地点： 2028 年 12 月 30 日 ；甲方住所地。

第八条 合作各方确定，因履行本合同所产生的最终研究开发技术成果及其相关知识产权权利归属，按第 1 种方式处理：

1．双方享有发表论文或申请专利的权利。

2．按技术秘密方式处理。

第九条 实验所购买的材料、制造设备及测试设备等归甲方所有。

第十条 双方确定，按以下约定承担各自的违约责任：

1．双方违反本合同第 任一 条约定，任何一方有权终止合同。

第十一条 双 方确定，在本合同有效期内，甲方指定 陈韩荫 为甲方项目联系人，乙方指定 黄光文 为乙方项目联系人。项目联系人承担以下责任：

1．按照约定的联系时间、联系方式和联系地点完成交办的相关工作。

2．防止因人事变动而使合同难以履行或无法履行。

3．保证按约定和法律法规，以适当的时间、方式、标准履行本合同。

一方变更项目联系人的，应当及时以书面形式通知另一方，未及时通知并影响本合同履行或造成损失的，应承担相应的责任。

第十二条 双方确定，出现下列情形，致使本合同的履行成为不必要或不可能的，可以解除本合同：

1．发生不可抗力。

2．技术风险出现，技术风险指当事人努力履行，现有水平无法达

到，有足够技术难度，同行专家认定为合理失败。

3．在合同履行中，第三人公开相同的技术成果。

第十三条 双方因履行本合同而发生的争议，应协商、调解解决。协商、调解不成的，可依法向人民法院起诉。

第十四条 双方确定：本合同及相关附件中所涉及的有关名词和技术术语，其定义和解释如下：

1．对没有标准和惯例的名词、技术术语要有标准的约定和解释，防止歧义或误解。

2．文字、符号标准化和规范。

3．注意词序变换，避免引起争议。

第十五条 双方约定本合同其他相关事项为：

1．乙方赴甲方项目工地技术指导的服务天数上限为 0 人天/年。乙方赴甲方公司所在地技术服务与交流的天数上限为 0 人次/年；

第十六条 本合同一式 三 份，具有同等法律效力。

第十七条 本合同经双方签字盖章后生效。

甲方： 广东新创意科技有限公司 （盖章）

法定代表人 / 委托代理人： 陈韩荫 （签名）

2024 年 11 月 22 日

乙方： 华南农业大学 （盖章）

法定代表人 / 委托代理人： 薛红巴 （签名）

2024 年 11 月 22 日

横向科技合同受理号 HXKJHT20242774

合同编号：

技术服务合同

项目名称： 建筑物外部智能爬升式施工设备的研发

委 托 方（甲 方）： 广东钜能建设有限公司

受 托 方（乙 方）： 华南农业大学

签订时间： 2024 年 11 月 30 日

签订地点： 华南农业大学

有效期限： 2024 年 12 月 1 日至 2025 年 11 月 30 日

中华人民共和国科学技术部印制

技术服务合同

委托方（甲方）：广东钜能建设有限公司

住　所　地：韶关市武江区沐阳东路 12 号卓越雅苑商住小区 5 幢 508 号写字间

法定代表人：巨向武

项目联系人：谭婧

联系方式 ：[redacted]

通讯地址：韶关市武江区沐阳东路 12 号卓越雅苑商住小区 5 幢 508 号写字间

电　　话：0751-8208166　传真：

电子信箱：gdjngs@163.com

受托方（乙方）：华南农业大学

住　所　地：广东省广州市天河区五山路 483 号

法定代表人：薛红卫

项目联系人：黄光文

联系方式 ：[redacted]

通讯地址：广州市天河区五山路 483 号华南农业大学工程学院

电　　话：020-85282860　传真：020-85282860

电子信箱：huanggw@scau.edu.cn

本合同甲方委托乙方就 建筑物外部智能爬升式施工设备的研发 项目进行的专项技术服务，并支付相应的技术服务报酬。双方经过平等协商，在真实、充分地表达各自意愿的基础上，根据《中华人民共和国民法典》的规定，达成如下协议，并由双方共同恪守。

第一条：甲方委托乙方进行技术服务的内容如下：

1．技术服务的目标： 针对建筑物外部智能爬升式施工设备的研发进行市场调研及国内外研究现状分析，提出设计和制造方案；协助实施、技术攻关咨询工作 。

2．技术服务的内容： 完成市场调研及国内外研究现状分析；完成技术方案设计、协助实施、技术攻关咨询工作等；对方案进行答疑和帮助。

3．技术服务的方式： 技术咨询 。

第二条：乙方应按下列要求完成技术服务工作：

1．技术服务地点： 甲方所在地

2．技术服务期限： 2024 年 12 月 01 日-2025 年 11 月 30 日

3．技术服务进度： 2025 年 3 月 31 日前，完成市场调研及国内外研究现状分析，提供建筑物外部智能爬升式施工设备研发设计方案。2025 年 6 月 30 日前，指导协助甲方完成建筑物外部智能爬升式施工设备的初步设计和制造。2025 年 9 月 30 日前，完成建筑物外部智能爬升式施工设备性能优化和制造工艺制定。2025 年 11 月 30 日前，完成性能测试、投入使用。

4．技术服务质量要求： 合格并投入使用

5. 技术服务质量期限要求： 本合同服务项目的保证期为壹年，自项目通过最终验收之日起计算。

第三条：为保证乙方有效进行技术服务工作，甲方应当向乙方提供下列工作条件和协作事项：

1．提供技术资料和条件：

（1） 提供制造建筑物外部智能爬升式施工设备所需材料、制造设备和测试设备。

（2） 按乙方指导进行性能测试和数据收集。

2．其他： 乙方提供建筑物外部智能爬升式施工设备的设计方案和技术支持 。

第四条：甲方向乙方支付技术服务报酬及支付方式为：

1．技术服务费总额为： 人民币陆仟元整（￥6000，含税）

2．技术服务费由甲方 一次 （一次或分期）支付乙方。

具体支付方式和时间如下：

（1） 双方签订合同书后 20 天内，甲方需付足乙方 100%的技术开发服务费，支付方式为银行转账，乙方提供相应发票。

乙方开户银行名称、地址和帐号为：

户名：华南农业大学

银行账号： 3602002609000310520

开户行：广州工行五山支行

地址：广州市天河区五山路 483 号

第五条：双方确定因履行本合同应遵守的保密义务如下：

甲方：

1.保密内容（包括技术信息和经营信息）：涉及本合同的技术文件、资料、经营信息和商业秘密。

2．涉密人员范围：直接或间接涉及本合同技术的相关人员。

3．保密期限：依法保密。

4．泄密责任：依照法律法规承担责任。

乙方：

1.保密内容（包括技术信息和经营信息）：涉及本合同的技术文件、资料、经营信息和商业秘密；②本合同技术标的及应用方向；③本技术的销售市场和方向。

2．涉密人员范围：直接或间接涉及本合同技术的有关人员；②乙方的研究开发人员；③涉及与该技术成果的相关人员。

3．保密期限：依法保密。

4．泄密责任：依照法律法规承担责任。

第六条：本合同的变更必须由双方协商一致，并以书面形式确定。但有下列情形之一的，一方可以向另一方提出变更合同权利与义务的请求，另一方应当在3日内予以答复；逾期未予答复的，视为同意：

1．发生了使合同基础发生变化的客观情况；

2．主要人员变动、国家政策变动等使原合同的继续履行显失公平或合同无法履行；

3．法律法规规定的合同可以变更的情形出现；

4．考虑双方合作过程中可能发生的变更，为维护双方利益，应

留下空间。

第七条：双方确定以下列标准和方式对乙方的技术服务工作成果进行验收：

1．乙方完成技术服务工作的形式：研究开发成果交付的形式。

2．技术服务工作成果的验收标准：根据甲方项目需求提出工程技术问题，完成市场调研及国内外研究现状分析，开展建筑物外部智能爬升式施工设备的研发和性能测试，测试数据分析，根据测试结果撰写研究报告。

3.技术服务工作成果的验收方法：验收方出具书面验收证明。

4．验收的时间和地点：2025 年 12 月 31 日 ；甲方住所地。

第八条：双方确定：

1．在本合同有效期内，甲方利用乙方提交的技术服务工作成果所完成的新的技术成果，归 双 （甲、双）方所有。

2．在本合同有效期内，乙方利用甲方提供的技术资料和工作条件所完成的新的技术成果，归 双 （乙、双）方所有。

第九条：双方确定，按以下约定承担各自的违约责任：

1．双方违反本合同第 任一 条约定，任何一方有权终止合同。

第十条：双方确定，在本合同有效期内，甲方指定 谭婧 为甲方项目联系人，乙方指定 黄光文 为乙方项目联系人。项目联系人承担以下责任：

1．按照约定的联系时间、联系方式和联系地点完成交办的相关

工作。

2．防止因人事变动而使合同难以履行或无法履行。

3．保证按约定和法律法规，以适当的时间、方式、标准履行本合同。

一方变更项目联系人的，应当及时以书面形式通知另一方，未及时通知并影响本合同履行或造成损失的，应承担相应的责任。

第十一条：双方确定，出现下列情形，致使本合同的履行成为不必要或不可能的，可以解除本合同：

1．发生不可抗力；

2．技术风险出现，技术风险指当事人努力履行，现有水平无法达到，有足够技术难度，同行专家认定为合理失败。

3．在合同履行中，第三人公开相同的技术成果。

第十二条：双方因履行本合同而发生的争议，应协商、调解解决。协商、调解不成的，确定按以下第 2 种方式处理：

1．提交 / 仲裁委员会仲裁；

2．依法向人民法院起诉。

第十三条：双方确定：本合同及相关附件中所涉及的有关名词和技术术语，其定义和解释如下：

1．对没有标准和惯例的名词、技术术语要有标准的约定和解释，防止歧义或误解。

2．文字、符号标准化和规范。

3．注意词序变换，避免引起争议。

第十四条：双方约定本合同其他相关事项为：<u>无</u>。

第十五条：本合同一式<u>二</u>份，具有同等法律效力。

第十六条：本合同经双方签字盖章后生效。

甲方：　　广东钜能建设有限公司　　（盖章）

法定代表人 / 委托代理人：　　（签名）

2024 年 11 月 30 日

乙方：　　华南农业大学　　（盖章）

法定代表人 / 委托代理人：薛红巳　　（签名）

2024 年 11 月 30 日

编号：CARS-32-10

国家荔枝龙眼产业技术体系
2023 年度任务书

岗位名称：	果园生产机械化
岗位科学家：	李君
岗位科学家依托单位：	华南农业大学
依托单位法定代表人：	刘雅红

农业农村部科技教育司

二〇二三年六月

一、基本情况表

（一）岗位科学家情况

岗位名称	果园生产机械化				
岗位科学家	李君	**性别**	男	**出生年月**	
职称	教授	**学历**	博士	**行政职务**	常务副院长
工作单位	华南农业大学				
通讯地址/邮编	广东省广州市天河区五山 483 号/510642				
电话/电子信箱	[redacted]/autojunli@scau. edu. cn				
所属功能研究室	机械化研究室				
功能研究室主任	李君				

（二）团队成员情况

姓名	**学历/职称**	**出生年月**	**性别**	**工作单位**	**电话/邮箱**
王慰祖	博士研究生/ 副教授		男	华南农业大学	egwwz@scau.edu.cn
谢家兴	博士研究生/ 讲师		男	华南农业大学	xjx1998@scau.edu.cn
郭嘉明	博士研究生/ 副教授		男	华南农业大学	jmguo@scau.edu.cn
黄光文	博士研究生/ 讲师		男	华南农业大学	huanggw@scau.edu.cn

四、2023 年绩效目标表

岗位名称	果园生产机械化			
总经费	59.50 万元			
年度总体目标	围绕“十四五”和年度重点任务开展研发、技术试验和示范工作，为全国荔枝龙眼产业高质量发展提供良好的技术支撑。2023 年目标为优化创制多风道风送喷雾机、自主导航割草机、便携式花量计数仪、声波土壤检测仪、智能采收机、辅助采摘平台、移动式蓄冷喷淋预冷装置等装备；建设智慧果园 1 个；开展农机化技术推广，举办农机作业观摩活动及技术培训 2 次以上；示范果树修剪机、割草机等农机装备以及蓄冷式预冷系统等保鲜装备。			
	一级指标	二级指标	三级指标	指标值
绩效指标	产出指标	数量指标	获得新品种（新产品、新设备、新技术新规程等）等技术成果数量	2
		数量指标	申报专利数量	3
		数量指标	科技成果试验示范情况	在 1 个区域进行
		数量指标	科技成果推广应用情况	500 亩
		数量指标	培训基层农技推广人员和农民等	100 人
		数量指标	中央级媒体宣传报道次数	/
		数量指标	省级媒体宣传报道次数	/
		时效指标	在主产区开展产业应急技术服务反应时间	/
	效益指标	社会效益指标	向中央和地方政府、企事业单位提供各类产业分析报告和政策建议等	/
		生态效益指标	研发的绿色增产技术或产品在主产区示范应用可实现节水或节肥或节药或省工	建设智慧果园，应用农机装备实现部分环节省力化生产，节肥节药省工明显。
	满意度指标	服务对象满意度指标	上级部门满意度	≥90%
			技术用户满意度	≥90%

六、签约方

国家荔枝龙眼产业技术体系首席科学家（签字）：陈厚彬

年　月　日

国家荔枝龙眼产业技术研发中心依托单位：（公章）

依托单位法定代表人（签字）：刘雅红

年　月　日

功能研究室主任（签字）：李君

2023年7月15日

岗位科学家（签字）：李君

2023年7月15日

岗位依托单位：华南农业大学　（公章）

依托单位法定代表人（签字）：刘雅红

年　月　日

编号：CARS-32-09

国家荔枝龙眼产业技术体系
2024 年度任务书

岗位名称：果园生产机械化

岗位科学家：李君

岗位科学家依托单位：华南农业大学

依托单位法定代表人：薛红卫

农业农村部科学技术司

二〇二四年五月

一、基本情况表

（一）岗位科学家情况

岗位名称	果园生产机械化				
岗位科学家	李君	性别	男	出生年月	
职称	教授	学历	博士	行政职务	院长
工作单位	华南农业大学				
通讯地址/邮编	广东省广州市天河区五山 483 号 / 510642				
电话/电子信箱	/ autojunli@scau.edu.cn				
所属功能研究室	机械化研究室				
功能研究室主任	李君				

（二）团队成员情况

姓名	学历/职称	出生年月	性别	工作单位	电话/邮箱
王慰祖	博士研究生/副教授	3	男	华南农业大学	/ egwwz@scau.edu.cn
谢家兴	博士研究生/副教授	8	男	华南农业大学	/ xjx1998@scau.edu.cn
郭嘉明	博士研究生/副教授	3	男	华南农业大学	/ jmguo@scau.edu.cn
黄光文	博士研究生/讲师	2	男	华南农业大学	huanggw@scau.edu.cn

二、2024 年经费预算表

科目名称	主 要 用 途	经 费（万元）
1.设备费	用于在研究开发和试验示范过程中，购置或试制专用仪器设备、购置计算类仪器设备和软件工具、对现有仪器设备进行升级改造、以及租赁外单位仪器设备或购买专用软件授权而发生的费用。	5.00
2.业务费	用于在研究开发和试验示范过程中，消耗的材料、辅助材料等低值易耗品的采购、运输、装卸、整理等费用，发生的测试化验加工、燃料动力、会议/差旅费、出版/文献/信息传播/知识产权事务等费用，以及其他相关支出。	36.8
3.劳务费	用于在研究开发和试验示范过程中，支付给参与体系任务的研究生、博士后、访问学者和科研辅助人员等劳务性费用，其开支标准参照当地科学研究和技术服务业从业人员平均工资水平，根据其在体系研发中承担的工作任务确定，其由单位缴纳的社会保险补助、住房公积金等可纳入劳务费科目支出。	24.00
4.管理费	用于在研究开发和试验示范过程中对使用依托单位现有仪器设备及房屋、试验田，日常水、电、气、暖消耗，以及其他有关管理费用的补助支出。管理费比例不超过扣除设备费后的 8%，由依托单位管理和使用。	4.20
合 计	**70.00（万元）**	

三、2024 年绩效目标表

岗位名称	果园生产机械化			
总经费	70 万元			
年度总体目标	2024 年目标为创制/改进开沟施肥机、自主导航割草机、智能采收机、采收分级一体化平台、移动式喷淋预冷装置等装备；建设智慧果园 1 个；开展农机化技术推广，举办农机作业观摩活动及技术培训 1 次以上；示范喷药机、割草机等农机装备以及田间预冷系统等保鲜装备。			
	一级指标	二级指标	三级指标	指标值
绩效指标	产出指标	数量指标	获得新品种（新产品、新设备、新技术新规程等）等技术成果数量	2
		数量指标	申报专利数量	3
		数量指标	科技成果试验示范情况	在 1 个区域进行
		数量指标	科技成果推广应用情况	200 亩以上
		数量指标	培训基层农技推广人员和农民等	100 人以上
		数量指标	中央级媒体宣传报道次数	/
		数量指标	省级媒体宣传报道次数	/
		时效指标	在主产区开展产业应急技术服务反应时间	/
	效益指标	社会效益指标	向中央和地方政府、企事业单位提供各类产业分析报告和政策建议等	/
		生态效益指标	研发的绿色增产技术或产品在主产区示范应用可实现节水或节肥或节药或省工	建设智慧果园，应用农机装备实现部分环节省力化生产，节肥节药省工明显。
	满意度指标	服务对象满意度指标	上级部门满意度	≥90%
			技术用户满意度	≥90%

五、签约方

国家荔枝龙眼产业技术体系首席科学家（签字）：

陈厚彬

2024年6月15日

国家荔枝龙眼产业技术研发中心依托单位：（公章）

依托单位法定代表人（签字）：薛红卫

2024年6月15日

功能研究室主任（签字）：李君

2024年6月15日

岗位科学家（签字）：李君

2024年6月15日

岗位依托单位：华南农业大学（公章）

依托单位法定代表人（签字）：薛红卫

2024年6月15日

编号：**CARS-32**-10

国家荔枝龙眼产业技术体系 2025 年度任务书

岗位名称：果园生产机械化

岗位科学家：李君

岗位科学家依托单位：华南农业大学

依托单位法定代表人：薛红卫

农业农村部科学技术司

二〇二五年四月

一、基本情况表

（一）岗位科学家情况

岗位名称	果园生产机械化				
岗位科学家	李君	**性别**	男	**出生年月**	
职称	教授	**学历**	博士	**行政职务**	院长
工作单位	华南农业大学				
通讯地址/邮编	广东省广州市天河区五山 483 号 / 510642				
电话/电子信箱	autojunli@scau.edu.cn				
所属功能研究室	机械化研究室				
功能研究室主任	李君				

（二）团队成员情况

姓名	**学历/职称**	**出生年月**	**性别**	**工作单位**	**电话/邮箱**
王慰祖	博士研究生/副教授		男	华南农业大学	egwwz@scau.edu.cn
谢家兴	博士研究生/副教授		男	华南农业大学	xjx1998@scau.edu.cn
郭嘉明	博士研究生/副教授		男	华南农业大学	jmguo@scau.edu.cn
黄光文	博士研究生/讲师		男	华南农业大学	huanggw@scau.edu.cn

三、2025 年经费预算表

科目名称	主 要 用 途	经 费 （万元）
1.设备费	用于在研究开发和试验示范过程中，购置或试制专用仪器设备、购置计算类仪器设备和软件工具、对现有仪器设备进行升级改造、以及租赁外单位仪器设备或购买专用软件授权而发生的费用。	5.00
2.业务费	用于在研究开发和试验示范过程中，消耗的材料、辅助材料等低值易耗品的采购、运输、装卸、整理等费用，发生的测试化验加工、燃料动力、会议/差旅费、出版/文献/信息传播/知识产权事务等费用，以及其他相关支出。	42.8
3.劳务费	用于在研究开发和试验示范过程中，支付给参与体系任务的研究生、博士后、访问学者和科研辅助人员等劳务性费用，其开支标准参照当地科学研究和技术服务业从业人员平均工资水平，根据其在体系研发中承担的工作任务确定，其由单位缴纳的社会保险补助、住房公积金等可纳入劳务费科目支出。	18.00
4.管理费	用于在研究开发和试验示范过程中对使用依托单位现有仪器设备及房屋、试验田，日常水、电、气、暖消耗，以及其他有关管理费用的补助支出。管理费比例不超过扣除设备费后的 8%，由依托单位管理和使用。	4.20
合 计	**70.00（万元）**	

四、2025年绩效目标表

岗位名称		果园生产机械化		
总经费		70万元		
年度总体目标	2025年目标为研制多风管仿形喷药机、双边机械式避障割草机、辅助采摘分级一体机等各1台（套），果园荔枝花序雌雄蕊数量三维检测软件1种，荔枝生长全过程智慧化管控系统1种；建立初步智慧化管理的示范果园1个；指导综合试验站在6个示范园开展果园生产机械化试验示范；收集、监测和分析生产机械化发展信息，开展产业政策研究咨询与服务，加强与体系内外的交流合作。			
	一级指标	二级指标	三级指标	指标值
绩效指标	产出指标	数量指标	获得新品种（新产品、新设备、新技术新规程等）等技术成果数量	3
		数量指标	申报专利数量	3
		数量指标	科技成果试验示范情况	在6个示范园进行
		数量指标	科技成果推广应用情况	1000亩以上
		数量指标	培训基层农技推广人员和农民等	100人以上
		数量指标	中央级媒体宣传报道次数	/
		数量指标	省级媒体宣传报道次数	/
		时效指标	在主产区开展产业应急技术服务反应时间	/
	效益指标	社会效益指标	向中央和地方政府、企事业单位提供各类产业分析报告和政策建议等	/
		生态效益指标	研发的绿色增产技术或产品在主产区示范应用可实现节水或节肥或节药或省工	建设智慧果园，应用农机装备实现部分环节省力化生产，节肥节药省工明显。
	满意度指标	服务对象满意度指标	上级部门满意度	≥90%
			技术用户满意度	≥90%

六、签约方

国家荔枝龙眼产业技术体系首席科学家（签字）： 胡桂兵 2025年 6月 16日
国家荔枝龙眼产业技术研发中心依托单位：（公章） 依托单位法定代表人（签字）：薛红卫 2025年 6月 16日
功能研究室主任（签字）： 2025年 6月 16日
岗位科学家（签字）： 2025年 6月 16日
岗位依托单位：（公章） 依托单位法定代表人（签字）：薛红卫 2025年 6月 16日

SCAULIB202625981

检索证明

根据委托人提供的论文材料，委托人**华南农业大学工程学院 黄光文(学科类型:自然科学)** 3 篇论文收录情况如下表。

序号	论文名称	发表刊物及发表的年月卷期/页码等	作者排名	论文等级	作者文中单位	收录情况	影响因子	中科院大类分区
1	Field Grading of Longan SSC via Vis-NIR and Improved BP Neural Network	AGRICULTURE-BASEL 出版年：2024 出版日期：DEC 卷期：14 12 页码：- 文献号：2297 文献类型：Article	通讯作者	A 类	华南农业大学 工程学院	SCI	IF2-year=3.6 IF5-year=3.8 （2024）	农林科学 2 区 Top 期刊：否 OA 期刊：是 （2025）
2	Research on Ditching Mechanism of Self-Excited Vibration Ditching Machine	AGRONOMY-BASEL 出版年：2023 出版日期：MAR 卷期：13 3 页码：- 文献号：905 文献类型：Article	通讯作者	A 类	华南农业大学 工程学院	SCI	IF2-year=3.3 IF5-year=3.7 （2023）	农林科学 2 区 Top 期刊：否 OA 期刊：是 （2023）
3	Detection and grading of oxidation for copper-water heat pipe wicks based on the machine learning methods	APPLIED THERMAL ENGINEERING 出版年：2025 出版日期：AUG 1 卷期：272 页码：- 文献号：126437	共同通讯作者（倒数第一）	A 类	华南农业大学 工程学院	SCI	IF2-year=6.9 IF5-year=6.6 （2024）	工程技术 2 区 Top 期刊：是 OA 期刊：否 （2025）

		文献类型：Article						

说明：论文等级和中科院大类分区按《华南农业大学学术论文评价方案（试行）》划分。

报告免责声明:如未盖章,报告无效

agronomy

Article

Research on Ditching Mechanism of Self-Excited Vibration Ditching Machine

Jun Li [1,2], Hongcai Li [1], Yingyi Chen [1], Peiyi Lin [1], Qianqian Zhang [1], Ying Cheng [1], Zhou Yang [3] and Guangwen Huang [1,*]

[1] College of Engineering, South China Agricultural University, Guangzhou 510642, China
[2] Guangdong Laboratory for Lingnan Modern Agriculture, Guangzhou 510642, China
[3] Guangdong Provincial Key Laboratory of Conservation and Precision Utilization of Characteristic Agricultural Resources in Mountainous Areas, Jiaying University, Meizhou 514015, China
[*] Correspondence: huanggw@scau.edu.cn; Tel.: +86-158-8996-1680

Abstract: A vibration ditching machine is a machine that can effectively reduce ditching resistance and energy consumption. In this paper, taking a self-developed, self-excited vibration ditching machine as the research object, we explore its internal dynamic vibration characteristics upon excitement when ditching, which reduces its resistance and energy consumption. The vibration characteristics of a ditching machine with three degrees of freedom (Y, Ry, and Rx directions), which are generated by the vibration of the self-excited ditching machine, are evaluated; the rotating speed, spring stiffness, spring damping coefficient, and blade weight are taken as factors, and their effects on the vibration characteristics are analyzed by an Adams–Edem coupling simulation model and a theoretical dynamics model of the self-excited ditching machine. Finally, a comparative analysis of the ditching machine of self-excited and nonself-excited ditching machines is conducted. The results of the analysis show that the rotating speed, spring stiffness, spring damping coefficient, and blade weight are important factors affecting the vibration characteristics. The theoretical dynamics model and the Adams–Edem coupling simulation model can represent the internal vibration mechanism of the self-excited ditching machine during ditching. The self-excited vibrating ditching machine is helpful in reducing the energy consumption of ditching.

Keywords: ditching machine; self-excited vibration; vibration characteristics; mechanism research; resistance reduction and consumption reduction; coupling simulation

Citation: Li, J.; Li, H.; Chen, Y.; Lin, P.; Zhang, Q.; Cheng, Y.; Yang, Z.; Huang, G. Research on Ditching Mechanism of Self-Excited Vibration Ditching Machine. *Agronomy* **2023**, *13*, 905. https://doi.org/10.3390/agronomy13030905

Academic Editor: Andrea Peruzzi

Received: 8 February 2023
Revised: 13 March 2023
Accepted: 15 March 2023
Published: 18 March 2023

1. Introduction

A fertilizer ditching machine is a widely used piece of orchard operation machinery [1], used in orchard fertilization work that can reduce the labor intensity of farmers and improve fertilization efficiency and the fertilizer utilization rate [2]. In the process of ditching, most of the energy consumption of the ditching and fertilizer machine comes from ditching and breaking the soil; additionally, crushing the ground requires a large amount of energy [1]. Therefore, the research and development of ditching technology to reduce the resistance and energy consumption of the process have become the focus of recent fertilizer ditching machine technology studies [3].

The ditching blade is the most frequently worked and easily damaged part of the device. To date, the existing research has mainly focused on profiling ditching blades to reduce their resistance and energy consumption [4]. Maohua Xiao used the characteristics of the contour-fitting curves of the forefoot and toe of Oriental mole crickets to design a well-profiled ditching blade [5]. Jianfeng Sun designed a new ditching blade that resembled a low-resistance brown bear claw [6]. Jun Guo [7] and Yuwan Yang [8] designed ditching blades that imitated the multitoe structural features of moles. Jie Yu [9] mimicked the geometric shape of the paw toe of a rabbit, and Hui Qi [10] imitated the forefoot geometries of crabs and turtles. The resistance reduction performance of a bionic blade was verified by experiments [11]. However, at this stage, scholars' bionomics of soil organisms are mainly reflected in designing simulations of their fixed forms of appearance, which makes it difficult to meet the increased precision and accuracy requirements for agricultural machinery design [12].

Therefore, there is an urgent need to design a new ditching mechanism based on other perspectives to reduce ditching power consumption. Research shows that vibration exhibits the most pronounced effect on resistance reduction among the various resistance and energy reduction techniques [13]. Vibration cutting involves two-dimensional cutting in the horizontal and vertical directions [14]. According to the structure and working principles of the machine, vibration can be divided into forced vibration and self-excited vibration [15]. In essence, forced vibration is the secondary distribution of tractor power. The drive excitation system requires energy consumption and cannot reduce the total power consumption [16]. Self-excited vibration reduces the resistance to a degree similar to that of forced vibration without applying additional power [17]. The primary driving forces of self-excited vibration are the variation in ditching depth and the variation in ditching resistance due to soil debris and variable soil mechanical properties [18]. Soil is subjected to vibration and stores some of the vibration energy, which makes the internal stress of the soil more significant; the larger the internal pressure is, the more efficiently the soil is broken [19]. When not vibrating, the ditching parts cut the soil and lift the soil stage simultaneously. When vibrating, the soil cutting and lifting are divided into two independent stages; the horizontal component of the force is lower than it is when not vibrating [16], and part of the resistance is offset by the vibration effect of the vibrating device, which reduces the total traction resistance [20].

Many scholars have conducted extensive research on vibratory ditching machines [21]. MA et al. designed a self-excited vibratory deep loosener to study the mechanism of deep loosening action and stress changes in the soil [22]. Razzaghi et al. chose a new mathematical model to analyze the effects of some key design parameters on the performance of vibratory tillage implements [23]. Ahmaside et al. used classical mechanics theory to derive the dynamic torque of rotating tillage blades from a dynamics-perspective computational model [24]. Zhang Xiaotong et al. proposed a vibration dynamics model of a grooving device [25]. Jingjing Fang et al. [26], Yanlin Wang [27], and Chenjun Hu [28] proposed a theoretical basis for vibration reduction methods. However, the vibratory ditching machine is limited by its rotating structure. The introduction of ditching blade vibration makes the device more complex, and the vibration of multiple sets of blades makes the characteristics of the system dynamics more complex; additionally, the stability of rotation under high-speed conditions is affected. For a vibratory ditching machine, the existing design involves applying excitation directly to the ditching blade. Nevertheless, a solution needs to be able to design an entire ditching machine structure, and it cannot be applied to a small ditching machine.

To solve the problem of significant energy loss in the ditching process of ditching blades, we designed a self-excited vibration ditching machine. This machine realizes a reduction in resistance and energy consumption by introducing vibration. Based on the theoretical dynamics model of the self-excited vibration ditching machine and the Adams–Edem coupling simulation model, the vibration characteristics of the self-excited vibration ditching machine were analyzed, and the accuracies of the theoretical dynamics model and Adams–Edem coupling simulation model were further verified through bench tests. Finally, a comparative analysis of the rotating torque of self-excited vibration ditching machines and nonself-excited vibration ditching machines was carried out, and the mechanism of self-excited vibration to reduce resistance and consumption was elaborated to provide a reference for research on vibration to reduce resistance and consumption.

2. Materials and Methods

2.1. Self-Excited Vibration Ditching Machine

The self-excited vibration ditching machine structure is shown in Figure 1. The self-excited vibration device is installed between the blade and the mounting bracket. The two ends are secured with nuts through a fixed connection, and the working state is achieved through elastic and limiting devices that generate a certain amplitude of self-excited vibration.

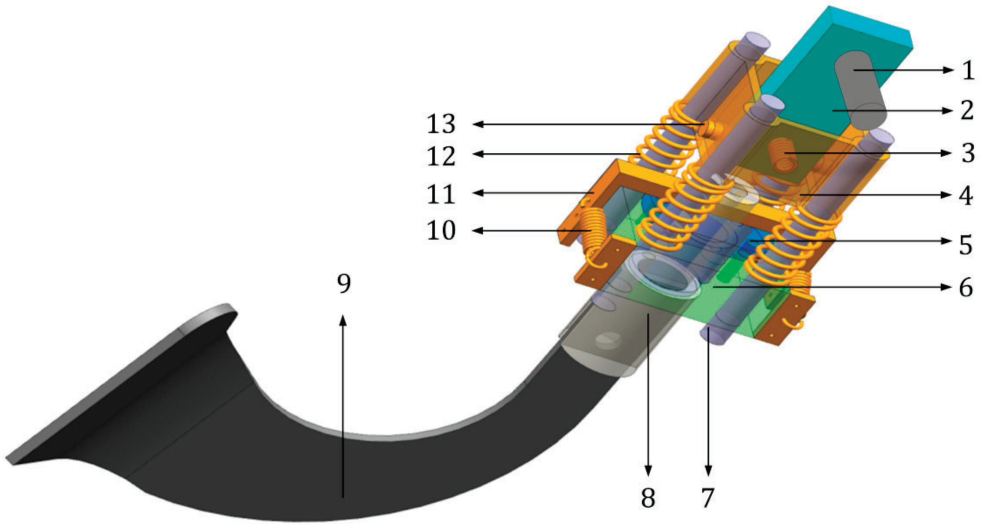

Figure 1. Structure of the self-excited vibration ditching machine: 1. blade roller shaft, 2. mounting bracket (Rigid Body 1), 3. compression spring k_1, 4. square mounting base m_1 (Rigid Body 2), 5. bearing base, 6. lower base m_2 (Rigid Body 3), 7. connecting bolt, 8. blade connecting base, 9. blade m_3 (Rigid Body 4), 10. tension spring k_3, 11. torsion beam, 12. compression spring k_2, 13. bracket connecting rod.

The whole device can be equated to 4 rigid bodies, with Rigid Body 1 and the blade axis solidly connected; compression springs are installed between Rigid Bodies 2 and 1 to provide stiffness in the Rx direction (blade oscillation relative to the blade axis). A compression spring is set between Rigid Body 2 and Rigid Body 3 to provide stiffness in the Y direction to realize the telescopic movement of the blade. A pair of tension springs are set between Rigid Bodies 3 and 4; one end is mounted on the bearing seat, and the other end is mounted on the torsion beam. In contrast, the torsion beam is connected to the blade shaft through bolts, and the torsional stiffness is equivalent to that in the Ry direction to realize the torsional movement of the blade. As an intermediate connection between the blade and the blade shaft, the device generates vibrations of the blade with three degrees of freedom relative to the blade shaft. When encountering hard local soil or stones during ditching, the blade can produce adaptive deflection and contraction to reduce wear and input torque. When the blade shaft rotates at a certain speed, the blade is forced to vibrate by the periodic soil force. When the vibration amplitude and frequency are under suitable conditions, the average input value of the torque can be effectively decreased to reduce resistance and energy consumption.

2.2. Theoretical Modeling of the Dynamics of a Self-Excited Vibratory Ditching Machine

The structure of the self-excited vibration ditching machine is simplified to obtain the dynamics model of the ditching blade; the simplified model is shown in Figure 2. Under the action of the compression spring k_2, m_2 and k_3 are displaced in the Y direction, m_3 produces torsional motion in the Ry direction under the action of the tension spring k_3, and the overall ditching blade is deflected and displaced in the Rx direction. The excitation force transmitted to the ditching blade by the ditching drive is $F_0 \cos \omega t$. The X, Y, and

Z directions of the coordinate system correspond to the forward direction, the vertically downward direction, and the direction perpendicular to the XY plane, respectively, of the ditching machine.

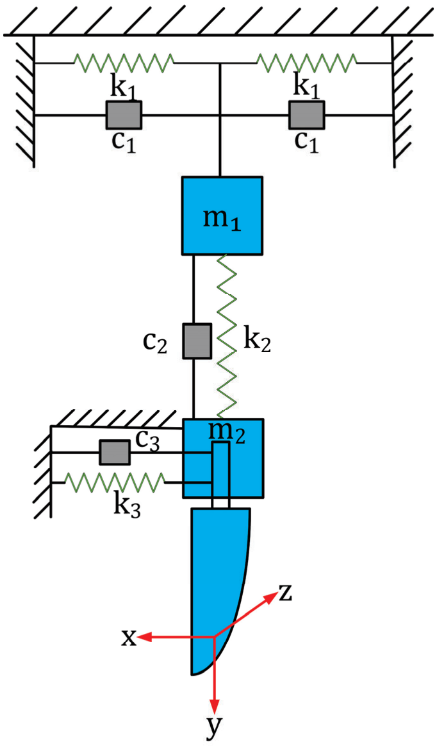

Figure 2. Simplified model of the self-excited vibration ditching machine.

The following force analysis of the ditching blade is shown in Figure 3, which displays a force analysis of the rotary self-excited vibration machine in the Y, Ry, and Rx directions.

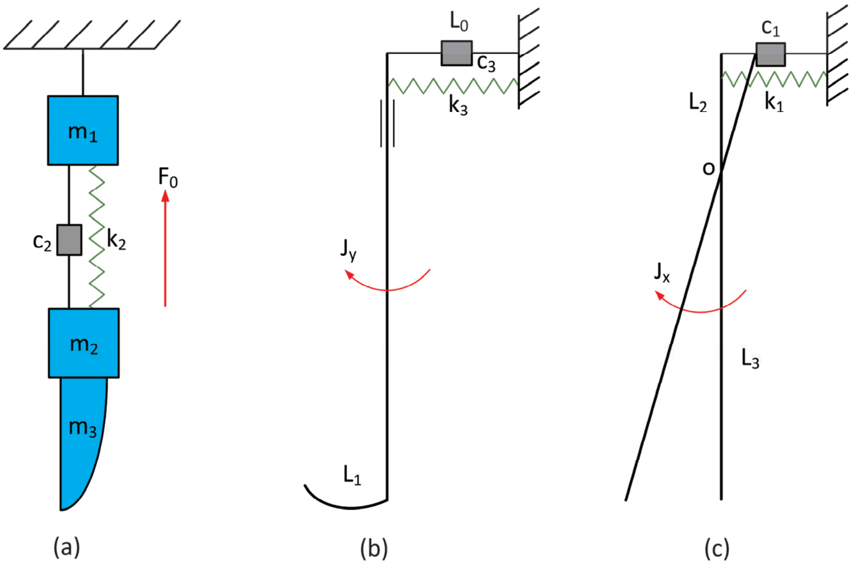

Figure 3. Analyses of the forces in the Y, Ry, and Rx directions of the self-excited vibration rotary machine: (**a**) Y-directional force analysis, (**b**) Ry-directional force analysis, and (**c**) Rx-directional force analysis.

The blade makes a linear reciprocating motion in the Y direction relative to m_1. During the rotation, $F_0 \cos \omega t$ is used as the excitation force, and a force analysis of the Y direction is conducted to obtain the following Y-directional dynamics model:

$$(m_2 + m_3)\ddot{x} + 4c_2\dot{x} + 4k_2x = F_0 \cos \omega t \tag{1}$$

$$F_0 = (m_2 + m_3)\omega^2 R \tag{2}$$

$$\omega = 2\pi n \tag{3}$$

where F_0 is the centripetal force, ω is the angular velocity, R is the distance from the m_1 center of mass to the m_2 center of mass, and n is the rotating speed.

The rotational inertia of the blade mass block m_3 is set to J_y, the angle of rotation of the blade is set to θ_y, and the distance between the point of action of the force and the center of rotation is set to L_0. According to Newton's second law and the momentum moment theorem, we can obtain the following equations:

$$J_y\ddot{\theta}_y + c_3L_0^2 \tan \dot{\theta}_y + k_3L_0^2 \tan \theta_y = 0 \tag{4}$$

$$J_y = \frac{1}{2}m_3L_1^2 \tag{5}$$

where L_0 is the distance from the k_3 spring tension to the rotating axis and L_1 is the radius of the blade axis.

The angle of deflection of the blade in the Rx direction is θ_x, the distance of the spring from the center of deflection is L_2, and the rotational inertia around the Rx direction is J_x. Then, according to Newton's second law and the momentum moment theorem, the Rx direction dynamics model can be obtained as follows:

$$J_x\ddot{\theta}_x + c_1\dot{x}_1L_2 + k_1x_1L_2 = 0 \tag{6}$$

$$J_x = \frac{1}{12}(m_1 + m_2 + m_3)(L_2 + L_3)^2 + (m_1 + m_2 + m_3)\left[\frac{(L_2 + L_3)}{2} - L_2\right]^2 \tag{7}$$

where L_2 is the distance from the k_1 spring tension to the rotating shaft and L_3 is the overall deflection radius of the ditching blade.

Since there is only a slight rotation of the ditching blade in the Ry and Rx directions, $\tan \theta \approx \theta$; In summary, the overall dynamics model of the self-excited vibration ditching machine can be obtained as follows.

$$(m_2 + m_3)\ddot{x} + 4c_2\dot{x} + 4k_2x = F_0 \cos \omega t \tag{8}$$

$$J_y\ddot{\theta}_y + c_3L_0^2\dot{\theta}_y + k_3L_0^2\theta_y = 0 \tag{9}$$

$$J_x\ddot{\theta}_x + c_1L_2^2\dot{\theta}_x + k_1L_2^2\theta_x = 0 \tag{10}$$

The structural parameters of the self-excited vibration ditching machine are shown in Table 1.

Table 1. Machine vibration device structure parameters.

Name	Numerical Value
K_3 spring tension to spindle distance L_0	0.035 m
Radius of blade axis L_1	0.0125 m
K_1 spring tension to pivot distance L_2	0.020 m
Overall deflection radius of ditching blade L_3	0.20 m
The distance R from the center of mass of m_1 to the center of mass of m_2	0.076 m
Upper mass block m_1	0.50 kg
Lower mass block m_2	1.00 kg
Blade mass block m_3	1.00 kg

2.3. Establishment of the Adams–Edem Coupled Simulation Model of the Self-Excited Vibration Ditching Machine and Soil Interaction

2.3.1. Establishment of the ADAMS Multibody Dynamics Simulation Model for a Self-Excited Vibration Ditching Machine

To verify the accuracy of the dynamics model of the self-excited ditching machine, a virtual prototype model is constructed by the dynamics simulation software ADAMS, as shown in Figure 4. A 3D drawing of the self-excited ditching machine is imported into ADAMS, constraints and parameters are set, material properties are added, and the material type of the geometry is set to steel; its density is 7801 kg/m^3, Young's modulus is 2.07×10^{11} N/m^2, and Poisson's ratio is 0.3, setting the corresponding constraints according to the motion of each degree of freedom.

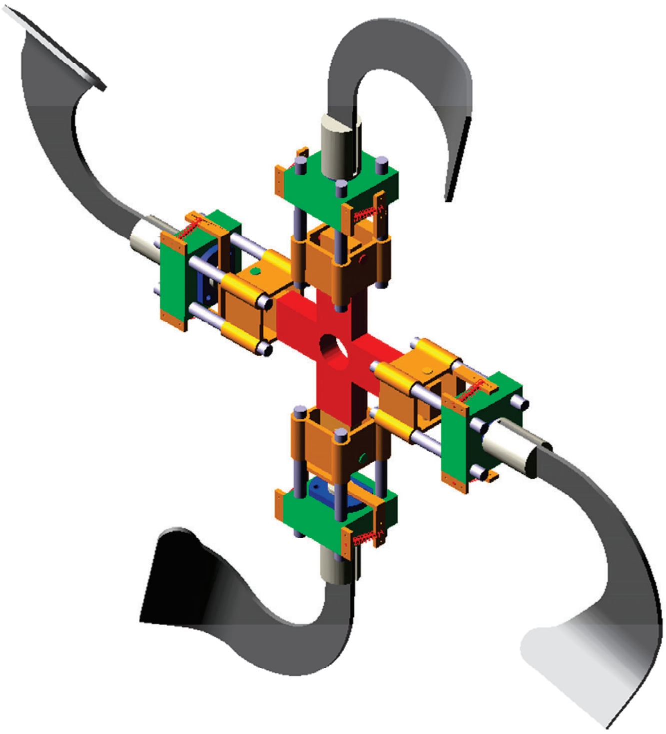

Figure 4. ADAMS multibody dynamics simulation model of a self-excited vibration ditching machine.

2.3.2. Establishment of the Edem Discrete Element Simulation Model for a Self-Excited Vibration Ditching Machine

In the Edem simulation, the Hertz-Mindlin with JKR contact model was selected [29] for the particle-to-particle contact with a surface energy of 7.91 J/m^2, and the Hertz-Mindlin no slip contact model was selected for the particle-to-geometry contact. The appropriate contact mechanics model was set up in the EDEM preprocessor module [30], and the simulation parameters were set as shown in Tables 2 and 3.

Table 2. Material property parameters.

Material	Poisson's Ratio	Young's Modulus (Pa)	Density (kg/m^3)
Soil	0.4	1×10^6	1650
45 steel	0.3	7×10^{10}	7800
Steel	0.3	7×10^{10}	7800

Table 3. Contact property parameters.

Interaction Material	Recovery Coefficient	Static Friction Coefficient	Rolling Friction Coefficient
Soil and Soil	0.2	0.67	0.03
Soil and 45 steel	0.2	0.75	0.1
Soil and steel	0.2	0.75	0.1

The geometric model of the self-excited ditching machine was imported from SolidWorks, and the particle factory was added. The size of the simulated soil tank is reduced to 500 × 300 × 300 mm based on the actual homemade bench test rig. The radius of simulated soil particles is enlarged and taken as R = 4 mm, and the soil particles are set to spherical particles; the total number of particles generated is 90,000. To reduce the porosity and make the particles fill more tightly, the particles are generated by applying a vibration with an amplitude of 1.5 mm and a frequency of 2 Hz in the length of the soil tank. The final model is shown in Figure 5. The material of the soil tank test rig is 45 steel, and the geometry of the self-excited vibration ditching machine is steel.

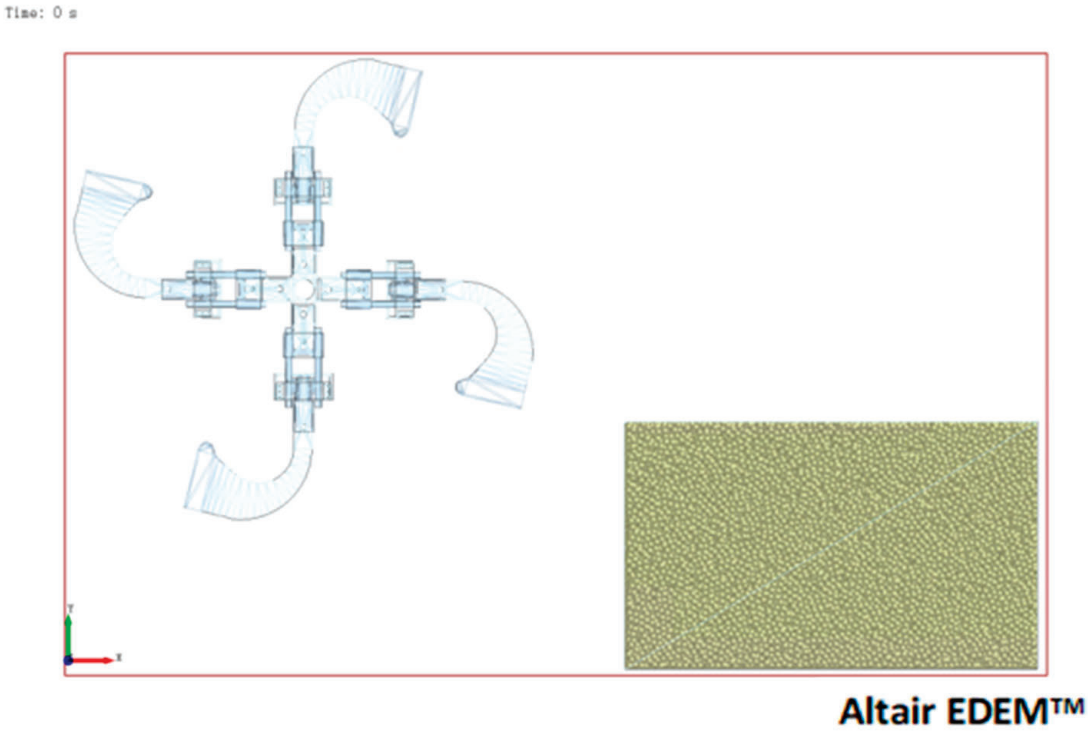

Figure 5. Edem(Discrete Element Method) discrete element simulation model of the self-excited vibration ditching machine.

2.3.3. Adams–Edem Coupling Simulation of Self-Excited Vibration Ditching Machine and Soil Interactions

To realize the interaction process between the self-excited ditching machine and soil, the Adams simulation model of the self-excited ditching machine is coupled with the Edem soil simulation model [31]. The coupled Adams–Edem simulation calculation is realized through the coupling interface. The Adams ditching blade parts rotate counterclockwise in the Edem interface to realize the contact, interaction, and separation between the ditching blade and the soil [32]. We set the simulation time to 5 s and the time step to 1000. In this way, we realize the self-initiated vibration ditching machine and soil interworking Adams–Edem coupling simulation (Figure 6).

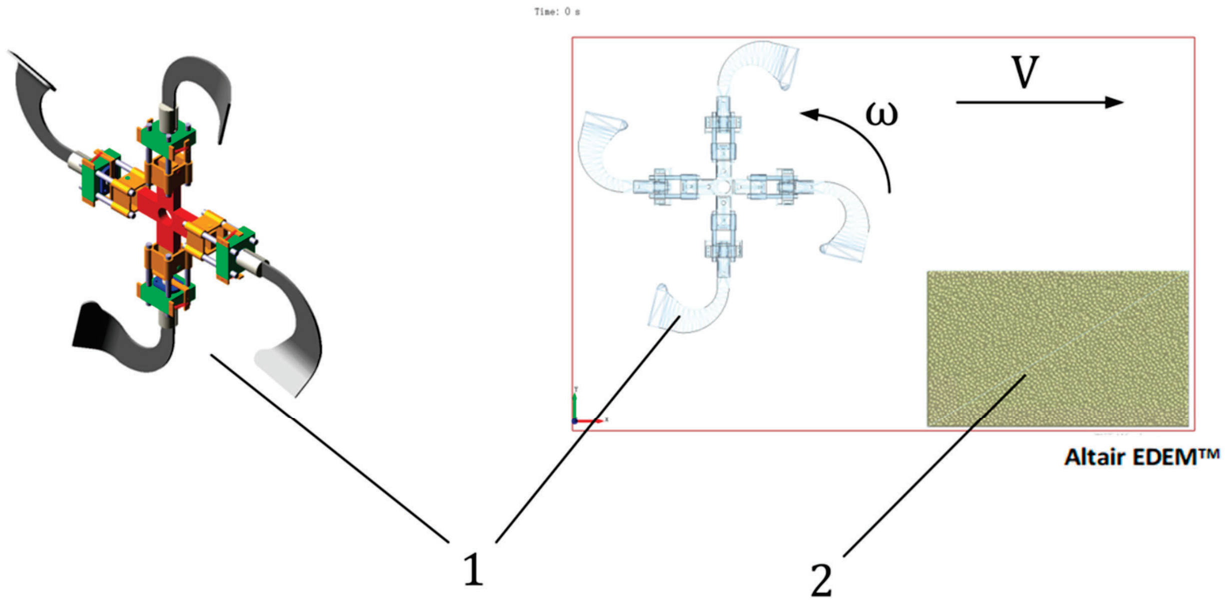

Figure 6. Self-excited(excitation forces exist inside the machine) vibration ditching machine and soil interaction Adams–Edem coupling simulation model: 1. self-excited vibration ditching machine, 2. soil model.

2.4. Bench Test Verification Platform

The overall structure and arrangement of the bench test verification platform are shown in Figure 7, and the overall length, width, and height of the test platform are 9.6, 1.5, and 1.3 m, respectively. The test platform selects the WDH-300Z torque rotating speed sensor for torque and speed detection. The torque range is 300 N-m, the rotating speed range is 5000 rpm, and the accuracy is 0.5. The torque rotating speed sensor combines a photoelectric switch and a speed measuring code to measure the rotating speed. When the speed measuring code turns continuously, the photoelectric switch outputs a pulse signal with a specific frequency. The speed of the measured shaft is calculated by the number of teeth of the code disk and the frequency of the output pulse signal, and the inverter controls the rotating speed of the ditching blade.

The soil used in the validation test platform was a clayey red soil, the average soil moisture was 16.8% in the 0–300 mm depth soil layer, the average soil compaction was 355 kPa, the measured wet density was 1.78×10^3 kg/m^3, the dry density was 1.55×10^3 kg/m^3, and the clay particle content was 60–70%.

(a) (b) (c)

Figure 7. Overall structure of the bench test rig: (**a**) bench test device, (**b**) ditching blade, and (**c**) attitude sensor mounting position; 1. rotator frame, 2. reducer support tube, 3. soil, 4. drive pulley,

5. coupling, 6. torque rotating speed sensor, 7. motor, 8. computer, 9. ditching depth adjustment support frame, 10. pusher motor, 11. gearbox, 12. rotating blade, 13. attitude sensor, 14. sensor bracket, and 15. blade.

In this study, the vibration characteristics of the three degrees of freedom of the blade roller axis (Y, Ry, and Rx directions), which are generated by the ditching blade, are collected in real-time with a bench validation test using attitude sensors. The size of the attitude sensor was 51.3 × 36 × 15 mm, the acceleration range was ±16 g, the angular velocity range was $\pm 2000^{\circ}/\mathrm{s}$, the angle range was $\pm 180^{\circ}$, and the measurement error was 0.01°. The device was purchased from Shenzhen Vetter Intelligence Co., Ltd. The Jy61 module was selected as the attitude sensor, with a sampling frequency reaching 200 Hz. The attitude sensor is attached to the sensor bracket of the device, which is fixed to the torsion beam of the device. The blade drives the vibration of the torsion beam, which, in turn, drives the vibration of the sensor bracket (Figure 7c). The attitude sensor is attached to the sensor mount of the device (Figure 5). The Y direction of the attitude sensor corresponds to the telescoping direction of the blade along the axial direction of the blade axis, and the Ry direction of the attitude sensor corresponds to the blade rotation direction around the blade axis. The Rx direction of the attitude sensor corresponds to the direction of blade oscillation relative to the blade axis. The attitude sensor communicates via Bluetooth, and the data are sent to the PC's higher-level computer software in real-time to record the Y-directional acceleration change, Y-directional angle change, and X-directional angle change in the attitude sensor. After each test, the data are output to the data file, and the information is postprocessed by MATLAB. The Y-directional acceleration data are integrated with the frequency domain and the de-DC component; then, the data are high-pass filtered to obtain the Y-directional displacement value. The Y-directional angle data and X-directional angle data are the de-DC components necessary to obtain the Ry-directional angular displacement value and Rx-directional angular displacement value.

2.5. Test Methods

To investigate the vibration characteristics of the internal dynamics of the self-excited ditching machine and to explain the mechanism of self-excited vibration for the reduction in resistance and energy consumption, the vibration characteristics of the ditching blade relative to the blade roller axis with three degrees of freedom (Y, Ry, and Rx directions) during the movement of the self-excited ditching machine are taken as the evaluation index. The effects of different factors (rotating speed, spring stiffness, spring damping coefficient, and blade weight) on the vibration characteristics in the Y, Ry, and Rx directions are analyzed. Each factor is set to 5 levels in the analysis, as shown in Table 4. The effects of different factors on the vibration characteristics in the Y, Ry, and Rx directions are analyzed by the dynamics theoretical model and Adams–Edem coupling simulation model. According to the effects of different factors on the Y-, Ry-, and Rx-directional vibration characteristics shown in the dynamics theory model and Adams–Edem coupling simulation model analysis results, a suitable rotating speed, spring stiffness, spring damping coefficient, and blade weight are selected for bench test verification. The attitude sensor collects the ditching blade vibration changes relative to the blade roller axis in the bench test. The experimental data are processed and analyzed by MATLAB to compare the Y-, Ry-, and Rx-directional vibration variations in the dynamics theoretical model and the Adams–Edem coupling simulation model to verify the accuracies of the established models. Finally, according to the actual working speed range of the small orchard ditching machine, the average input torque of the self-excited vibration ditching machine is compared with the nonself-excited vibration ditching machine under different actual working speeds to provide a reference for the actual working of the self-excited vibration ditching machine to reduce resistance and consumption.

Table 4. Levels of factors.

Number	Rotating Speed (rpm)	Spring Stiffness (N/mm)	Spring Damping Coefficient (Ns/m)	Blade Weight (kg)
1	100	5	0	1.0
2	200	10	0.03	1.5
3	300	15	0.3	2.0
4	400	20	3.0	2.5
5	500	25	30	3.0

3. Results and Discussion

3.1. Effects of Rotating Speed on the Vibration Characteristics in the Y, Ry, and Rx Directions

Since the rotating speed is the main parameter that affects the power consumption of ditching machines, this subsection investigates the effects of different rotating speeds on the vibration behaviors of self-excited ditching machines. The relationships between the vibration displacements in the Y, Ry, and Rx directions and the different rotating speeds are shown in Figure 8. The results show that the RMS value of the Y-directional vibration displacement increases from 0.266 to 7.052 mm. The average relative error between the simulated value and the theoretical value is 7.79% (Figure 8a). The RMS value of the Ry-directional vibration angular displacement increases from 1.475° to 7.182°. The average relative error between the simulated and theoretical values is 7.30% (Figure 8b). The RMS value of the Rx-directional vibration angular displacement increases from 1.169° to 5.70°. The average relative error between the simulated and theoretical values is 10.87% (Figure 8c).

To more comprehensively evaluate the vibration mechanism of the self-excited ditching machine, it is convenient to see the energy distribution of the vibration displacement at the frequency point and to obtain the frequency point that contributes the most to the vibration amplitude in the time domain, i.e., the primary vibration frequency of the blade. Power spectra analyses of the vibration displacement in the Y, Ry, and Rx directions are performed to obtain the vibration energy distributions in the frequency domain, as shown in Figure 9. The results show that the power spectral density (PSD) energy amplitudes of the vibration displacements in the Y, Ry, and Rx directions increase with increasing rotating speed, indicating that the Y-, Ry-, and Rx-directional vibration displacements also increase under these conditions. The results of the power spectra analysis are consistent with the results of the time domain analysis. The Y-directional vibration frequency increases from 1.63 to 8.85 Hz, and the change in the rotating speed is the same. This phenomenon is conducive to the vibration of both the ditching blade and the soil in the vertical soil direction so that the soil is broken by the vibration and separation of the ditching blade; thus, the total traction resistance is reduced, which reduces the overall resistance and losses. These phenomena occur because the centripetal force from the rotation of the self-excited vibration device affects the Y direction of the ditching device, causing the self-excited vibration of the spring in the Y direction so that the Y-directional vibration frequency and rotating speed are the same. The vibration frequency in the Rx direction is maintained at 2.24 Hz, and the frequency in the Ry direction is held at 1.73 Hz. The vibration frequency in the Rx direction and the vibration frequency in the Ry direction remain the same as the rotating speed increases. The reason for this phenomenon is that the rotation of the self-excited vibration device causes initial perturbations in the Rx and Ry directions of the spring from the rotation, leading to the self-excited vibration of the Rx and Ry springs. There are no forces in other directions in the Rx and Ry directions, so a fixed vibration frequency is maintained.

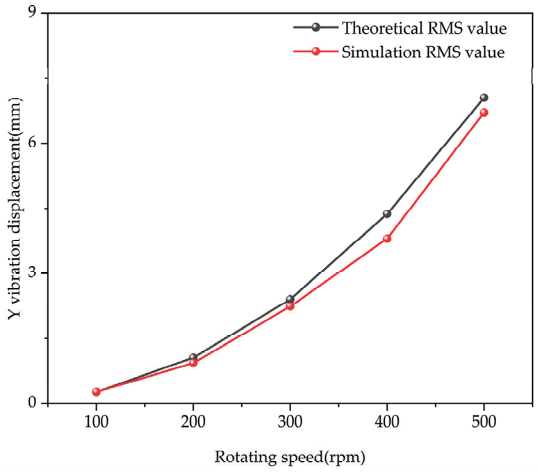

(**a**) Y direction

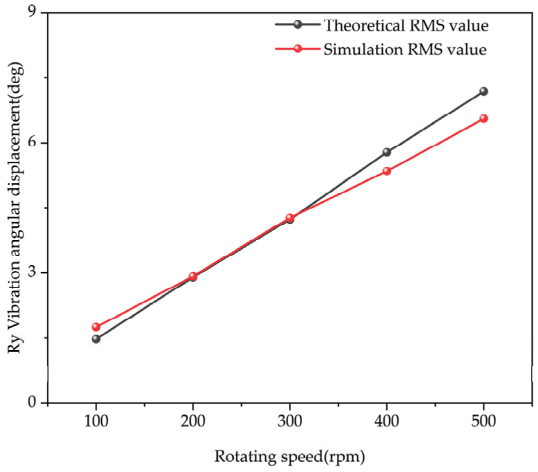

(**b**) Ry direction

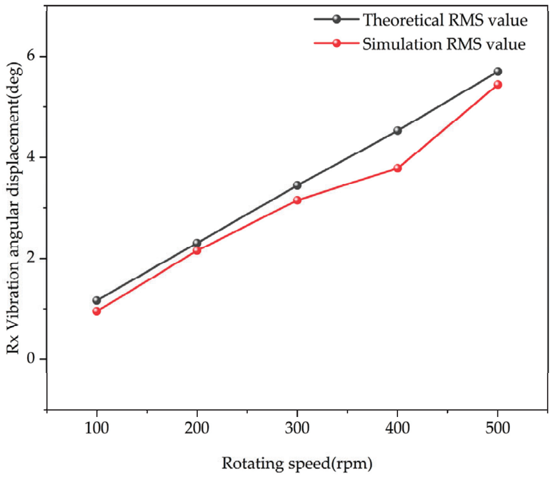

(**c**) Rx direction

Figure 8. Variations in the vibration displacement with rotating speed in the Y, Ry, and Rx directions: (**a**) Y direction, (**b**) Ry direction, and (**c**) Rx direction. (the spring stiffness is specified as 15 N/mm, the spring damping factor is 0.03 Ns/m, and the blade weight is 1.0 kg).

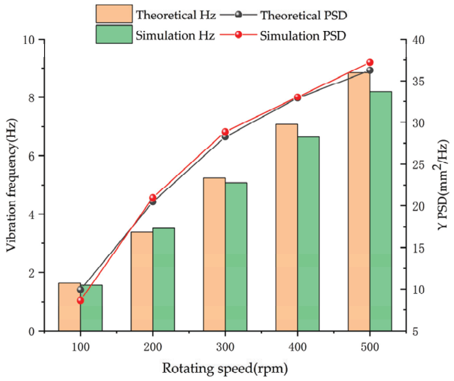

(**a**) Y direction

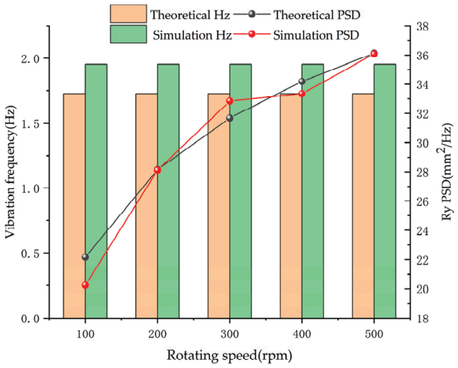

(**b**) Ry direction

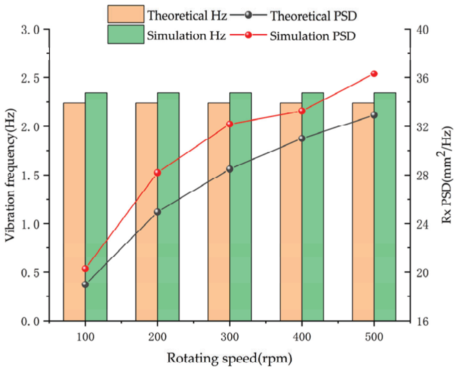

(**c**) Rx direction

Figure 9. Variations in the PSDs of the vibration displacements with different rotating speeds in the Y, Ry, and Rx directions: (**a**) Y direction, (**b**) Ry direction, and (**c**) Rx direction. (the spring stiffness is specified as 15 N/mm, the spring damping factor is 0.03 Ns/m, and the blade weight is 1.0 kg).

The Ry and Rx directions of vibration mainly achieve a certain degree of flexural obstacle avoidance in the actual working process, increase the effect of soil breaking, and reduce the amount of soil throwing in the process of ditching. Under a constant linear spring stiffness, the equivalent torsional stiffness and rotational angle are nonlinear. Nevertheless, the rotational angle is within 5°, and the equivalent torsional stiffness is considered to remain constant, so the angular displacements in the Ry and Rx directions of vibration should be kept within 5° to the greatest possible extent [33]. Therefore, to maintain stability in the Ry and Rx directions of vibration during ditching, the rotating speed should be maintained in the range of 300–400 rpm.

3.2. Effects of Spring Stiffness on the Vibration Characteristics in the Y, Ry, and Rx Directions

A self-excited vibratory ditching machine produces adaptive deformation using a spring in response to changes in the external load, and the spring stiffness affects the force characteristics of the blade. Therefore, in this subsection, we investigate the effects of different spring stiffnesses on the vibration of a self-excited ditching machine. The relationships between the vibration displacements in the Y, Ry, and Rx directions and the spring stiffnesses are shown in Figure 10. The results show that the RMS value of the Y-directional vibration displacement decreases from 7.70 to 1.478 mm. The average relative error between the simulated and theoretical values is 10.68% (Figure 10a). The RMS value of the Ry-directional vibration angular displacement decreases from 6.84° to 3.46°. The average relative error between the simulated and theoretical values is 11.82% (Figure 10b). The RMS value of the Rx-directional vibration angular displacement decreases from 5.43° to 2.78°. The average relative error between the simulated and theoretical values is 8.29% (Figure 10c).

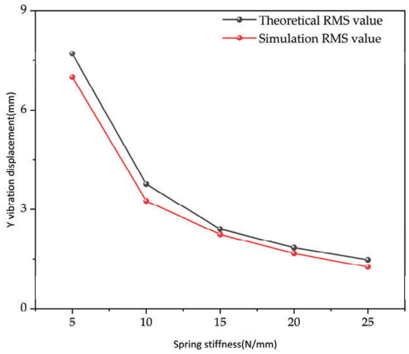

(**a**) Y direction

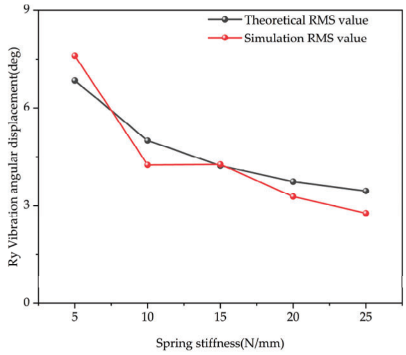

(**b**) Ry direction

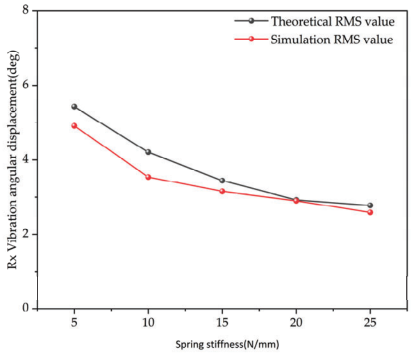

(**c**) Rx direction

Figure 10. Variations in the vibration displacements with different spring stiffnesses in the Y, Ry, and Rx directions: (**a**) Y direction, (**b**) Ry direction, and (**c**) Rx direction. (the rotating speed is specified as 300 rpm, the spring damping factor is 0.03 Ns/m, and the blade weight is 1.0 kg).

Power spectra analyses of the vibration displacements in the Y, Ry, and Rx directions are performed to obtain the vibration energy distributions in the frequency domain, as shown in Figure 11. The results show that as the spring stiffness increases, the PSD energy amplitudes of the vibration displacements in the Y, Ry, and Rx directions decrease, indicating that the vibration displacements in the Y, Ry, and Rx directions decrease as the spring stiffness increases. The results of the power spectra analyses remain consistent with the results of the time domain analysis. The Y-directional vibration frequency is maintained at approximately 5.24 Hz, mainly due to the Y-directional vibration coming from the centripetal force acting as the excitation force; furthermore, the rotating speed influences the Y-directional vibration frequency, and the influence of the spring stiffness is relatively slight. The Rx-directional vibration frequency increases from 1.29 to 2.89 Hz, and the Ry-directional vibration frequency increases from 1.00 to 2.23 Hz. The Ry-directional vibration frequency increases from 1.46 to 2.93 Hz. The reason for this is that the Rx- and Ry-directional vibrations come from the self-excited vibration caused by the initial disturbance of the spring, so the spring stiffness exhibits direct effects on the vibration frequencies in the Rx and Ry directions; the stiffer the spring is, the larger the vibration frequency.

The self-excited vibration ditching blade, soil contact, and vibration frequency, when increasing in a certain range, are conducive to the detachment of the soil adhering to the blade due to the rapid vibration of the machine, thereby reducing the friction between the blade and the soil. In contrast, the internal stress of the soil increases, and the greater the internal stress is, the easier the soil is broken, thus reducing the total traction resistance to reduce overall resistance and energy consumption. Thus, the vibration frequencies in the Ry and Rx directions should be increased as much as possible while ensuring their stability. Therefore, the spring stiffnesses in the Ry and Rx directions should be kept in the range of 20–25 N/mm. The Y-directional vibration frequency remains constant as the spring stiffness increases, and the Y-directional vibration displacement changes to a greater extent within the spring stiffness range of 5–10 N/mm, indicating that the Y-directional vibration is rapid within this range; thus, the Y-directional spring stiffness should be maintained within this range.

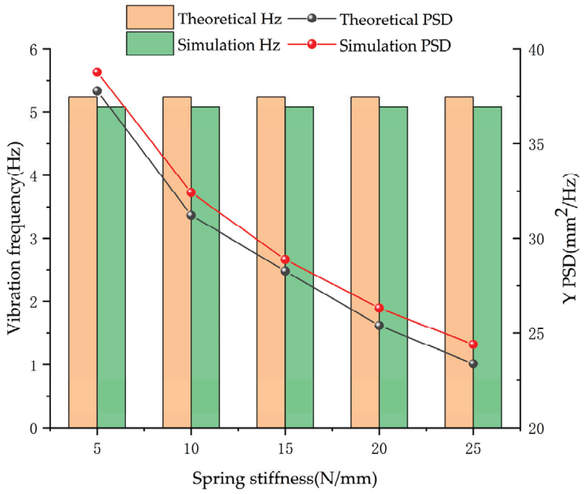

(**a**) Y direction

Figure 11. *Cont.*

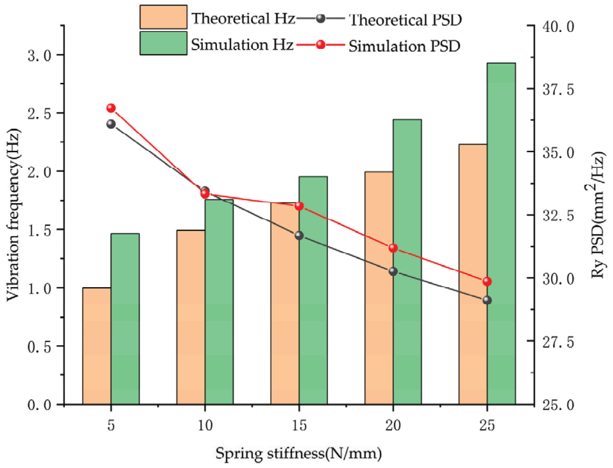

(**b**) Ry direction

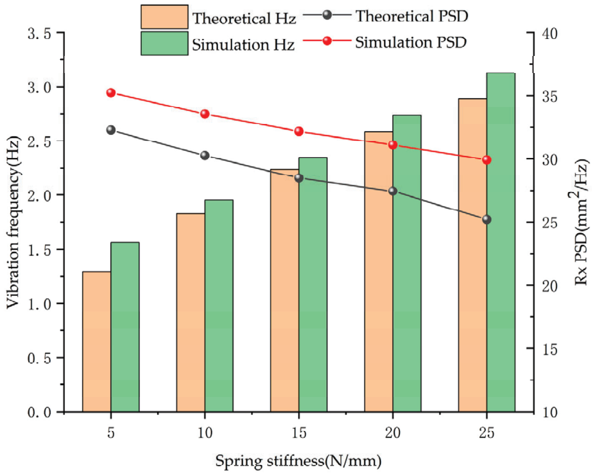

(**c**) Rx direction

Figure 11. Variations in the vibration displacement PSDs with different spring stiffnesses in the Y, Ry, and Rx directions: (**a**) Y direction, (**b**) Ry direction, and (**c**) Rx direction. (the rotating speed is specified as 300 rpm, the spring damping factor is 0.03 Ns/m, and the blade weight is 1.0 kg).

3.3. *Effects of Spring Damping Coefficients on the Vibration Characteristics in the Y, Ry, and Rx Directions*

Spring damping is an inherent property of the spring, and its size affects the self-excited vibration amplitude of the ditching machine, controlling whether the amplitude is fast or slow. Therefore, this subsection investigates the effects of different spring damping coefficients on the vibration behaviors of self-excited vibratory ditching machines. In the analysis, the relationships between the vibration displacements in the Y, Ry, and Rx directions and the spring damping coefficients are shown in Figure 12. The results show that the RMS value of the Y-directional vibration displacement decreases from 2.49 to 1.91 mm. The average relative error between the simulated and theoretical values is 5.58% (Figure 12a). The RMS value of the Ry-directional vibration angular displacement decreases from 4.23° to 3.74°. The average relative error between the simulated and theoretical values is 2.33% (Figure 12b). The RMS value of the Rx-directional vibration angular displacement decreases from 3.44° to 3.11°. The average relative error between the simulated and theoretical values is 10.34% (Figure 12c).

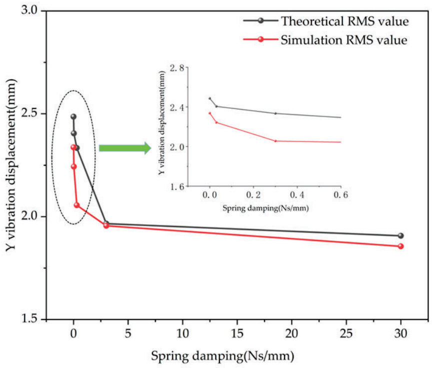

(**a**) Y direction

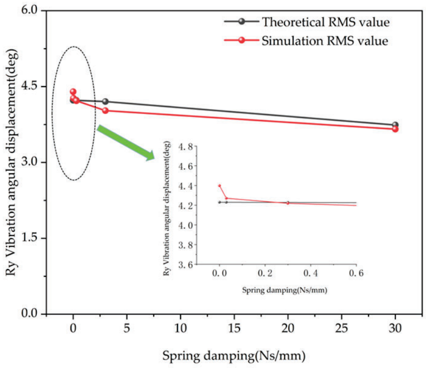

(**b**) Ry direction

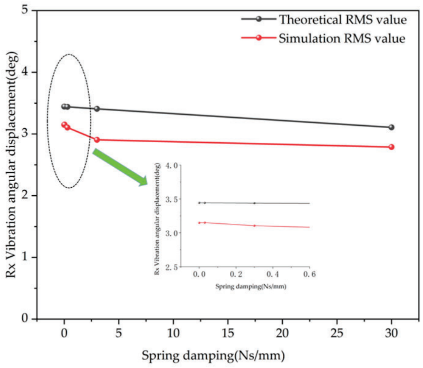

(**c**) Rx direction

Figure 12. Variations in the vibration displacements with different spring damping coefficients in the Y, Ry, and Rx directions: (**a**) Y direction, (**b**) Ry direction, and (**c**) Rx direction. (the rotating speed is specified as 300 rpm, the spring stiffness factor is 15 N/mm, and the blade weight is 1.0 kg).

Power spectra analyses of the vibration displacements in the Y, Ry, and Rx directions were performed to obtain the vibration energy distributions in the frequency domain, as shown in Figure 13. The results show that the PSD energy amplitudes of the vibration displacements in the y, Ry, and Rx directions decrease as the spring damping increases, indicating that the vibration displacement decreases in the Y, Ry, and Rx directions as the spring damping increases, and the results of the power spectra analyses remain consistent with the results of the time domain analysis. The Y-directional vibration frequency is maintained at 5.24 Hz, the Ry-directional vibration frequency is maintained at 1.73 Hz, and the Rx-directional vibration frequency is maintained at 2.24 Hz. These findings indicate that the spring damping coefficient slightly influences the vibration frequencies in the Y, Ry, and Rx directions.

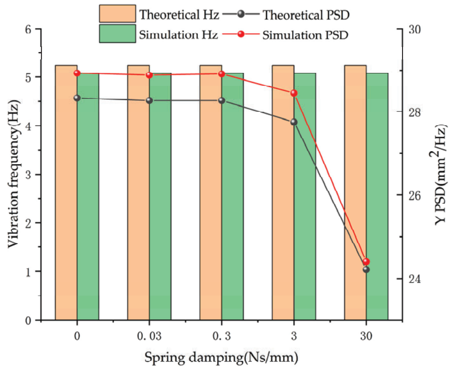

(**a**) Y direction

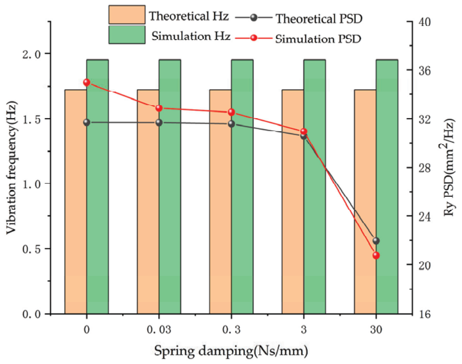

(**b**) Ry direction

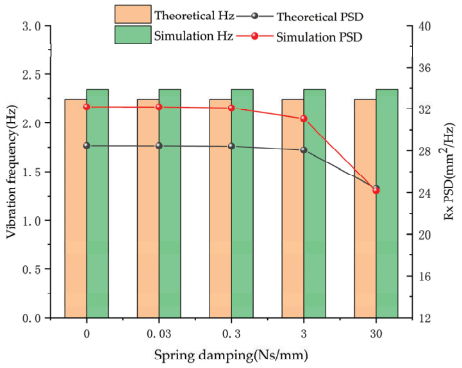

(**c**) Rx direction

Figure 13. Variations in the vibration displacement PSDs with different spring damping coefficients in the Y, Ry, and Rx directions: (**a**) Y direction, (**b**) Ry direction, and (**c**) Rx direction. (the rotating speed is specified as 300 rpm, the spring stiffness factor is 15 N/mm, and the blade weight is 1.0 kg).

Since there is no external force, the vibration in both the Ry and Rx directions stops over time, and the greater the spring damping is, the shorter the stopping time is for the vibration in the Ry and Rx directions. The Y-, Ry-, and Rx-directional vibration frequencies remain the same with increasing spring stiffness; thus, the spring damping coefficient, to a certain extent, hinders the vibration in the Y, Ry, and Rx directions. In the selection of the spring damping coefficient, a small damping coefficient in the range of 0–0.3 NS/mm should be chosen to slow the stopping time for vibration in the Ry and Rx directions.

3.4. Effects of the Blade Weight on the Vibration Characteristics in the Y, Ry, and Rx Directions

As the main component of a self-excited ditching machine, the weight of the ditching blade affects its vibration amplitude and speed; in this subsection, we investigate the effects of different blade weights on the vibration of a self-excited ditching machine. In the analysis, the relationships between the vibration displacement in the Y, Ry, and Rx directions and the different weights of the blade are shown in Figure 14. The results show that the Y-directional vibration displacement increases from 2.41 to 5.06 mm. The average relative error between the simulated and theoretical values is 4.69% (Figure 14a). The RMS value of the Ry-directional vibration angular displacement increases from 4.23° to 6.84°. The average relative error between the simulated and theoretical values is 4.00% (Figure 14b). The RMS value of the Rx-directional vibration angular displacement increases from 3.44° to 7.58°. The average relative error between the simulated and theoretical values is 5.20% (Figure 14c).

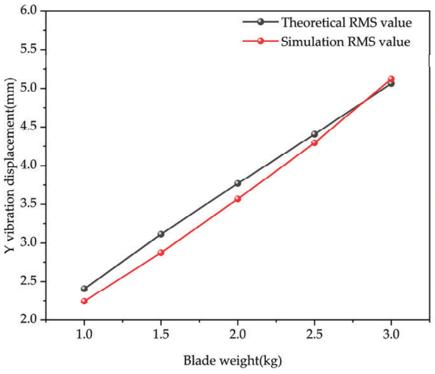

(**a**) Y direction

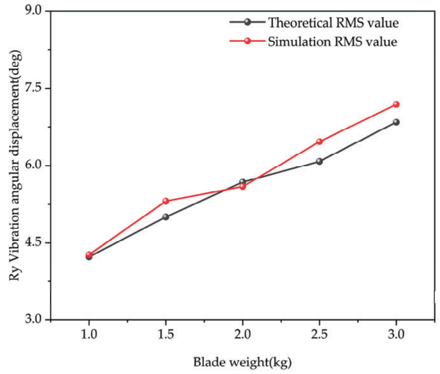

(**b**) Ry direction

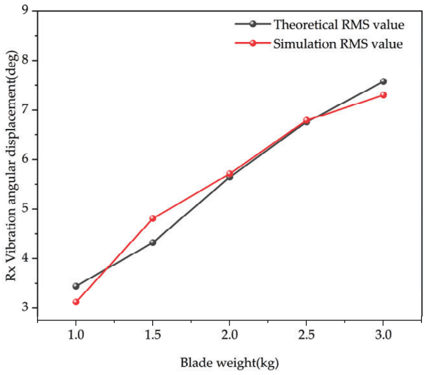

(**c**) Rx direction

Figure 14. Variations in the vibration displacements with different blade weights in the Y, Ry, and Rx

directions: (**a**) Y direction, (**b**) Ry direction, and (**c**) Rx direction. (the rotating speed is specified as 300 rpm, the spring stiffness factor is 15 N/mm, and the spring damping is 0.03 Ns/m).

Power spectra analyses of the vibration displacements in the Y, Ry, and Rx directions are performed to obtain the vibration energy distributions in the frequency domain, as shown in Figure 15. The results show that the PSD energy amplitudes of the vibration displacements in the Y, Ry, and Rx directions increase with increasing blade weight; thus, the vibration displacements in the Y, Ry, and Rx directions increase with increasing blade weight, and the results of the power spectra analyses are consistent with those of the time domain analysis. The vibration frequency in the Y direction is maintained at 5.238 Hz, which indicates that its vibration frequency is slightly affected by the weight of the blade. The vibration frequency in the Ry direction decreases from 1.73 to 1.00 Hz, and the vibration frequency in the Rx direction decreases from 2.24 to 1.67 Hz. These phenomena occur because the vibration in the Ry and Rx directions originates from the spring due to the initial disturbance caused by self-excited vibration. The blade weight exhibits a direct impact on its vibration frequency. The greater the weight of the blade, the lower its vibration frequency, resulting in decreasing vibration frequencies in the Ry and Rx directions with increasing blade weight.

With the increase in blade weight, the vibration displacements in the Y, Ry, and Rx directions increase linearly. The increase in the blade weight decreases the vibration frequency in the Ry and Rx directions, which is not conducive to detaching the adhered soil from the blade, thus increasing the blade and soil resistance. This phenomenon decreases the internal stress of the soil, which is not conducive to breaking the soil, making the total traction resistance increase. Therefore, the weight of the blade should be reduced as much as possible while keeping the vibration stable by selecting a weight of approximately 1.0 kg.

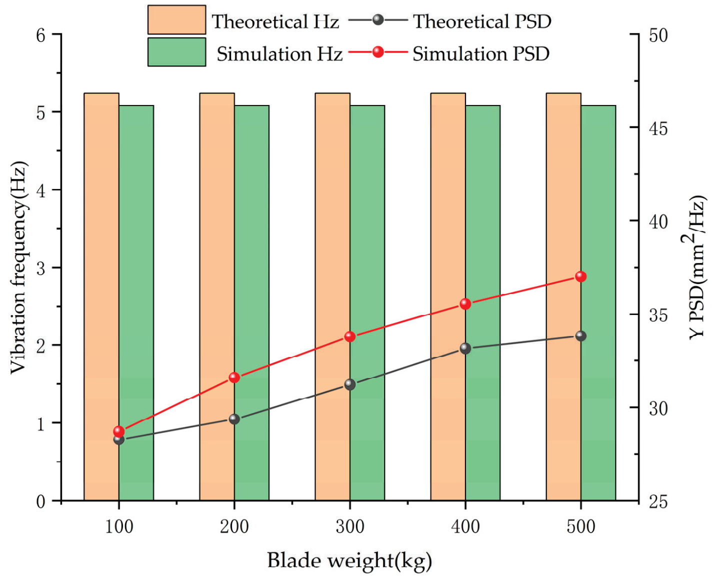

(**a**) Y direction

Figure 15. *Cont.*

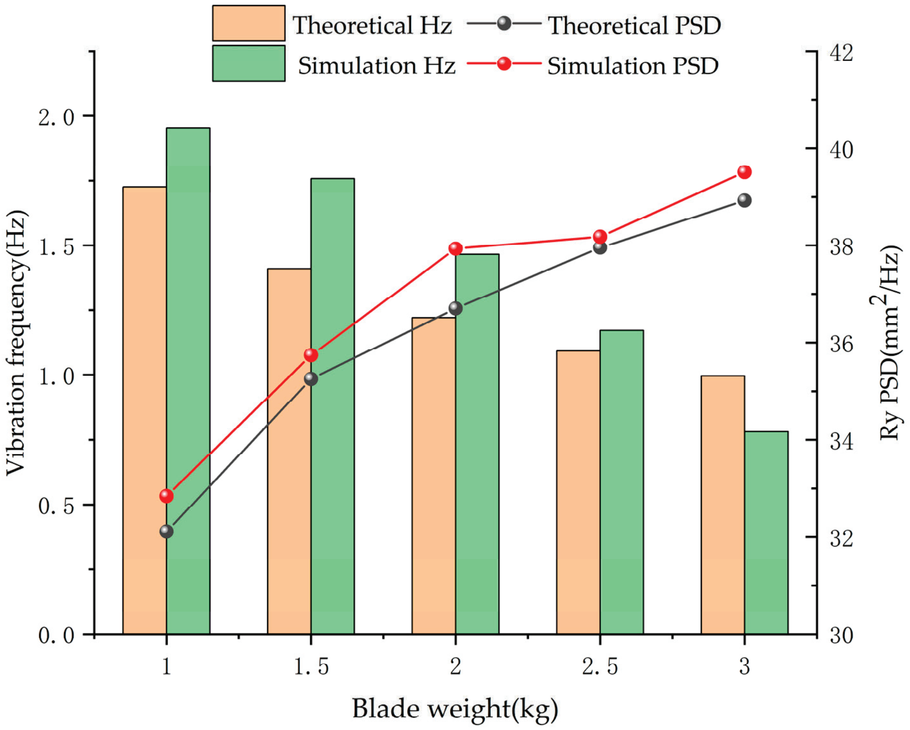

(**b**) Ry direction

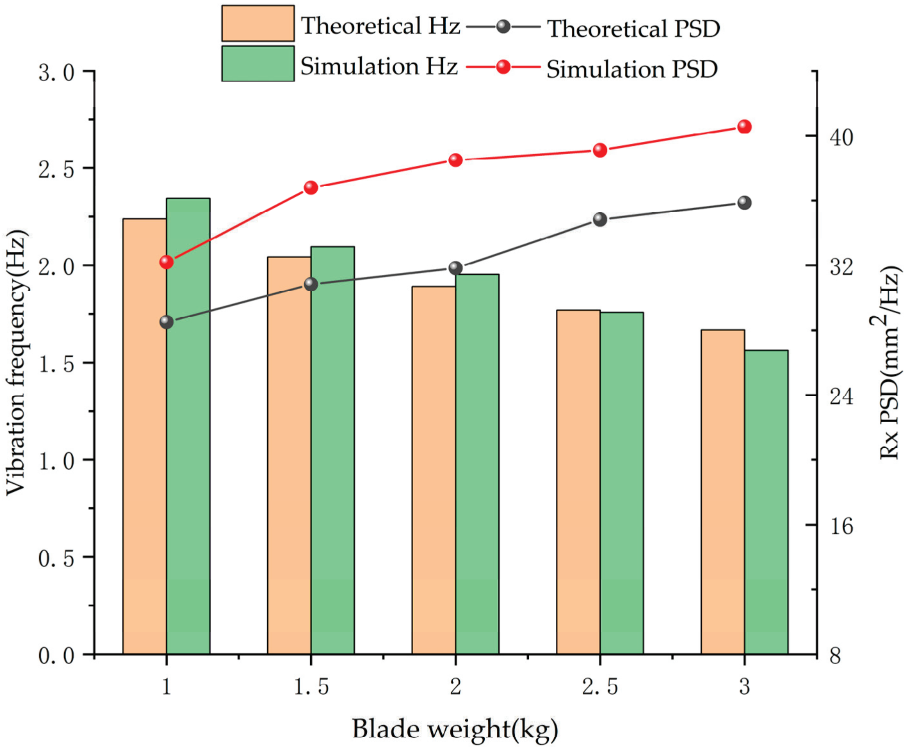

(**c**) Rx direction

Figure 15. Variations in the PSDs of vibration displacements with different blade weights in the Y,

Ry, and Rx directions: (**a**) Y direction, (**b**) Ry direction, and (**c**) Rx direction. (the rotating speed is specified as 300 rpm, the spring stiffness factor is 15 N/mm, and the spring damping is 0.03 Ns/m).

3.5. Test Verification

To verify the accuracies of the derived dynamics theoretical model and the Adams–Edem coupling simulation model, the rotating speed of the ditching test stand is set to a constant value of 300 rpm; additionally, the blade is turned counterclockwise, and the blade weight is 1.0 kg according to the results of the analyses of the effects of different parameters on the vibration characteristics in the Y, Ry, and Rx directions. Suitable springs are selected for the Y, Ry, and Rx directions, and extension and compression experiments are performed on a universal testing machine for extension and compression springs. Each experiment was repeated three times. The linear stiffness of the spring is selected by the MATLAB data fitting toolbox, as shown in Table 5.

Table 5. Spring stiffness test results.

Spring Type	Spring Size (mm) (Wire Diameter × Diameter × Length)	Spring Stiffness (N/mm)	Spring Damping (NS/mm)	Degree of Freedom
Compression spring 1	1.2 × 6 ×12	22	0.03	Rx
Compression spring 2	1.6 × 13 × 35	6.2	0.03	Y
Tension spring 1	1.4 × 7 × 24	24	0.03	Ry

The self-excited vibration ditching machine is bench-tested, and the test results collected from the sensors are processed and analyzed by MATLAB to obtain the variations in the vibration displacements in the Y, Ry, and Rx directions, as shown in Figure 16. Table 6 features the results of the time and frequency domain analyses of the Y-, Ry-, and Rx-direction vibrations. In the bench test, the RMS value of the vibration displacement in the Y direction is 6.05 mm, the RMS value of the vibration angular displacement in the Ry direction is 3.31°, and the RMS value of the vibration angular displacement in the Rx direction is 3.24°. The relative error between the RMS value of the Y-directional vibration displacement test and the theoretical RMS value is 2.85%, and the relative error with the simulation is 1.69%. The relative error between the RMS value of the Ry-directional vibration angular displacement test and the theoretical RMS value is 4.02%, and the relative error with the simulation is 8.82%. The relative error between the RMS value of the Rx-directional vibration angular displacement test and the theoretical RMS value is 10.99%, and the relative error with the simulation is 5.88%. The difference between the vibration frequency in the Y direction and the theoretical vibration frequency is 0.20 Hz, and the difference between the vibration frequency and the simulation is 0.28 Hz. The difference between the vibration frequency in the Ry direction and the theoretical vibration frequency is 0.12 Hz, and the difference between the vibration frequency and the simulation is 0.39 Hz. The difference between the vibration frequency in the Rx direction and the theoretical vibration frequency is 0.19 Hz, and the difference between the vibration frequency and the simulation is 0.19 Hz. Test, simulation, and theoretical analyses of the existence of errors are performed mainly because the slight vibration of the test platform affects the measurements of the sensor, resulting in a certain error and affecting the ditching blade vibration directions and frequencies in the Y, Ry, and Rx directions. The test shows that the theoretical model of self-excited ditching machine dynamics and the Adams–Edem coupling simulation model derived in this paper can better represent the internal motion mechanisms of self-excited ditching machines.

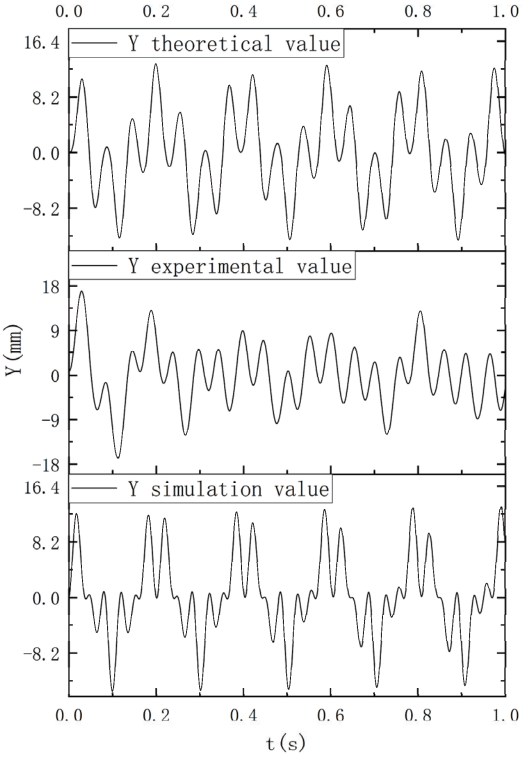

(**a**) Y direction

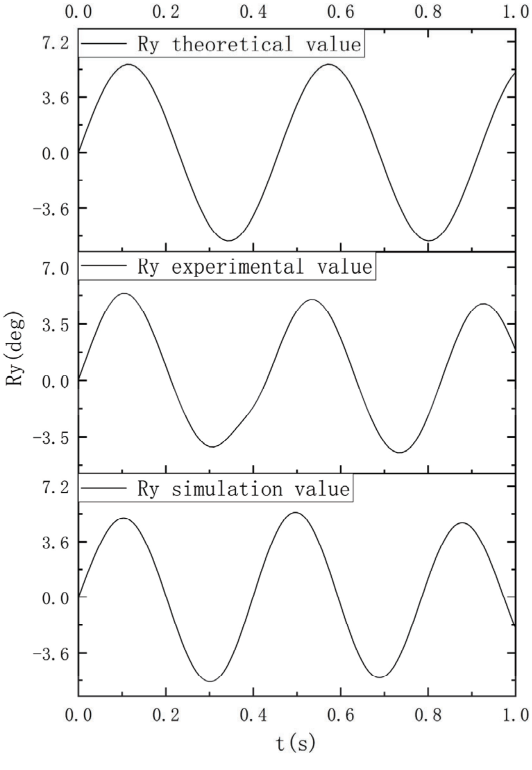

(**b**) Ry direction

Figure 16. *Cont*.

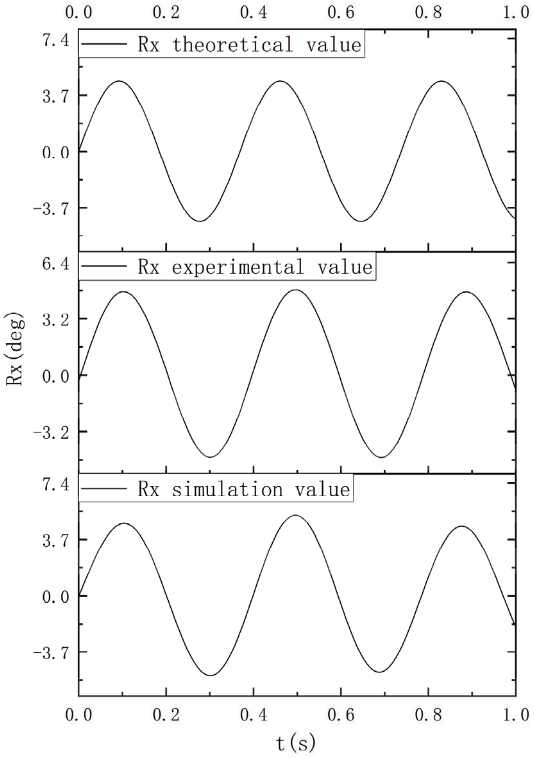

(**c**) Rx direction

Figure 16. Experimental verification of the variations in vibration displacements in the Y, Ry, and Rx directions: (**a**) Y direction, (**b**) Ry direction, and (**c**) Rx direction.

3.6. Comparison Analysis of Ditching Torque

To elaborate on the self-excited vibration ditching machine compared with the nonself-excited vibration ditching machine, the process of ditching has a better role in reducing resistance and consumption. According to the normal travel speed of small orchard ditching machine work, the test bench travel speed is set to 0.4 m/s, and the cutter disc turns counterclockwise. According to the actual working speed range and design rotary speed range of 180–500 rpm, five levels are designed, 180 rpm, 220 rpm, 330 rpm, 440 rpm, and 500 rpm, and the average input torque of the ditching machine is used as the evaluation index of torque comparison analysis to elaborate the self-excited vibration ditching machine in the process of ditching. It is more conducive to the reduction of resistance and consumption. To minimize the error, each test was repeated three times to find the average value. Each time before the start of the test, the sensor calibration, soil conditioning, tamping, and ditching depth adjustments (using the soil tamper back and forth to compact the soil to maintain the soil moisture content (14–17%, measured by moisture content instrument), soil firmness (355 kPa, measured by TYD-2 type soil firmness measuring instrument), and ditching depth (80 mm) of each test) were basically the same.

The self-excited ditching machine and nonself-excited ditching machine were tested on the bench, and the average input torque variation of the self-excited ditching machine and nonself-excited ditching machine were obtained by processing and analyzing the test results collected by the sensor through MATLAB, as shown in Figure 17.

Table 6. Vibration analyses in the Y, Ry, and Rx directions under test verification conditions.

	RMS Value			**PSD**			**Vibration Frequency**		
	Y (mm)	**Ry (deg)**	**Rx (deg)**	**Y (mm^2/Hz)**	**Ry (deg^2/Hz)**	**Rx (deg^2/Hz)**	**Y (Hz)**	**Ry (Hz)**	**Rx (Hz)**
Theoretical analysis	6.23	3.44	2.89	36.80	28.36	26.89	5.00	2.18	2.71
Experimental analysis	6.05	3.31	3.24	36.26	26.80	25.18	4.80	2.30	2.50
Simulation analysis	5.948	3.60	3.43	37.03	30.75	30.56	5.08	2.69	2.69

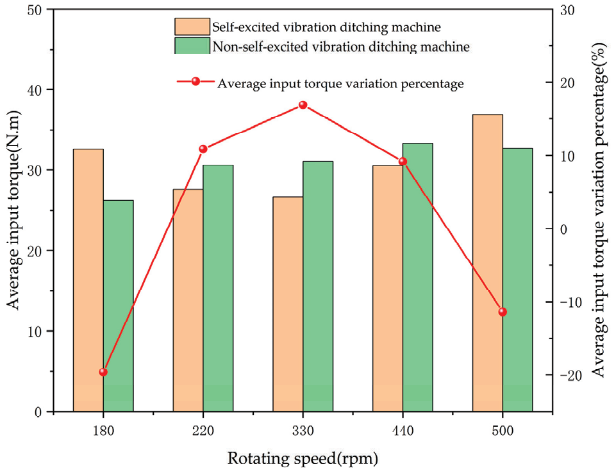

Figure 17. Variation in the average input torque with rotational speed for the self-excited vibratory ditching machine and the nonself-excited vibratory ditching machine.

The results showed that the average input torque of the self-excited vibration ditching method was significantly lower than that of the nonself-excited vibration ditching method in the range of 220–500 rpm under the test conditions, and the maximum ratio of 16.92% was reduced at 330 rpm. However, the average input torque of the self-excited ditching method is higher than that of the nonself-excited ditching method at low speed (180 rpm) and high speed (500 rpm). The test results of the average input torque of the self-excited vibration ditching machine compared with the results of the nonself-excited ditching machine showed that the self-excited vibration ditching machine helps to reduce the energy consumption of ditching in a suitable speed range.

At the same time, the Adams–Edem coupled simulation model was set with a maximum depth of entry of the self-excited ditching knife of 80 mm, a linear movement speed of the knife shaft of 0.4 m/s, the knife shaft speed as in the bench test, and a data saving interval of 0.01 s. Five sets of simulation tests were conducted, and the test results were obtained in the data analysis module to obtain the average input torque variation of the knife shaft and compare it with the average input torque variation of the self-excited ditching knife in the bench test. The average input torque variation of the knife shaft is compared with the average input torque variation of the self-excited ditching test, as shown in Figure 18.

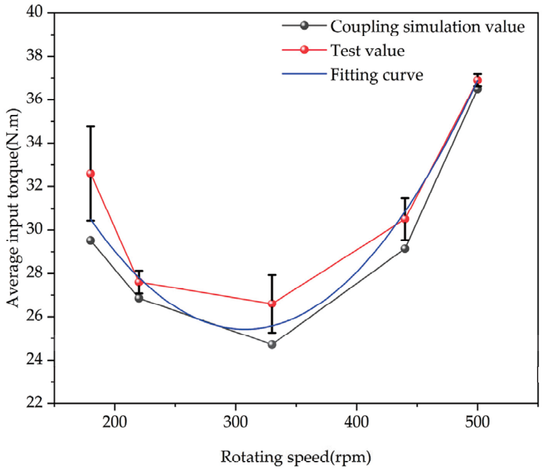

Figure 18. Average input torque versus speed for the test and Adams–Edem coupled simulation.

The results show that the average input torque of the tool decreases and then increases as the speed increases, and it reaches the lowest value of 25.1 N.m at 330 rpm. The simulated value has the same trend as the test value and reaches the lowest value of 24.72 N.m at 330 rpm and the maximum relative error of 9.45% at 180 rpm. The operating effectiveness of trenching can be evaluated in terms of trenching depth, trenching width, and trenching quality, so the lower torque indicates more energy saving with the same effect of action. Fitting the analysis to the data pairs gives: $y = 54.784 - 0.191x + 3.100 \times 10^{-4}\ x^2$, $R^2 = 0.994$ which indicates that the simulation results can better reflect the change law of rototill power consumption and more accurately express the average input torque value; hence, the Adams–Edem coupled simulation model established in this paper is reliable for studying the vibration characteristics and torque change of the self-excited vibration ditching machine. The bench test value is generally larger than the simulated value, which may be due to the additional power consumption caused by the soil containing stones, transmission system friction, and overcoming the forward resistance of the test cart.

4. Conclusions

1. The vibration displacements in the Y, Ry, and Rx directions increase with increasing rotating speed and ditching blade weight values and decrease with increasing spring stiffness and spring damping coefficient values.
2. The Y-directional vibration frequency increases with increasing rotating speed and remains the same with increasing spring stiffness, spring damping coefficient, and ditching blade weight values. The vibration frequencies in the Ry and Rx directions increase with increasing spring stiffness and ditching blade weight and remain the same with increasing rotating speed and spring damping coefficients.
3. An analysis of the dynamics theoretical model shows that the theoretical values of the established dynamics model of the self-excited vibration ditching machine change in line with the experimental values; the relative error of the vibration displacement in the Y direction is 2.85%, the relative error of the vibration angular displacement in the Ry direction is 4.02%, and the relative error of the vibration angular displacement in the Rx direction is 10.99%. The differences in the vibration frequencies in the Y, Ry, and Rx directions are 0.20, 0.12, and 0.19 Hz, respectively. This observation shows that the theoretical dynamics model has high accuracy.
4. An analysis of the Adams–Edem coupling simulation model shows that the established simulation values are consistent with the experimental values of the self-excited vibration ditching machine. The relative error of the vibration displacement in the Y direction is 1.69%, the relative error of the vibration angular displacement in the Ry direction is 8.82%, and the relative error of the vibration angular displacement in the Rx direction is 5.88%. The difference between the Y-, Ry-, and Rx-directional vibration frequencies and the simulated vibration frequencies is 0.28, 0.39, and 0.19 Hz, respectively. This observation shows that the Adams–Edem coupling simulation model has high accuracy.
5. The comparative analysis of the rotational torque shows that the self-excited vibratory ditching machine helps reduce the ditching energy consumption by up to 16.92% compared with the nonself-excited vibratory ditching machine in the suitable speed range (220–440 rpm) during the ditching process. The Adams–Edem coupling simulation value of self-excited ditching implementation and soil interaction is consistent with the experimental value, and the maximum relative error is 9.45%, which indicates that the Adams–Edem coupling simulation model has high accuracy.
6. We also considered preparing prototypes related to the new self-excited vibratory ditching device in order to conduct experimental tests in different soil types and conditions in order to evaluate the ditching quality of the self-excited vibratory ditching prototype and to check the final issues (formation of compacted soil layers, degree of soil fining, torque, and energy consumption) related to the use of the self-excited vibratory ditching prototype in real field conditions.

Author Contributions: Conceptualization, J.L. and G.H.; methodology, J.L.; software, J.L. and H.L.; validation, J.L., H.L. and Y.C. (Yingyi Chen); formal analysis, J.L., H.L. and P.L.; investigation, J.L.; resources, J.L. and G.H.; data curation, H.L.; writing—original draft preparation, J.L. and H.L.; writing—review and editing, J.L., G.H. and H.L.; visualization, G.H., Q.Z. and Y.C. (Ying Cheng); supervision, G.H. and Z.Y.; project administration, J.L.; funding acquisition, J.L. All authors have read and agreed to the published version of the manuscript.

Funding: This research was funded by the Guangdong Laboratory for Lingnan Modern Agriculture under Grant [NZ2021040] and [NZ2021009], the China Agriculture Research System under Grant [CARS-32], the Special Project of Rural Vitalization Strategy of Guangdong Academy of Agricultural Sciences under Grant [TS-1-4], and the Guangdong Provincial Modern Agricultural Industry Technology System under Grant [2021KJ123].

Data Availability Statement: The data used to support the findings of this study are included within the article.

Conflicts of Interest: No potential conflict of interest were reported by the authors.

References

1. Du, Z.; Chen, Y.; Zhang, J.; Han, X.; Geng, A.; Zhang, Z. Development status and prospects of rotary farm machinery in domestic and abroad. *J. Chin. Agric. Mech.* **2019**, *40*, 43–47. (In Chinese) [CrossRef]
2. Zhao, Y. Research of Effect on Operational Performance of Structure And Motion Parameters of The Rotary Tiller. Master's Thesis, Jilin Agricultural University, Changchun, China, May 2015.
3. Jia, H.; Wang, W.; Chen, Z.; Zheng, T.; Zhang, P.; Zhuang, J. Research Status and Prospect of Soil-engaging Components Optimization for Agricultural Machinery. *Trans. Chin. Society Agric. Mach.* **2017**, *48*, 1–13. (In Chinese)
4. Zhao, J.L.; Lu, Y.; Guo, M.Z.; Fu, J.; Wang, Y.J. Design and experiment of bionic stubble breaking-deep loosening combined tillage machine. *Int. J. Agric. Biol. Eng.* **2021**, *14*, 123–134. [CrossRef]
5. Xiao, M.; Wang, K.; Yang, W.; Wang, W.; Jiang, F. Design and Experiment of Bionic Rotary Blade Based on Claw Toe of Gryllotalpa orientalis Burmeister. *Trans. Chin. Society Agric. Mach.* **2021**, *52*, 55–63. (In Chinese)
6. Sun, J.; Chen, H.; Wang, Z.; Ou, Z.; Yang, Z.; Liu, Z.; Duan, J. Study on plowing performance of EDEM low-resistance animal bionic device based on red soil. *Soil Tillage Res.* **2020**, *196*, 104336. [CrossRef]
7. Guo, J. Research on working performance of serrated and rotary blades on straw returning to field machine. Ph.D. Thesis, Nanjing Agricultural University, Nanjing, China, 2017.
8. Yang, Y.; Tong, J.; Ma, Y.; Jiang, X.; Li, J. Design and experiment of biomimetic rotary tillage blade based on multiple claws characteristics of mole rats. *Trans. Chin. Society Agric. Eng.* **2019**, *35*, 37–45, (In Chinese with English abstract).
9. Yu, J. Bionic Design of Rotary Blade Based on Rabbot's Claw-Toe Structural Characteristics. Master's Thesis, Central South University of Forestry & Technology, Changsha, China, 2019.
10. Qi, H. The Copying Rotary Tillage Blade Optimization Design and Experimental Research. Master's Thesis, Anhui Agricultural University, Hefei, China, 2017.
11. Sun, Z.; Duan, J.; Yang, Z. Research progress of drag reduction and consumption reduction technology for rotary tillage. *J. Chin. Agric. Mech.* **2021**, *42*, 37–45. (In Chinese) [CrossRef]
12. Liu, J.; Li, Q.; Zheng, X.; Wang, Z. Research Status of Drag Reduction Technology for Soil Tillage Components. *Xinjiang Agric. Mech.* **2021**, *210*, 25–28,37. (In Chinese) [CrossRef]
13. Ma, X. Self-excited Vibration Subsoiler Design and Experimental Research. Ph.D. Thesis, Shenyang Agricultural University, Shenyang, China, 2016.
14. Zhuang, K.; Guo, Z. Research for Application of Vibration Drag Reduction Technology to the Design of Soil Tillage Equipment. *J. Agric. Mech. Res.* **2014**, *36*, 212–217. (In Chinese) [CrossRef]
15. Shahgoli, G.; Saunders, C.; Desbiolles, J.; Fielke, J. An investigation into the performance of vibratory tillage using straight and bent leg tines. *Adv. Geoecol.* **2006**, *38*, 21–30.
16. Wang, X. Study on Vibration Subsoiling Technology and Its Key Parts. Master's Thesis, China Agricultural University, Beijing, China, 2005.
17. Yuan, J.; Wang, J. Research status of self-excited vibration subsoiler. *J. Chin. Agric. Mech.* **2018**, *39*, 11–15. (In Chinese) [CrossRef]
18. Qiu, L.; Li, B. Experimental Study on the Self-Excited Vibration Subsoiler for Reducing Draft Force. *Trans. Chin. Society Agric. Eng.* **2000**, *6*, 72–76. (In Chinese)
19. Li, L.; Li, Y.; Meng, H.; Kan, Z.; Qi, J.; Liu, Q.; Deng, Y. Experimental Study on Performance of Potato Vibration Excavation Device. *J. Agric. Mech. Res.* **2020**, *42*, 173–178. (In Chinese)
20. Shen, D.; Kong, H.; Yao, Z.; Zheng, M.; Fang, J.; Zhang, Y. Design and Experiment of Potato Hiller Based on the Principle of Self-excited Vibration and Drag Reduction. *J. Agric. Mech. Res.* **2022**, *44*, 163–168. (In Chinese) [CrossRef]
21. Askari, M.; Shahgholi, G.; Abbaspour-Gilandeh, Y. New wings on the interaction between conventional subsoiler and paraplow tines with the soil: Effects on the draft and the properties of soil. *Arch. Agron. Soil Sci.* **2018**, *65*, 88–100. [CrossRef]

22. Ma, X.; Wang, S.; Wang, H. Vibration Soil Crushing Mechanism of Self-excited Vibration Subsoiler in Coastal Area. *J. Coast. Res.* **2020**, *103*, 426. [CrossRef]
23. Razzaghi, E.; Sohrabi, Y. Vibratory soil cutting a new approach for the mathematical analysis. *Soil Tillage Res.* **2016**, *159*, 33–40. [CrossRef]
24. Ahmadi, I. A torque calculator for rotary tiller using the laws of classical mechanics. *Soil Tillage Res.* **2017**, *165*, 137–143. [CrossRef]
25. Zhang, X. Research on Vibration Cutting of Wall Groove. Master's Thesis, Hebei University of Technology, Tianjin, China, 2017.
26. Fang, J.; Chen, J.; Niu, P.; Wang, Z.; Luo, Z.; Zheng, Y.; Wang, Y. Simulation and Experimental Study on Vibration Characteristics of Mini Tiller. *J. Agric. Mech. Res.* **2020**, *42*, 203–207. (In Chinese) [CrossRef]
27. Wang, Y. Study on the Establishment of Vibration Model and Structural Optimization of Electric Micro Cultivator. Master's Thesis, Southwest University, Chongqing, China, 2019.
28. Hu, C. Structural Optimization Design and Vibration Analysis of Electric Mini-tiller. Master's Thesis, Southwest University, Chongqing, China, 2018.
29. Zhao, H.; Huang, Y.; Liu, Z.; Liu, W.; Zheng, Z. Applications of Discrete Element Method in the Research of Agricultural Machinery: A Review. *Agriculture* **2021**, *11*, 425. [CrossRef]
30. Zhang, L.; Zhai, Y.; Chen, J.; Zhang, Z.; Huang, S. Optimization design and performance study of a subsoiler underlying the tea garden subsoiling mechanism based on bionics and EDEM. *Soil Tillage Res.* **2022**, *220*, 105375. [CrossRef]
31. Shi, L.; Zhao, W.; Hua, C.; Rao, G.; Guo, J.; Wang, Z. Study on the Intercropping Mechanism and Seeding Improvement of the Cavity Planter with Vertical Insertion Using DEM-MBD Coupling Method. *Agriculture* **2022**, *12*, 1567. [CrossRef]
32. Li, Y.; Hu, Z.; Gu, F.; Wang, B.; Fan, J.; Yang, H.; Wu, F. DEM-MBD Coupling Simulation and Analysis of the Working Process of Soil and Tuber Separation of a Potato Combine Harvester. *Agronomy* **2022**, *12*, 1734. [CrossRef]
33. Zhang, Q. Design and Experimental Study of Self-Excited Vibration Device of Rotary Tillage Tool. Master's Thesis, South China Agricultural University, Guangzhou, China, 2018.

agriculture

Article

Field Grading of Longan SSC via Vis-NIR and Improved BP Neural Network

Jun Li [1,2,3], Meiqi Zhang [1], Kaixuan Wu [1], Hengxu Chen [1], Zhe Ma [1], Juan Xia [1] and Guangwen Huang [1,*]

[1] College of Engineering, South China Agricultural University, Guangzhou 510642, China; autojunli@scau.edu.cn (J.L.); meiqizhang@stu.scau.edu.cn (M.Z.); wukaixuan19990822@163.com (K.W.); hengxuchen@stu.scau.edu.cn (H.C.); m1521829551@163.com (Z.M.); 20221168013@stu.scau.edu.cn (J.X.)

[2] Guangdong Laboratory for Lingnan Modern Agriculture, Guangzhou 510642, China

[3] State Key Laboratory of Agricultural Equipment Technology, Beijing 100083, China

* Correspondence: huanggw@scau.edu.cn; Tel.: +86-158-8996-1680

Abstract: Soluble solids content (SSC) measurements are crucial for managing longan production and post-harvest handling. However, most traditional SSC detection methods are destructive, cumbersome, and unsuitable for field applications. This study proposes a novel field detection model (Brix-back propagation neural network, Brix-BPNN), designed for longan SSC grading based on an improved BP neural network. Initially, nine preprocessing methods were combined with six classification algorithms to develop the longan SSC grading prediction model. Among these, the model preprocessed with Savitzky–Golay smoothing and the first derivative (SG-D1) demonstrated a 7.02% improvement in accuracy compared to the original spectral model. Subsequently, the BP network structure was refined, and the competitive adaptive reweighted sampling (CARS) algorithm was employed for feature wavelength extraction. The results show that the improved Brix-BPNN model, integrated with the CARS, achieves the highest prediction performance, with a 2.84% increase in classification accuracy relative to the original BPNN model. Additionally, the number of wavelengths is reduced by 92% compared to the full spectrum, making this model both lightweight and efficient for rapid field detection. Furthermore, a portable detection device based on visible-near-infrared (Vis-NIR) spectroscopy was developed for longan SSC grading, achieving a prediction accuracy of 83.33% and enabling fast, nondestructive testing in field conditions.

Keywords: nondestructive testing; longan; soluble solids content; visible-near-infrared spectroscopy; brix-back propagation neural network

check for updates

Citation: Li, J.; Zhang, M.; Wu, K.; Chen, H.; Ma, Z.; Xia, J.; Huang, G. Field Grading of Longan SSC via Vis-NIR and Improved BP Neural Network. *Agriculture* **2024**, *14*, 2297. https://doi.org/10.3390/agriculture14122297

Academic Editor: Francesco Marinello

Received: 16 November 2024
Revised: 5 December 2024
Accepted: 12 December 2024
Published: 14 December 2024

1. Introduction

Longan, a specialty fruit native to tropical and subtropical regions, is rich in nutrients and valued for its nourishing and tonic properties [1]. Its fresh fruit, dry fruit, and canned sugar water are globally traded, contributing significantly to economic value [2]. Measuring the soluble solids content (SSC) is essential for evaluating fruit maturity, guiding postharvest treatments, and determining the optimal harvest time [3]. Conventional SSC detection relies primarily on digital refractometers, which suffer from drawbacks such as destructive sampling, tedious operation, and low efficiency [4]. Consequently, there is an urgent need for innovative methods that enable rapid, accurate, and nondestructive SSC evaluation. With the development of spectral detection technology, nondestructive methods based on spectroscopy have been extensively applied to assess the quality of fruits such as pears, apples, and others [5–8]. However, the bulky design and high costs of most spectral detection equipment hinder their practical application in the fields. Therefore, there is an urgent need to develop efficient nondestructive testing methods and portable equipment for fruit quality. In recent years, researchers have designed and utilized portable spectral detection devices to measure the SSC in fruits such as apples and balsam pears [9–11].

However, studies on field detection algorithms and portable detection devices specifically for longan fruits are still scarce.

Meanwhile, deep learning technology is advancing rapidly and shows significant potential in the field of spectral detection [12,13]. With their superior feature extraction and pattern recognition capabilities, deep learning algorithms have achieved remarkable success in predicting the SSC of various fruits. For example, Qiao et al. [14] effectively predicted the SSC and firmness index (FI) of blueberries using hyperspectral imaging combined with the MS-SPA-BPNN model. Zheng et al. [15] developed an apple SSC prediction model using 1D-CNN and PLSR models, demonstrating that the 1D-CNN model can simplify the Vis-NIR spectral modeling process. Qi et al. [8] utilized Vis-NIR and MLP-CNN-TCN deep learning models to achieve fast and nondestructive SSC prediction for crown pear. However, the unique characteristics of longan fruits (such as their hard shell, large seed, and low flesh content) pose significant challenges. These factors impair spectral signal transmittance, increasing the complexity of spectral detection and introducing substantial interference. Consequently, the accuracy and stability of traditional deep learning algorithms for SSC prediction in longan are considerably reduced. Moreover, no specifically SSC prediction model for longan has been developed so far. Therefore, developing an SSC prediction model for longan has become imperative to fulfill the need for the rapid, nondestructive testing of longan fruit ripeness in the field. Such a model would also offer a scientific foundation and decision-making support for mid-production management and postharvest handling.

This study aims to tackle the challenges associated with SSC detection in longan fruits by proposing a qualitative analytical model, the Brix-back propagation neural network (Brix-BPNN), based on an improved BP neural network for rapid and nondestructive SSC detection. The effectiveness and applicability of Brix-BPNN in longan SSC detection were validated through experimental comparisons. Additionally, a portable detection device suitable for field environments was designed and tested. This research offers an effective solution for the quality assessment of longan fruits.

2. Materials and Methods

2.1. Test Samples

The experimental samples were "Chuliang" longans collected from the Longan Garden of the Fruit Tree Research Institute of Guangdong Academy of Agricultural Sciences, Guangzhou, China. A total of 350 Chuliang longans of similar shape and size were selected by a random sampling method. The samples were returned to the laboratory within 1 h after picking, and spectral data collection and soluble solids content determination experiments were carried out at room temperature. Before collecting the spectra, impurities on the sample surface were removed, and samples with damage or defects were excluded, resulting in 325 test samples.

In this study, the SSC (denoted as S) of 325 longan fruits was graded according to the quality grading standard for fresh longan [16]. According to the standard, $S \geq 21.0\%$ is classified as a super-grade, first-grade, or second-grade fruit; $21.0\% > S \geq 19.0\%$ is classified as a third-grade fruit; and $S < 19.0\%$ is classified as an equal external fruit. The specific grade classification is shown in Table 1. These three levels are denoted as 0, 1, and 2 in the classification model.

Table 1. Classification of Chuliang longan.

SSC %	≥21.0	21.0~19.0	<19.0
Grade	Super-grade, first-grade, second-grade fruit	Third-grade fruit	Equal external fruit
Grade labels	0	1	2

2.2. Portable Detection Device

To achieve rapid field detection of longan SSC and meet the need for real-time fruit quality assessment during the harvest season, ensuring optimal harvesting timing, optimizing management, and increasing value, this study designed a portable detection device based on a fiber optic spectrometer. By collecting spectral information from the longan and utilizing a classification prediction model embedded in the instrument, the device enables nondestructive, on-site detection of longan SSC grades.

Figure 1 shows a block diagram of the hardware system structure of the portable detection device. The spectrometer used in this paper is a SPEC-CMS960 fiber optic spectrometer (Pynect, Shenzhen, China) with a wavelength range of 190.357–1100.1 nm and an optical resolution of approximately 2.6 nm. The Youyeetoo X1 SBC x86 control board (SmartFLY Tech. Corp., Shenzhen, China) was selected. The light source used was an LS-H100-type adjustable halogen tungsten light (Pynect, Shenzhen, China) source with a power of 100 W and an effective wavelength range of 380–2500 nm. An RP-N600-7D-1M-ST reflective Y-type fiber probe (Pynect, Shenzhen, China) was used, and the wavelength range was 300–2600 nm.

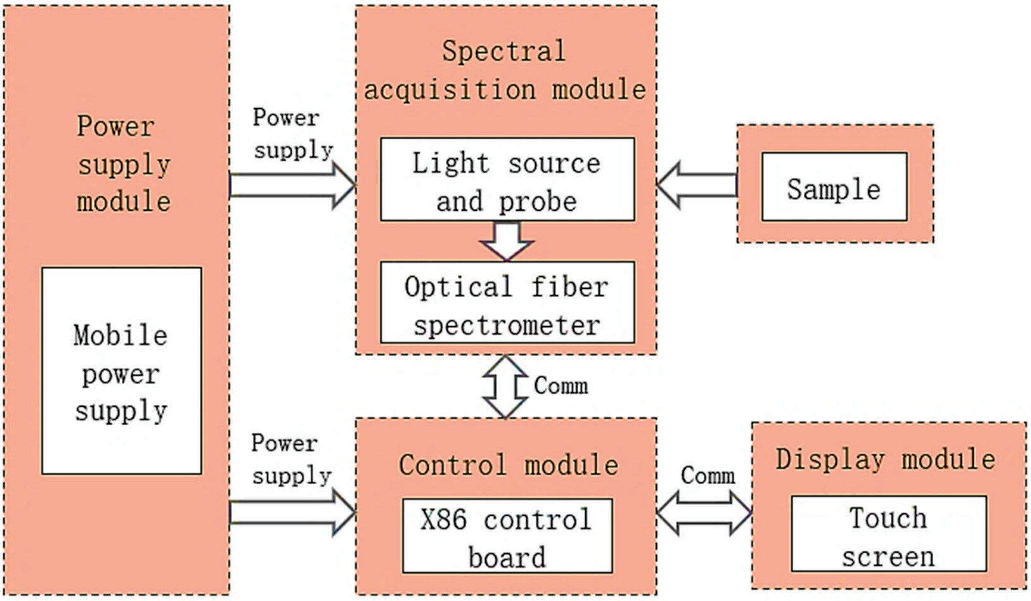

Figure 1. Block diagram of the hardware system structure.

The portable detection device is shown in Figures 2 and 3. The overall size is 320 mm × 220 mm × 240 mm. A black rubber material hood was designed at the probe to avoid interference from natural light when collecting spectra. When the portable detection device works, Longan's spectral reflectance information is obtained through the acquisition module, and the spectral signal is converted into a digital signal and transmitted to the control module for data processing and calculation. The detection results are displayed through the display module, and finally, the spectral data and detection results are saved.

2.3. Modeling Method

2.3.1. Spectral Data Acquisition

The spectral equipment was preheated and whiteboard corrected before spectrum acquisition. The experimental parameters were set to an integration time of 10 ms, averaging number of 10, and smoothing number of 5. The spectrum acquisition range was 190.357–1100.1 nm, and there were 1365 bands in the spectral range. The spectral collection point (Figure 4) is the equatorial part of each sample, collected every 90°, and four spectra are collected for each sample. When the spectrum is collected, the reflection probe is closely attached to the surface of the longan sample to be measured, and the light source is transmitted to the probe through the optical fiber to illuminate the sample. The probe receives the diffuse light signal from the sample, transmits it through the optical fiber to the spectrometer, and then saves the data.

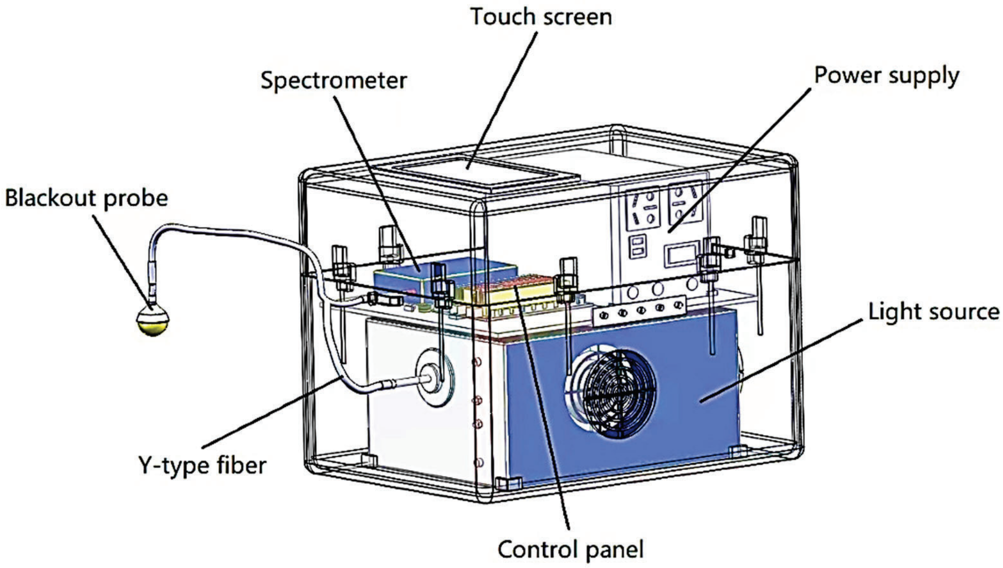

Figure 2. Perspective view of the device.

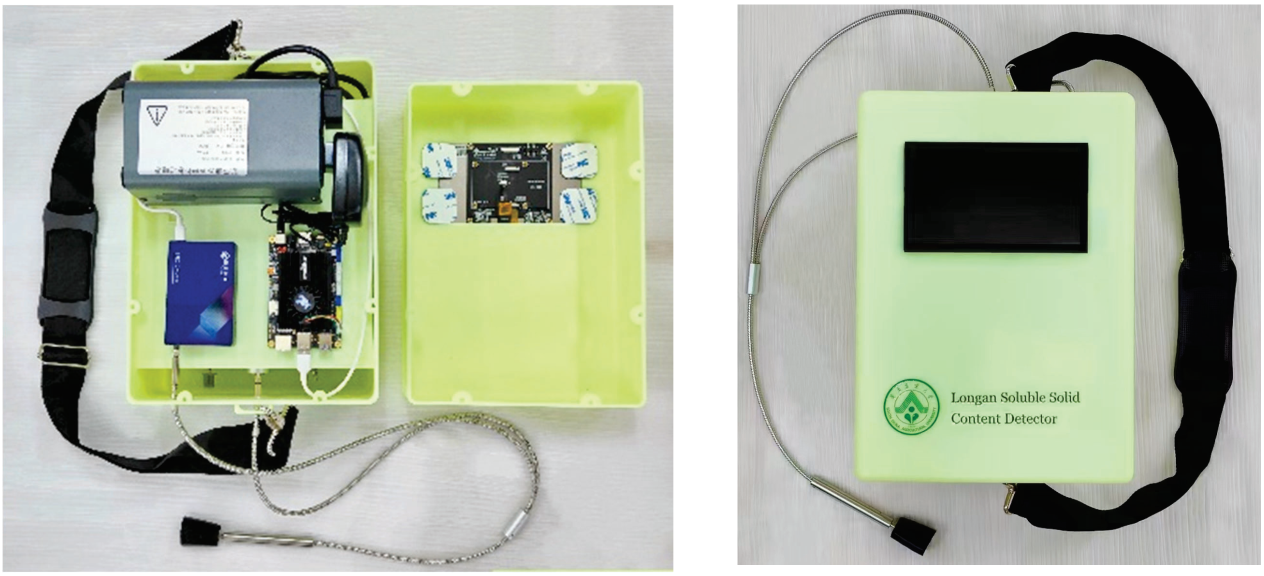

(**a**) (**b**)

Figure 3. Physical drawing of the device: (**a**) internal structure of the device; (**b**) overall view of the device.

2.3.2. Determination of Longan SSC Values

The SSC of longan varies with storage time and environment. Therefore, SSC measurements should be performed immediately after spectral acquisition to obtain more accurate data. The SSC was determined using an ATAGO PAL-BX/ACID3 sugar acidity meter (ATAGO Tech. Corp., Tokyo, Japan); the measurement range was 0–60%, and the measurement accuracy was 0.2%. The longan was peeled and squeezed, and the juice was dropped into the measurement area of the sugar acidity meter for reading. The measurements were repeated three times for each longan sample, and the average value was taken as the real measurement value of the SSC.

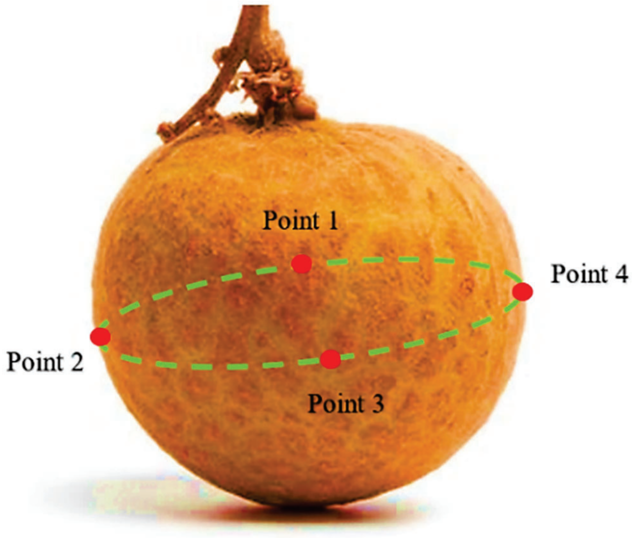

Figure 4. Spectral collection points.

In this study, the longan dataset was divided into a training set and a test set without a separate validation set. This approach was adopted to ensure that the training set contained sufficient data to support effective neural network training. Given the relatively small size of the longan dataset, further splitting it to create a validation set could result in an excessively small training set, potentially compromising the model's learning capacity and overall performance [17]. Table 2 shows the statistical results for the SSC of longan. In this experiment, the SSC range of the training set samples is 14.67% to 24.00%, and the SSC range of the test set samples is 15.95% to 23.65%. The SSC range of the training set samples encompasses the range of the test set samples, so the SSC prediction model established by the training set can be applied to the test set samples.

Table 2. Statistical results of soluble solids content in longan.

Sample Set	Number of Samples	SSC %		
		Range	Average Value	Standard Deviation
Training set	244	14.67~24.00	20.71	1.68
Test set	81	16.15~23.60	20.72	1.61

2.3.3. Spectral Data Preprocessing Method

The original spectral data includes both the sample's characteristic information and extraneous information like instrument noise, baseline drift, and stray light [18]. Therefore, preprocessing is a crucial step to ensure the accuracy and reliability of the model. This study considers that different spectral preprocessing techniques address various issues in spectral data (such as denoising, smoothing, baseline correction, etc.), which, ultimately, have different impacts on model performance. In this study, several common and effective preprocessing methods are used, including multiplicative scatter correction (MSC), standard normal variate (SNV), first derivative (D1), mean centering (CT), Savitzky–Golay smoothing (SG), and their combinations, to preprocess the spectral data. By comparing multiple methods, we aim to gain a more comprehensive understanding of the data characteristics and optimize model performance.

2.3.4. Feature Wavelength Selection Method

The original spectral data have a large amount of data and contain considerable redundancy, noise, and other invalid information. By effectively extracting the characteristic wavelengths associated with SSC, the dimensionality of the data can be significantly reduced and the invalid information can be reduced, thus reducing the computational complexity and improving the efficiency of SSC detection in longan in the field. The successive projection algorithm (SPA) [19] confers the advantages of strong robustness, fast convergence speed, and parallelization in feature wavelength extraction. The competitive adaptive reweighted sampling algorithm (CARS) [20] is outstanding for mining the relationships between features and adaptive weight adjustment. Therefore, the SPA and CARS algorithms were utilized for feature wavelength selection, and a small number of selected feature wavelengths with low collinearity and reduced redundancy, and that contain the most effective information, are used as the input variables of the prediction model to improve the prediction ability and stability.

2.3.5. Classification Models

Due to the high-dimensional, complex, and nonlinear nature of spectral data, selecting the appropriate classification algorithm is crucial. To establish the optimal model for longan SSC classification, this study fully considers the data characteristics and task requirements of longan SSC grading, as well as the advantages of various common traditional machine learning methods and deep learning techniques. Six classification algorithms were selected, including support vector machine (SVM), K-nearest neighbors (KNN), logistic regression (LR), random forest (RF), backs propagation neural network (BPNN), and convolutional neural network (CNN). Through a comprehensive comparison of these methods, the goal was to determine the most effective classification model for achieving more accurate and efficient longan SSC classification. The results indicate that the BPNN model achieved the best classification performance. Therefore, in order to further improve the accuracy and efficiency of longan SSC detection, this study innovatively proposes an improved Brix-BPNN model based on the BP neural network, specifically designed for the precise prediction of longan SSC grades.

2.3.6. Proposed Brix-BPNN Model

The Brix-BPNN model is mainly composed of a Brix module, an activation function module, and a pooling module. The Brix module includes a normalization module, an attention mechanism module, and a convolution module, etc. The overall network structures of the BPNN model and the improved Brix-BPNN model are shown in Figure 5.

Typically, the spectral data of longan exhibit two-dimensional characteristic wavelengths, with overall spectral features that are irregular, inconspicuous, and widely distributed. This situation easily leads to multiple sets of spectra with similar feature wavelengths, relatively flat feature wavelengths, and overlapping phenomena. Therefore, in this paper, 78 two-dimensional feature wavelength tensors X are selected by the CARS algorithm, and a dimension is added as the number of channels, C, so that the data can be better input into the Brix-BPNN convolutional neural network for feature processing. Second, the feature mapping characteristics of the fully connected layer-A module were used to linearly extract and convert the 3D feature wavelength to map the subsequent module for spectral feature extraction. The extracted 3D spectral feature wavelengths were input into the batch normalization module in the Brix module. The batch normalization module standardizing and regularizing each mini batch during the training process helps to reduce the risk of model overfitting and improve the generalization ability of the model. At the same time, reducing the internal covariate shift helps to reduce the problems of gradient disappearance or gradient explosion, thus accelerating the convergence of the Brix-BPNN model.

To improve the correlation and expression ability between the longan SSC and spectral features, and to reduce the negative impact of redundant information and noise on the BP neural network to help the model focus on the most distinctive and important features in the input, the ECA-Brix Attention mechanism module was introduced within the Brix module. The ECA-Brix attention mechanism incorporates a φ module that spreads the spectral features into a single vector, and an ω module that changes the height and width of the spectral features to one. Specifically, the φ module spreads the features in each sample to generate a spectral tensor φ of shape (batch_size,1, height × width × channels), making subsequent processing (e.g., passing into the fully connected layer) easier. The ω module keeps the channels of each sample unchanged while changing them to 1 in height and width, thus generating a spectral tensor ω of shape (batch_size,channels,1), making it easy to compute with tensors of other shapes. The specific structure of the ECA-Brix attention mechanism is shown in Figure 6. By introducing the improved ECA-Brix attention mechanism, the input spectral value tensors can be rearranged and combined. It adaptively learns the importance and weight of each channel and better captures the dependencies between different feature channels, making the model devote more attention to the feature channels related to the longan SSC prediction task. Thus, the correlation and expression ability between the longan SSC and spectral features are improved, and the accuracy and robustness of the model in the prediction of SSC grade are improved. At the same time, compared with a conventional attention mechanism (such as the squeeze-and-excitation module used in SENet), the ECA-Brix attention mechanism adopts a one-dimensional convolution operation, which can calculate channel attention without introducing excessive additional parameters, reducing the computational complexity and storage requirements of the model. This approach is conducive to the development and application of portable devices.

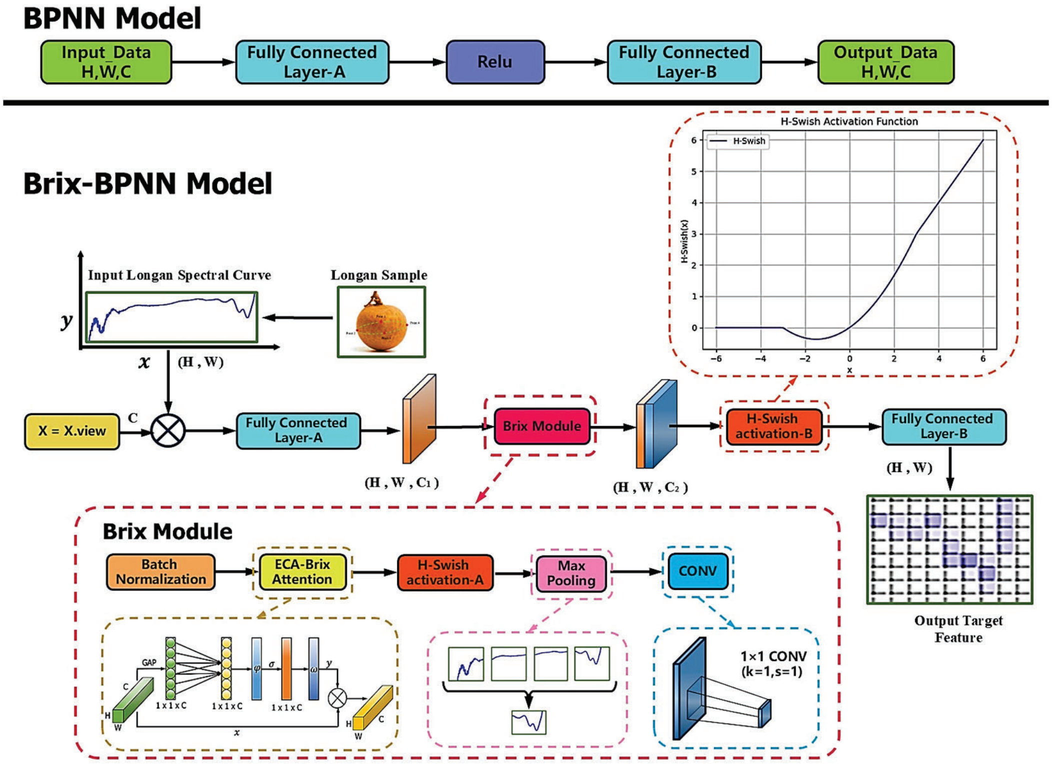

Figure 5. Overall structures of the BPNN and Brix-BPNN.

At the same time, to improve the ability of the Brix-BPNN neural network model to learn the complex nonlinear mapping relationship between the longan SSC and spectral values, the H-swish activation function A is connected after the ECA-Brix attention mechanism module. This activation function only requires simple addition, subtraction, and multiplication operations, and has low computational cost. It is more suitable for processing high-dimensional spectral data and has a non-zero gradient in the negative region, which can effectively alleviate the problem of gradient disappearance and improve the training stability of the model in the deep network. At the same time, the H-swish activation function introduces nonlinear transformation, so that the model can better adapt to the data distribution of various complex spectra when activating the output and improve the accuracy and robustness of the model prediction.

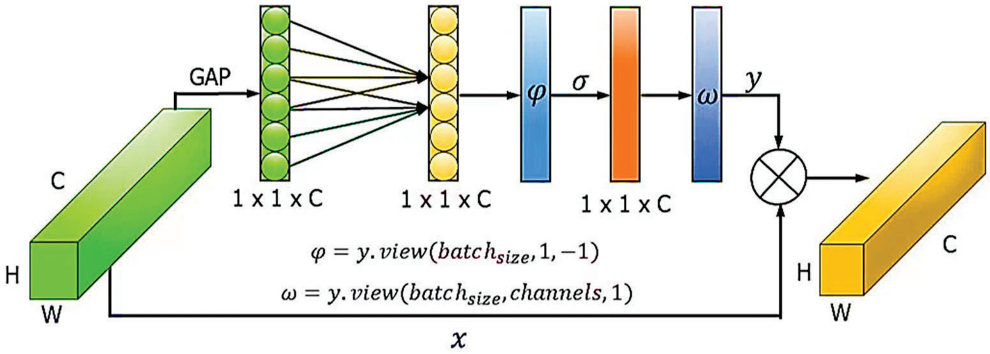

Figure 6. Structural diagram of the ECA-Brix attention mechanism.

The principal formula of the H-swish activation function is shown in Equation (1). Compared with the ReLU activation function in the BPNN model, H-swish not only has the advantages of relatively simple calculations and high computational efficiency but also has a smoother curve (Figure 7), which can help the model better handle spectral data in the spectral data list. In addition, the performance of the model is improved.

$$\begin{aligned} \text{HardSwish}(x) &= x \times \text{HardSigmiod}(x) \\ &= x \times \frac{\text{ReLu6}(x+3)}{6} \\ &= x \times \begin{cases} 1, & x \geq 3 \\ \frac{x}{6} + \frac{1}{2}, & -3 < x < 3 \\ 0, & x \leq -3 \end{cases} \end{aligned} \tag{1}$$

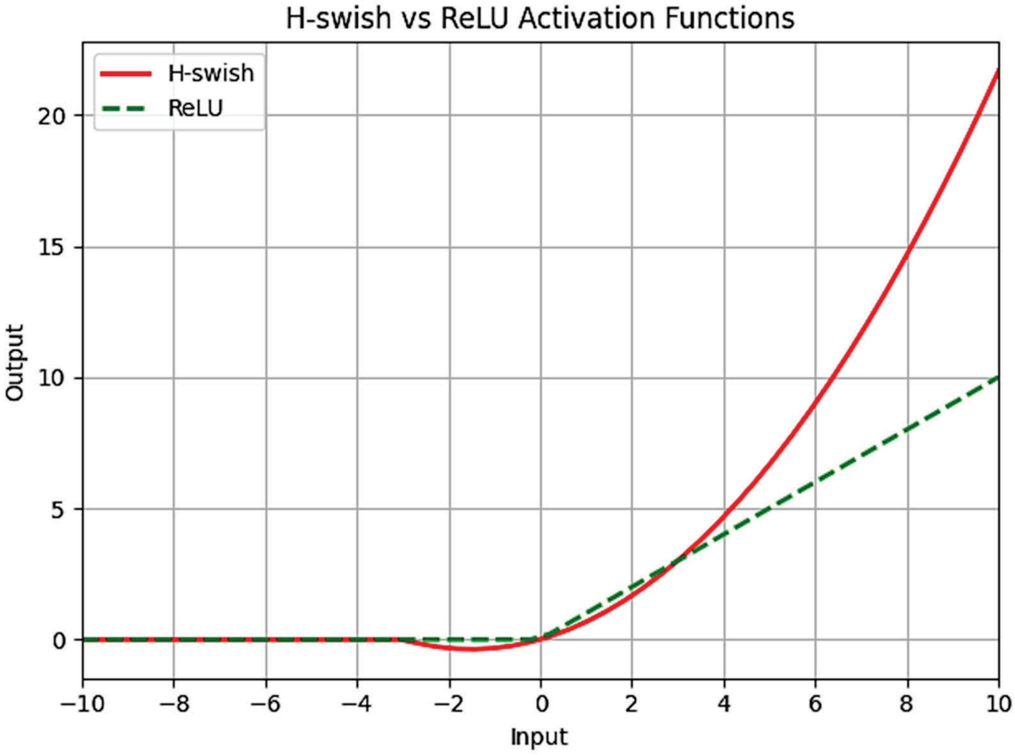

Figure 7. H-swish and ReLU activation functions.

Moreover, to fully utilize the limited resources and arithmetic power of the portable detection device, as well as to help the model extract the most significant features in the region of the spectral feature list, the max-pooling module and the convolutional layer module are introduced in the second half of the Brix module. The max-pooling module effectively extracts key features from spectral data by selecting the maximum values within local regions while reducing the computational burden (as shown in Figure 8), and ensures that the slight translation of the input features within a certain range does not change the position of the maximum value, helping to improve the robustness and generalization ability of the Brix-BPNN model. The role of the convolution module is to perform sliding window calculations on the input spectral data through the convolution kernel to extract local features in the input data. At the same time, by exploiting the "sparse interaction" property of the convolution module, only the local region of the input spectral data is focused, without the full connection with all the input spectral data. This interaction reduces the amount of calculation, improves the computational efficiency, and helps to capture the spatial structure information in the spectral data list.

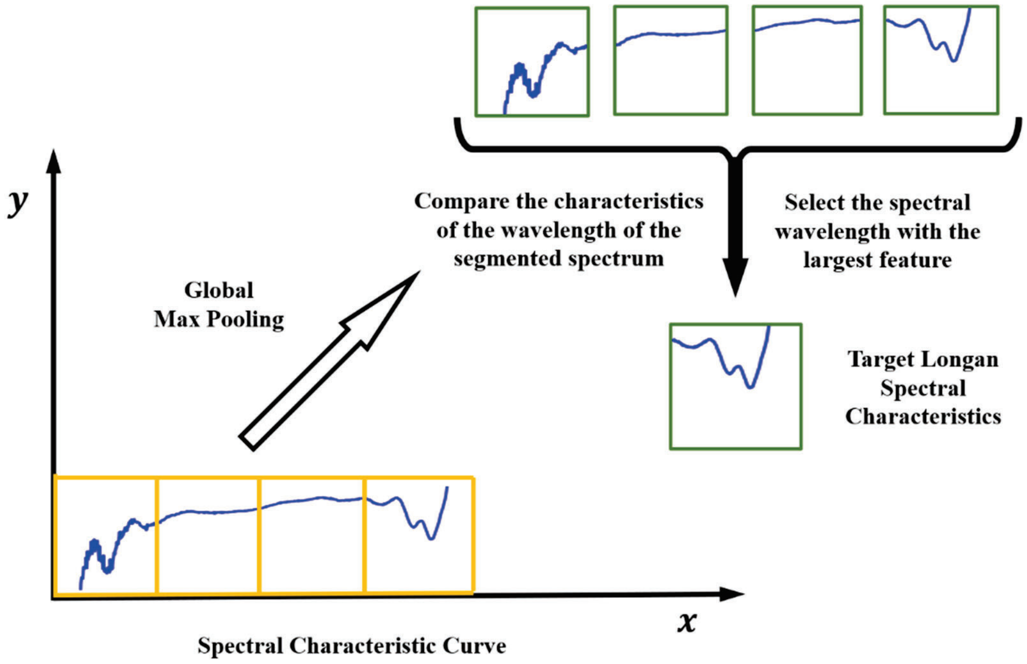

Figure 8. Max pooling process for longan spectral data.

Finally, the H-swish activation function B and the fully connected layer B module were connected after the Brix module. The secondary activation through the H-swish activation function can further enhance the nonlinear characteristics so that the Brix-BPNN model can better fit the complex data distribution output from the Brix module and improve the expression ability and generalization ability of the model. The fully connected layer B module performs further linear transformation of the features, uses the squeeze () function to remove the channel number dimension C of the output tensor X, and restores the spectral data after feature extraction into a two-dimensional tensor.

The improvement of the BP network structure aims to enhance the model's performance in longan SSC classification, with these optimizations primarily focused on more effectively capturing and processing spectral data. Specifically, by introducing the channel dimension and one-dimensional convolution, the model is better able to capture local features of SSC. The ECA module further optimizes channel weights, focusing on key features to reduce noise interference. Additionally, normalization accelerates convergence to ensure stability in the learning process. The H-swish activation function enhances the model's adaptability to diverse data. Finally, pooling layers effectively reduce dimensionality, preserving key features and improving robustness. These optimizations have improved the accuracy, stability, and generalization ability of the Brix-BPNN model.

2.3.7. Model Parameter Setting and Evaluation

To determine the performance of the established model, four main evaluation metrics, namely, accuracy, precision, recall, and harmonic mean F1 score, are used to evaluate the classification model. The traditional machine learning model parameters and deep learning model parameters are summarized in Tables 3 and 4, respectively.

Table 3. Traditional machine learning model parameters.

SVM		KNN	
Parameters	**Parameter Value**	**Parameters**	**Parameter Value**
C	1.0	n_neighbors	5
kernel	'rbf'	weights	'uniform'
gamma	scale	algorithm	'auto'
shrinking	True	p	2
decision_function _shape	'ovr'	metric	'minkowski'
LR		**RF**	
Parameters	**Parameter value**	**Parameters**	**Parameter value**
C	1.0	n_estimators	100
penalty	'l2'	max_depth	10
solver	'lbfgs'	max_features	'auto'
max_iter	100	min_samples_split	2
tol	1×10^{-4}	min_samples_leaf	1

Table 4. Deep learning model parameters.

Parameters	Model		
	CNN	**BPNN**	**Brix-BPNN**
batch_size	2	2	2
epochs	300	300	300
optimizer	SGD	SGD	SGD
learning_rate	0.001	0.001	0.001
loss function	Cross-Entropy	Cross-Entropy	Cross-Entropy

2.4. Field Experiment Method

The designed portable detection device was used to verify the field experiment of longan SSC grade prediction, which was carried out in the Longan Garden of the Fruit Tree Research Institute of Guangdong Academy of Agricultural Sciences, China. The longan garden was divided into 10 regions, and three fruits from one longan tree were randomly selected in each region for detection so that 30 Chuliang longans were detected. The test was repeated three times for each fruit, and the results were recorded to ensure the reliability of the results. After the field test, the fruits were picked and numbered. Within 1 h, the SSC values were measured by a sugar acidity meter, and the grades were recorded to verify the accuracy of the prediction results.

3. Results

The dataset used in this study was sourced from the longan orchard of the Fruit Tree Research Institute, Guangdong Academy of Agricultural Sciences, China, with the "Chuliang" variety of longan selected as the experimental sample. A random sampling method was applied to randomly select 350 longan samples with similar shapes and sizes. After manual screening to remove surface impurities and exclude damaged or defective samples, a final dataset of 325 "Chuliang" longan samples was obtained for model training and evaluation. To ensure fairness, the training and test datasets were kept consistent across all models, with 244 samples designated for training and 81 samples for testing.

All experiments were conducted under the same experimental environment. The experimental setup included a Windows 10 operating system, with Python 3.9, CUDA 11.7, and PyTorch 2.0, and hardware configuration comprising an Intel(R) Core(TM) i5-9300H CPU @ 2.40 GHz and an NVIDIA GeForce GTX 1650 GPU. During model training, the initial learning rate was set to 0.001, and the training period (epochs) was 300.

To validate the effectiveness and fairness of the Brix-BPNN model, we designed a series of horizontal comparative experiments and performed ablation analyses focusing on the model's improvements. Training and validation were conducted under identical hyper-parameter conditions, and these experiments demonstrated the performance advantages of the Brix-BPNN model under the same conditions.

3.1. Sample Spectral Analysis

Due to the significant spectral noise at the beginning (190.357–300.475 nm) and termination (950.248–1100.100 nm) of the spectrum, to maintain the spectral curve with a high signal-to-noise ratio, only the 300.475–950.248 nm band, which included 975 wavelengths, was selected for subsequent analysis. The original spectral curves are shown in Figure 9. It can be seen from the figure that longan spectral curves of different SSC grades have similar trends, and their absorption peak positions are roughly similar. The average spectral curves of longan with three SSC grades are shown in Figure 10. It can be seen from the curves that the differences between different SSC grades are obvious in the ranges of 500–680 nm and 700–880 nm, and the spectral reflectance of longan increases with increasing soluble solid content. Therefore, it is feasible to classify the SSC of longan using spectral data.

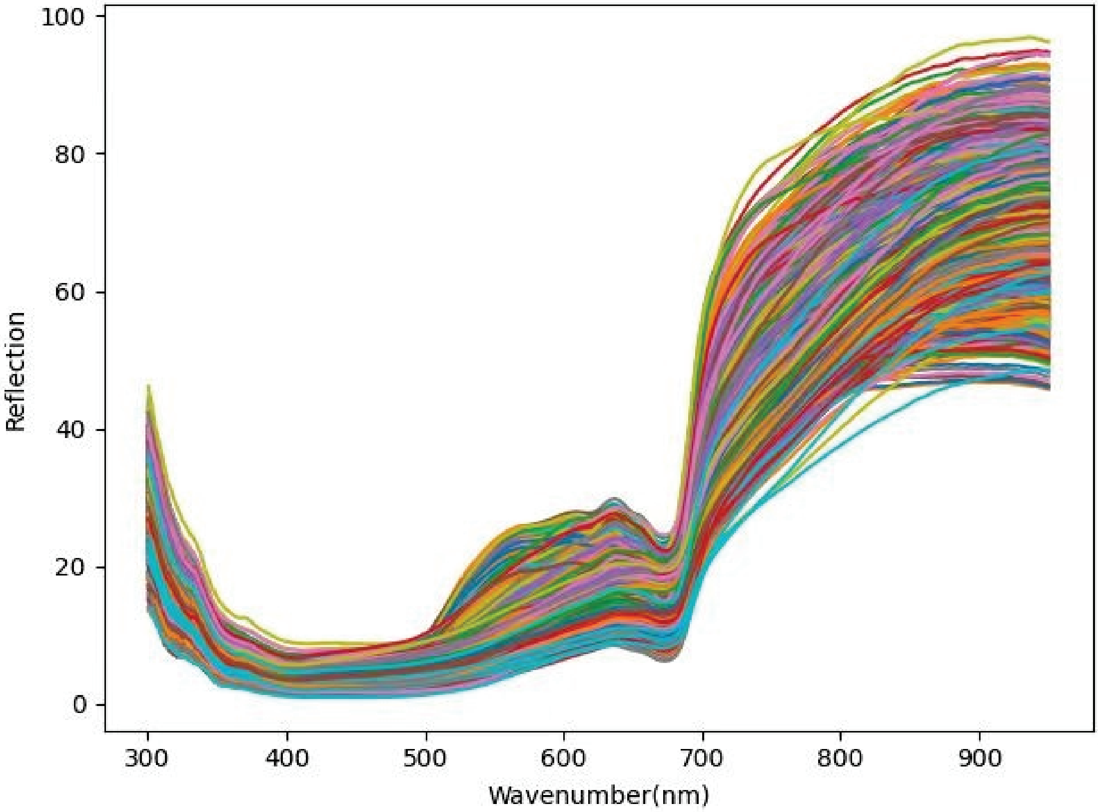

Figure 9. Original spectral curves.

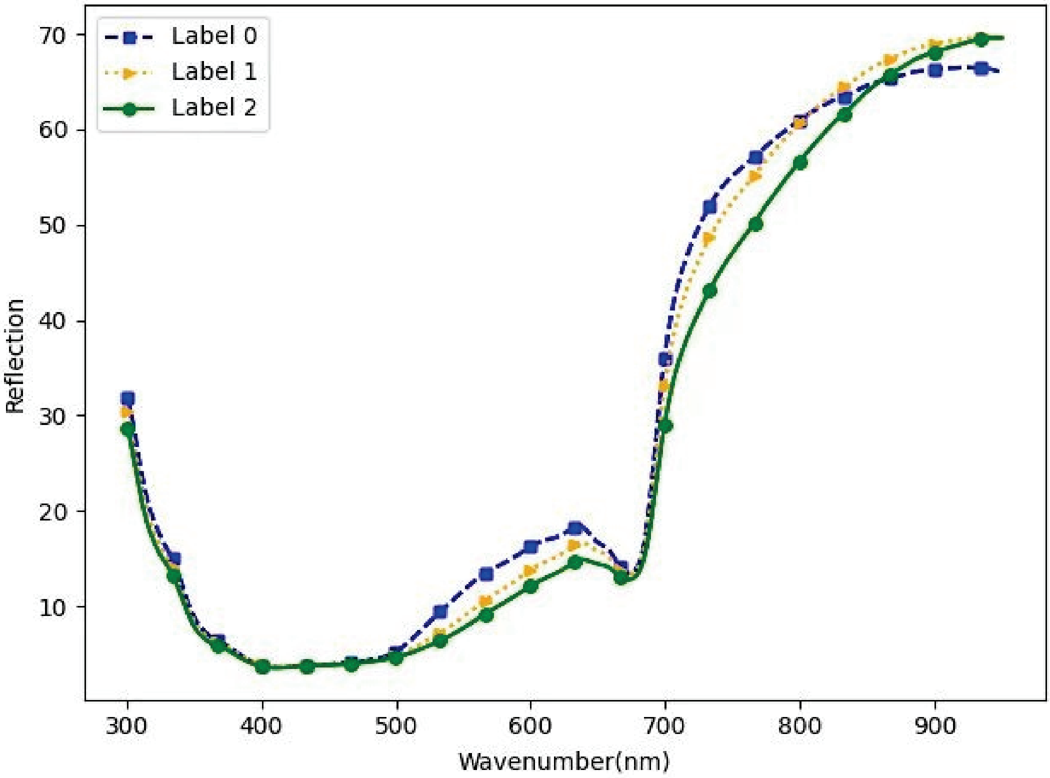

Figure 10. Average spectral curves of the three SSC grades.

3.2. Results of Spectral Data Preprocessing

The original spectral data and the full-band spectral data after different preprocessing were substituted into different models to analyze the effects of the different preprocessing methods on the performances of the different models. The experimental results are shown in Table 5.

Table 5. Modeling results of different spectral preprocessing methods.

Preprocessing	Accuracy%					
	SVM	KNN	LR	RF	BPNN	CNN
Original spectral	54.21	55.90	59.83	60.96	62.08	64.32
SG	54.21	55.90	60.39	61.52	62.36	62.36
SNV	53.09	57.30	64.33	60.39	63.20	60.39
MSC	53.09	57.02	62.36	60.12	60.39	61.24
CT	54.21	59.27	63.48	61.24	63.76	63.76
D1	61.24	56.46	63.76	63.76	67.13	67.13
SG-D1	61.24	60.96	66.29	65.17	69.10	67.41
SG-SNV	53.09	57.58	63.76	60.39	63.48	62.36
SG-MSC	53.09	57.30	63.76	60.96	61.52	62.08
SG-CT	54.21	59.55	63.20	62.92	63.20	65.17

The modeling results show that different preprocessing methods have different modeling effects on different models, and most of them improve the prediction performance of the model. Among the nine preprocessing methods, Savitzky–Golay smoothing combined with the first derivative preprocessing method (SG-D1) has the best effect, and the accuracy of the six classification models established by SG-D1 is higher than that of the other preprocessing methods. Comparing the modeling effects of the six classification models revealed that the accuracies of the BPNN models established by different preprocessing methods are mostly greater than those of the other classification models. Among them, the BPNN model preprocessed by SG-D1 has the best modeling result, and the model classification accuracy reaches 69.10%, which is 7.02% higher than that of the original spectral model. Therefore, in this paper, the SG-D1 preprocessing method was used to preprocess the original spectral data, and the BP neural network was used to establish a longan SSC grading prediction model.

3.3. Characteristic Wavelength Selection

To eliminate a significant amount of redundant, noisy, and invalid information from the original spectral data, reduce model complexity, and enhance detection efficiency to meet the rapid real-time detection needs for longan fruits in the field, SPA and CARS feature extraction algorithms were employed for dimensionality reduction. This is of great value to orchard staff in assessing the maturity of longan in a timely manner and optimizing the timing of picking.

3.3.1. Results of SPA Feature Wavelength Selection

The process of applying the SPA algorithm to the longan spectral data preprocessed by SG-D1 for feature wavelength selection is shown in Figure 11a. The SPA determines the number of feature wavelengths according to the root mean square error (RMSE). Figure 11a shows that with an increase in the number of wavelengths, the RMSE quickly decreases to the lowest point and then tends to flatten after a small fluctuation. When the RMSE reaches the minimum value, the 20 optimal feature wavelengths are identified as [327.584, 341.479, 362.667, 364.654, 367.967, 448.903, 464.85, 479.475, 558.029, 600.706, 674.164, 682.185, 719.636, 728.334, 873.734, 887.152, 898.559, 905.27, 911.31, and 916.68], and the specific distributions are shown in Figure 11b.

3.3.2. Results of CARS Feature Wavelength Selection

The process of applying the CARS algorithm to longan spectral data preprocessed by SG-D1 for feature wavelength selection is shown in Figure 12. The number of Monte Carlo samples is set to 50. Figure 12a shows that the number of selected wavelengths gradually decreases with increasing sampling time. Figure 12b shows that the RMSECV first decreases and then increases with increasing sampling time, and when the number of iterations reaches 20, the RMSECV reaches the minimum value, at which point 78 feature wavelengths are selected.

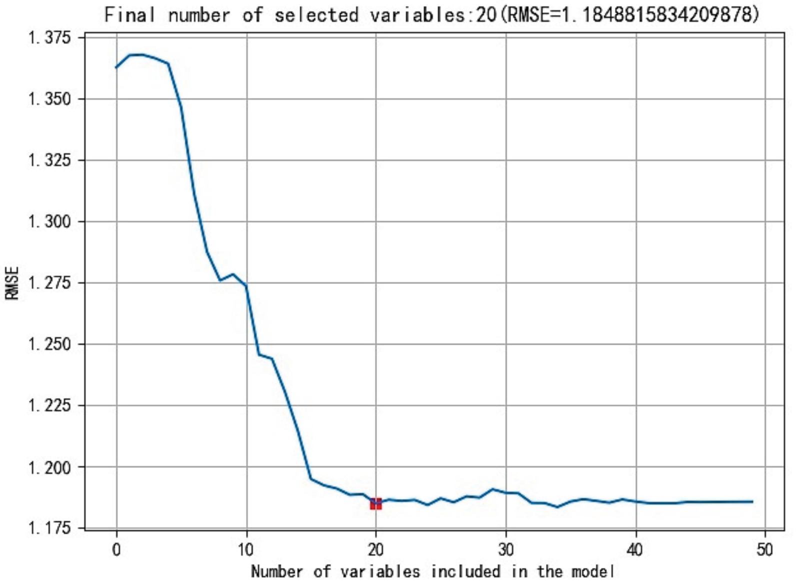

(**a**)

Figure 11. *Cont.*

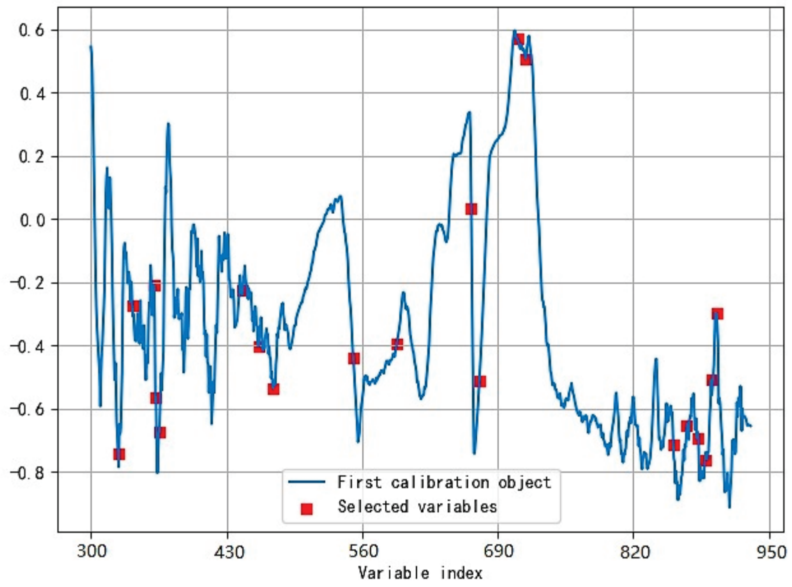

(**b**)

Figure 11. Feature wavelength selection of longan SSC based on the SPA algorithm: (**a**) RMSE variation of the model; (**b**) optimal feature wavelength selected by SPA.

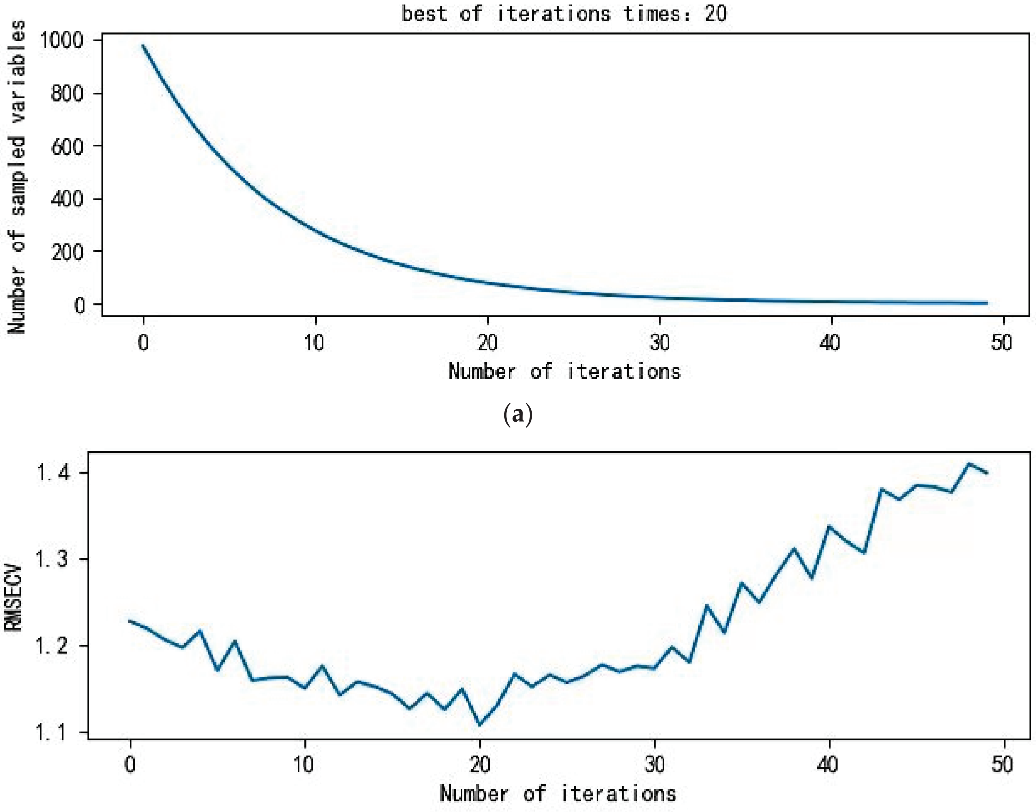

(**a**)

(**b**)

Figure 12. Feature wavelength selection of longan SSC based on the CARS algorithm: (**a**) number of sample variables; (**b**) RMSECV.

3.4. Results of BP Neural Network Modeling

The BPNN classification prediction model for the longan SSC grade is established based on full-band spectral data and the feature wavelengths selected by the SPA and CARS algorithms, and the influence of the number of wavelength variables on the performance of the model is compared and analyzed.

Table 6 shows that the BPNN model established based on the full band has the best prediction effect, with an accuracy of 69.10%. Compared with those of the full band, the numbers of feature wavelengths selected by the SPA and CARS algorithms are reduced by 98% and 92%, respectively, and the model training efficiency is significantly improved, while the modeling accuracy is reduced by only 1.69% and 0.84%, respectively, compared with that of the full band. There is also only a small decrease in the precision, recall, and harmonic mean F1 score. The results show that a large amount of invalid spectral information is eliminated, which significantly improves the operating efficiency and stability of the BPNN model and makes the model more suitable for practical portable detection device applications in the field. Therefore, the BPNN model established based on the feature wavelength has good predictive ability for the nondestructive testing of longan SSC grading.

Table 6. BPNN modeling results for longan SSC grading based on full-band and feature wavelengths.

Variable Selection Method	Wavelength Number	Accuracy%	Precision%	Recall%	F1%
Full band	974	69.10	68.43	67.82	67.20
SPA	20	67.41	63.09	64.41	63.42
CARS	78	68.26	67.07	67.42	66.71

The modeling accuracy of the 78 feature wavelengths selected by the CARS algorithm combined with the BP neural network is 68.26%, which is higher than the 67.41% achieved by the 20 feature wavelengths selected by the SPA algorithm, which indicates that some important features may be lost during SPA feature wavelength selection, thus reducing the prediction performance of the model.

3.5. Results of Brix-BPNN Modeling

The improved Brix-BPNN model was used to establish a qualitative analysis model of longan SSC grade based on the full band and feature wavelengths, and the classification results are shown in Table 5. According to Tables 4 and 5, compared with the BPNN model, the Brix-BPNN model achieves better modeling effects for different wavelength variables, with improved values of the four evaluation indicators and model performance. The modeling accuracies of the full-band, 20-feature-wavelength, and 78-feature-wavelength models are 69.66%, 68.25%, and 71.10%, respectively, which are 0.56%, 0.85%, and 2.84% higher than those of the BPNN model. This indicates that the Brix-BPNN model achieves better predictive performance than the BPNN model in the qualitative analysis of longan SSC grades.

Table 7 shows that the longan SSC classification model established by 78 feature wavelengths selected by the CARS algorithm has the best prediction effect, and the accuracy of the model is 1.44% higher than that of the full-band model and 2.85% higher than that of the 20-feature-wavelength model; the precision, recall rate and harmonic mean F1 score of the proposed model are also greater than those of the full-band model and the 20-feature-wavelength model. This further indicates that feature wavelength selection helps improve the overall prediction performance and stability of the model, while too few feature wavelength variables may eliminate some important features, thereby reducing the prediction performance of the model.

Table 7. Brix-BPNN modeling results for longan SSC grading based on full-band and feature wavelengths.

Variable Selection Method	Wavelength Number	Accuracy%	Precision%	Recall%	F1%
Full band	974	69.66	69.50	68.42	67.40
SPA	20	68.25	66.02	66.85	65.12
CARS	78	71.10	70.04	69.10	68.44

Therefore, combining the feature wavelengths selected by the CARS algorithm with the improved Brix-BPNN neural network model resulted in a classification accuracy of 71.10%, achieving the best prediction performance. The CARS algorithm performed excellently in selecting feature wavelengths from the longan SSC spectral data. Compared to using the full spectrum, it effectively reduced the number of wavelengths by 92% while retaining key information, thereby alleviating the computational burden on the model and shortening the training duration. This improvement enhances the model's training efficiency and prediction speed, which is particularly crucial for deploying the model in field environments and enabling real-time detection.

3.6. Results of Model Ablation and Comparison Experiments

To further validate the superiority of the proposed CARS+Brix-BPNN model, ablation experiments were conducted, and the results are presented in Table 8. Model 1 represents the original structure of the BPNN model based on the full spectrum, while Model 2 represents the original structure of the BPNN model constructed using 78 feature wavelengths extracted by CARS. Model 3 incorporates a Batch Normalization module into the front-end of the CARS+BPNN model, and Model 4 integrates the improved ECA-Brix attention mechanism into the front-end of the CARS+BPNN model. Model 5 replaces the ReLU activation function with the H-Swish activation function in the CARS+BPNN model. Model 6 integrates a Max-Pooling module into the backend of the CARS+BPNN model, and Model 7 incorporates a convolution module into its backend. Model 8 integrates both the Batch Normalization module and the improved ECA-Brix attention mechanism into the front-end of the CARS+BPNN model, while Model 9 builds on Model 8 by replacing the ReLU activation function with the H-Swish activation function. Model 10 extends Model 9 by incorporating a Max-Pooling module. Model 11 integrates the Brix-Module into the middle section of the CARS+BPNN model, and Model 12 represents the proposed CARS+Brix-BPNN model structure in this study.

Table 8. CARS+Brix-BPNN model ablation experiment results.

Number	Model	Accuracy%	Precision%	Recall%	F1%
1	BPNN	69.10	68.43	67.82	67.20
2	CARS+BPNN	68.26	67.07	67.42	66.71
3	CARS+BPNN+BN	69.10	64.47	65.73	64.84
4	CARS+BPNN+ECA-Brix	68.82	68.20	68.82	65.87
5	CARS+BPNN+H-Swish	68.54	65.15	66.01	62.13
6	CARS+BPNN+Max-Pool	68.53	67.13	67.52	66.48
7	CARS+BPNN+CONV	68.82	63.92	65.73	62.72
8	CARS+BPNN +BN+ECA-Brix	69.38	65.95	67.42	65.58
9	CARS+BPNN+BN +ECA-Brix+H-Swish	69.66	68.87	67.85	66.11
10	CARS+BPNN+BN +ECA-Brix+H-Swish+Max-Pool	70.50	68.66	68.82	67.83
11	CARS+BPNN+Brix-Module	70.86	69.47	68.56	67.93
12	CARS+Brix-BPNN	71.10	70.04	69.10	68.44

As shown in Table 8, incorporating the Batch Normalization module, the improved ECA-Brix attention mechanism, the Max-Pooling module, and the convolution module into the CARS+BPNN model, as well as replacing the ReLU activation function with the H-Swish activation function, all contributed to improvements in the model's accuracy, with the highest improvement reaching 0.84%. Furthermore, progressively combining and applying individual modules to the CARS+BPNN model demonstrated that each combination algorithm improved the model's accuracy, precision, recall, and F1 score, exhibiting a cumulative performance effect. Among these, the combination of the CARS+BPNN model with the Brix-Module further enhanced the model's overall performance. Ultimately, compared to the full-spectrum BPNN model, the CARS+Brix-BPNN model reduced the number of wavelengths by 92%, while improving accuracy and precision by 2% and 1.61%, respectively. These findings indicate that the proposed Brix-BPNN model not only achieved improved detection accuracy but also successfully realized model lightweighting, meeting the requirements for both accuracy and efficiency in predictive modeling.

To further validate the efficiency and adaptability of the proposed Brix-BPNN model in classifying and recognizing SSC within complex longan spectral data, comparative experiments were conducted with various machine learning models. The Brix-BPNN model was compared with several BPNN variants, including MLP, Dropout-BPNN, Residual-BPNN, and ResNet-BPNN. Four performance metrics—accuracy, precision, recall, and F1 score—were selected to comprehensively evaluate and analyze the performance of each model. The experimental results are presented in Table 9.

Table 9. Brix-BPNN model comparison experiment results.

Model (CARS+)	Accuracy%	Precision%	Recall%	F1%
BPNN	68.26	67.07	67.42	66.71
MLP	69.38	65.98	66.85	63.67
Dropout-BPNN	68.26	66.76	66.85	64.23
Residual-BPNN	68.82	62.84	63.20	61.96
ResNet-BPNN	68.15	66.12	66.01	61.90
Brix-BPNN	71.10	70.04	69.10	68.44

Based on the results in Table 9, the proposed Brix-BPNN model outperforms other classical models in both detection accuracy and precision. Compared to other models, the Brix-BPNN model achieved an average improvement of 2.53% in accuracy and 4.29% in precision. Considering all performance metrics comprehensively, the Brix-BPNN model demonstrates the best overall performance, showcasing exceptional capabilities in analyzing longan spectral features as well as identifying and classifying SSC. It effectively meets the dual requirements of real-time performance and high accuracy.

3.7. Field Experiment Verification

Embedding the improved optimal Brix-BPNN model into the developed portable detection device, the stability and accuracy of the model were verified according to the field experiment method mentioned in Section 2.4. The SSC grade of 30 Chuliang longan fruits was predicted, and the SSC values were measured with a sugar acidity meter. The true and predicted labels of the longan samples are shown in Figure 13, and a summary of the test results is provided in Table 10.

Among the 30 test samples, 25 were correctly predicted, resulting in an overall classification accuracy of 83.33%, which is generally sufficient for the rapid, nondestructive field detection of longan SSC classification. Among the five misclassified samples (numbers 8, 11, 17, 21, 26), three samples had SSC values of 21.20% (sample 11), 20.75% (sample 17), and 18.80% (sample 26), which are very close to the classification thresholds of 21% and 19%, respectively. This proximity to the critical thresholds may have been the primary cause of misclassification. Furthermore, the misclassification of samples 8 and 21 might have been influenced by field environmental factors such as lighting and humidity, as well as noise or feature interference in the spectral data, which led to the model incorrectly identifying the true classification of these samples. The test results show that this classification model performs well in predicting longan samples. Future research plans include further improving the model algorithm and enhancing data preprocessing, particularly by controlling the surface conditions of the samples and environmental factors, to improve the classification accuracy of longan fruit.

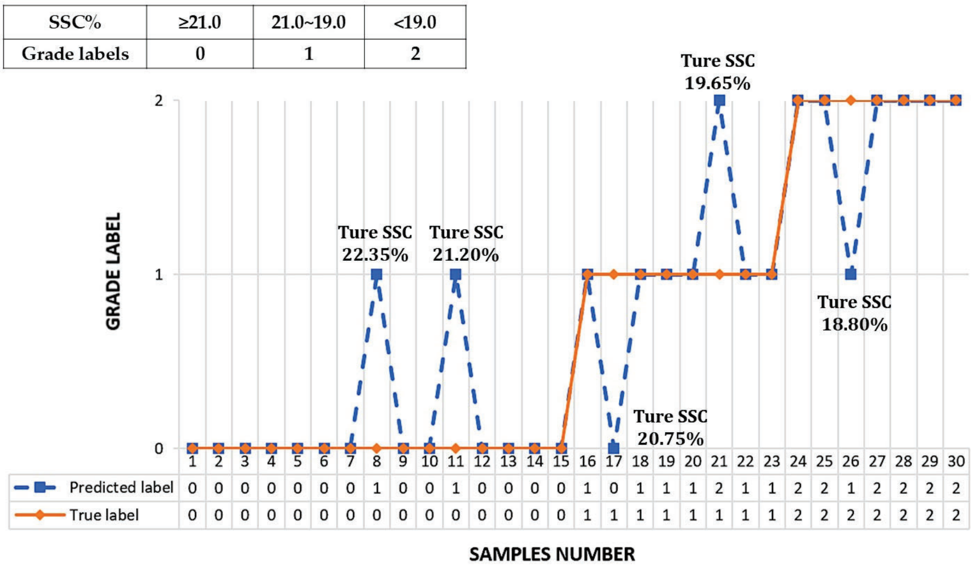

SSC%	≥21.0	21.0~19.0	<19.0
Grade labels	0	1	2

	1	2	3	4	5	6	7	8	9	10	11	12	13	14	15	16	17	18	19	20	21	22	23	24	25	26	27	28	29	30
Predicted label	0	0	0	0	0	0	0	1	0	0	1	0	0	0	0	1	0	1	1	1	2	1	1	2	2	1	2	2	2	2
True label	0	0	0	0	0	0	0	0	0	0	0	0	0	0	0	1	1	1	1	1	1	1	1	2	2	2	2	2	2	2

Figure 13. Statistical chart of the true and predicted labels for the SSC grade of the test samples.

Table 10. Results of field experiments.

SSC Grade	Grade Labels	Number of True Detections	Number of True Predictions	Number of False Predictions	Accuracy%
Super-grade, first-grade, second-grade fruit	0	15	13	2	86.67%
Third-grade fruit	1	8	6	2	75%
Equal external fruit	2	7	6	1	85.71%
Total	Total	30	25	5	83.33%

4. Discussion

Based on the results of the study, the proposed nondestructive detection method based on Vis-NIR spectroscopy, along with the portable device, has shown remarkable performance in the classification of longan SSC. Compared to traditional SSC detection methods such as refractometry and chemical titration, the spectral method offers higher sensitivity and accuracy, and it allows for rapid measurement without the need for sample pretreatment. This greatly improves detection efficiency and convenience. Furthermore, the developed portable device has the advantages of compact structure and ease of operation, enabling real-time field detection and overcoming the limitations of traditional methods that require specialized laboratory settings and complex operating procedures.

The spectral analysis results show that there are distinct differences in the spectral data of longan at different SSC levels within the wavelength ranges of 500–680 nm and 700–880 nm. As the SSC content increases, the reflectance gradually increases, indicating that it is feasible to use spectral data for the classification and detection of longan SSC.

Preprocessing is crucial for enhancing the robustness and reliability of the model, especially in real-time on-site prediction scenarios, as it removes noise and improves the quality of the spectral data [21]. The results of spectral data preprocessing indicate that using the Savitzky–Golay smoothing method combined with the first derivative (SG-D1) effectively reduces noise in the raw spectral data caused by environmental and equipment factors, while enhancing the spectral features related to the longan SSC. Compared to other preprocessing methods, SG-D1 shows significant effectiveness in noise reduction and the enhancement of subtle features, making the final spectral data more stable and of higher quality, which, in turn, improves the predictive performance of the model. Furthermore, the study results suggest that combining different preprocessing methods is more effective than using a single preprocessing method in improving both spectral data quality and model performance, as also demonstrated in other studies [22].

This study employed two feature extraction algorithms, SPA (Successive Projections Algorithm) and CARS (Competitive Adaptive Reweighted Sampling), to select wavelengths most relevant to longan SSC from the spectral data. This process retained key information while effectively reducing the number of spectral variables, thus improving training efficiency, reducing computational load, and speeding up prediction, which is crucial for real-time field detection. The results showed that SPA performed well in dimensionality reduction efficiency, whereas CARS exhibited superior classification accuracy, consistent with the findings of Cheng et al. [23], who also found that CARS retained more classification-relevant information, thereby enhancing the model's predictive capability. However, despite CARS outperforming SPA with smaller datasets in this study, a balance between efficiency and accuracy in real-time applications with larger datasets still requires further investigation.

The Brix-BPNN model proposed in this study significantly improved the accuracy and stability of longan SSC classification compared to the original BPNN model. By incorporating a Brix module, which includes normalization, attention mechanisms, and convolutional modules, the model more effectively captures and enhances key information, significantly improving classification accuracy and stability. However, compared to studies on SSC detection in other fruits, the prediction accuracy in this study was slightly lower. Liu et al. [24] used visible-near-infrared spectroscopy combined with the BPNN model to achieve 90% accuracy in the measurement of navel orange fruit SSC. Chen et al. [25] utilized the BP-PLS method in combination with NIR to achieve the rapid and accurate detection of SSC in PE-packed blueberries ($Rp^2 = 0.947$). Several factors contribute to the accuracy of the model. First, the physical characteristics of different fruits may be a major reason for accuracy differences. Longan fruits have a hard shell and low edible portion, making spectral signal acquisition more challenging. The separation of the peel from the pulp may cause spectral interference, affecting data quality and model accuracy. In contrast, fruits such as navel oranges, which have thin and transparent skins, allow for clearer spectral signals and, therefore, higher SSC prediction accuracy. Second, different detection devices can significantly impact model accuracy. Given the goal of enhancing the portability of the device and reducing costs, the spectral detection equipment chosen for this study may have a lower resolution and signal-to-noise ratio compared to other devices used in previous studies, leading to suboptimal spectral data quality and, in turn, affecting model training and prediction performance.

Therefore, in future research, we will consider optimizing the network structure from several aspects to further improve the model performance. For example, we could try to design a more lightweight network structure to reduce the computational complexity, introducing dynamic weight allocation or a dynamic layer selection mechanism, so that the network can adapt to adjust the structure according to the input data, improving the computational efficiency and performance. Or, we could introduce a residual structure to alleviate the gradient disappearance problem of the deep network, and a design multi-branch structure to process different feature or scale information, and carry out feature fusion in the final stage to improve the adaptability to complex tasks.

Moreover, by combining the developed portable device with an efficient classification model, this study has achieved the rapid, nondestructive field detection of longan SSC. The system design of this study places a greater emphasis on the practical needs of field applications, making the detection system suitable for agricultural production environments.

Unlike many studies that require laboratory-based testing [14,26], this research provides a new technological solution for the rapid field detection of fruit quality, with promising potential for practical applications in agricultural settings.

5. Conclusions

To achieve the rapid field detection of longan SSC and address the need for real-time fruit quality assessment during the harvest period, ensuring optimal harvest timing, this study proposes a detection method based on an improved BP neural network and develops a portable detection device. Spectral data of Chuliang longan within the 190.357–1100.1 nm wavelength range were collected, pretreated, and analyzed to select characteristic wavelengths. A qualitative analysis model for longan SSC was established and improved subsequently. Finally, the accuracy and stability of the model were validated through experimental testing. The following were the main conclusions:

1. The original spectral data collected were preprocessed by nine preprocessing methods (SG, D1, SNV, MSC, CT, SG-D1, SG-SNV, SG-MSC, and SG-CT) and combined with six classification algorithms (SVM, KNN, LR, RF, BPNN, and CNN) to develop an SSC qualitative analysis model for longan. Among these methods, the SG-D1 preprocessing method paired with the BP neural network demonstrated the best prediction performance. The classification accuracy of the full-band model reached 69.10%, which is 7.02% higher than the accuracy of the original spectral model.
2. The SPA and CARS algorithms were applied to extract feature wavelength spectra following data pretreatment. These were then combined with the BPNN model and the improved Brix-BPNN model to establish a qualitative analysis model for longan SSC, utilizing both the full band and the feature wavelength. The experimental results showed that the Brix-BPNN model, based on 78 feature wavelengths extracted via CARS, achieved the best performance, with a classification accuracy of 71.10%, which is 2.84% higher than that of the original BPNN model. The number of wavelengths was reduced by 92% compared to the full band, making this model lightweight and efficient for rapid field detection.
3. The improved optimal Brix-BPNN model was implanted into the developed portable detection device and validated through field experiments. The SSC grade of 30 Chuliang longan samples was predicted, with 25 accurate predictions, resulting in a total classification accuracy of 83.33%. The results demonstrate that the portable detection system can effectively facilitate the rapid, nondestructive detection of longan SSC grading in the field. The portable detection can serve as a decision-making tool for longan production management and postharvest treatment, offering promising application prospects.

Author Contributions: Conceptualization, G.H. and H.C.; methodology, J.L. and M.Z.; software, M.Z. and K.W.; validation, Z.M. and J.X.; formal analysis, H.C.; investigation, Z.M. and J.X.; data curation, M.Z. and K.W.; writing—original draft preparation, J.L. and M.Z.; writing—review and editing, G.H.; supervision, J.L.; project administration, J.L.; funding acquisition, J.L. All authors have read and agreed to the published version of the manuscript.

Funding: This research was funded by the Guangdong Laboratory for Lingnan Modern Agriculture (NZ2021040 and NT2021009), the Special Project of Rural Vitalization Strategy of Guangdong Academy of Agricultural Sciences (TS-1-4), the China Agriculture Research System (CARS-32), the Guangdong Provincial Agricultural Science and Technology Demonstration (2023-440000-60010000-9818), and the Discipline Construction Project of South China Agricultural University in 2023 (2023B10564002).

Institutional Review Board Statement: Not applicable.

Data Availability Statement: Data available on request due to privacy. The data presented in this study are available on request from the corresponding author. The data are not publicly available due to undisclosed intellectual property content and privacy concerns.

Conflicts of Interest: The authors declare no conflicts of interest.

References

1. Huang, S.; Lv, X.; Han, Y.; Han, D.; Wei, J.; Li, J.; Guo, D. Disrupted sugar transport and continued sugar consumption lead to sugar decline in ripe 'Shixia'longan fruit. *LWT* **2024**, *191*, 115620. [CrossRef]
2. Zeng, S.; Wang, K.; Liu, X.; Hu, Z.; Zhao, L. Potential of longan (*Dimocarpus longan* Lour.) in functional food: A review of molecular mechanism-directing health benefit properties. *Food Chem.* **2023**, *437*, 137812. [CrossRef] [PubMed]
3. Shao, Y.; Ji, S.; Xuan, G.; Wang, K.; Xu, L.; Shao, J. Soluble solids content monitoring and shelf life analysis of winter jujube at different maturity stages by Vis-NIR hyperspectral imaging. *Postharvest Biol. Technol.* **2024**, *210*, 112773. [CrossRef]
4. Guo, W.; Li, W.; Yang, B.; Zhu, Z.; Liu, D.; Zhu, X. A novel noninvasive and cost-effective handheld detector on soluble solids content of fruits. *J. Food Eng.* **2019**, *257*, 1–9. [CrossRef]
5. Tian, X.; Fan, S.; Li, J.; Huang, W.; Chen, L. An optimal zone combination model for on-line nondestructive prediction of soluble solids content of apple based on full-transmittance spectroscopy. *Biosyst. Eng.* **2020**, *197*, 64–75. [CrossRef]
6. Sirisomboon, P.; Tanaka, M.; Kojima, T.; Williams, P. Nondestructive estimation of maturity and textural properties on tomato 'Momotaro'by near infrared spectroscopy. *J. Food Eng.* **2012**, *112*, 218–226. [CrossRef]
7. Yang, X.; Zhu, L.; Huang, X.; Zhang, Q.; Li, S.; Chen, Q.; Wang, Z.; Li, J. Determination of the soluble solids content in korla fragrant pears based on visible and near-infrared spectroscopy combined with model analysis and variable selection. *Front. Plant Sci.* **2022**, *13*, 938162. [CrossRef]
8. Qi, H.; Shen, C.; Chen, G.; Zhang, J.; Chen, F.; Li, H.; Zhang, C. Rapid and nondestructive determination of soluble solid content of crown pear by visible/near-infrared spectroscopy with deep learning regression. *J. Food Compos. Anal.* **2023**, *123*, 105585. [CrossRef]
9. Yuan, W.; Zhou, H.; Zhou, Y.; Zhang, C.; Jiang, X.; Jiang, H. In-field and nondestructive determination of comprehensive maturity index and maturity stages of *Camellia oleifera* fruits using a portable hyperspectral imager. *Spectrochim. Acta Part A* **2024**, *315*, 124266. [CrossRef] [PubMed]
10. Yu, Y.; Zhang, Q.; Huang, J.; Zhu, J.; Liu, J. Nondestructive determination of SSC in Korla fragrant pear using a portable near-infrared spectroscopy system. *Infrared Phys. Technol.* **2021**, *116*, 103785. [CrossRef]
11. Yao, Y.N.; Ma, K.; Zhu, J.; Huang, F.; Kuang, L.; Wang, X.; Li, S. Nondestructive determination of soluble solids content in intact apples using a self-made portable NIR diffuse reflectance instrument. *Infrared Phys. Technol.* **2023**, *132*, 104714. [CrossRef]
12. Mansuri, S.M.; Chakraborty, S.K.; Mahanti, N.K.; Pandiselvam, R. Effect of germ orientation during Vis-NIR hyperspectral imaging for the detection of fungal contamination in maize kernel using PLS-DA, ANN and 1D-CNN modeling. *Food Control* **2022**, *139*, 109077. [CrossRef]
13. Shih, M.S.; Chang, K.C.; Chou, S.A.; Liu, T.S.; Ouyang, Y.C. The Automated Detection of Fusarium Wilt on Phalaenopsis Using VIS-NIR and SWIR Hyperspectral Imaging. *Remote Sens.* **2023**, *15*, 4174. [CrossRef]
14. Qiao, S.; Tian, Y.; Gu, W.; He, K.; Yao, P.; Song, S.; Wang, J.; Wang, H.; Zhang, F. Research on simultaneous detection of SSC and FI of blueberry based on hyperspectral imaging combined MS-SPA. *Eng. Agric. Environ. Food* **2019**, *12*, 540–547. [CrossRef]
15. Zheng, Y.; Cao, Y.; Yang, J.; Xie, L. Enhancing model robustness through different optimization methods and 1-D CNN to eliminate the variations in size and detection position for apple SSC determination. *Postharvest Biol. Technol.* **2023**, *205*, 112513. [CrossRef]
16. *Q/YNKG 12*; 2020 Quality Grading Standard for Fresh Fruit of Chuliang Longan. Fruit Tree Research Institute of Guangdong Academy of Agricultural Sciences: Guangzhou, China, 2020.
17. Ashtiani, S.H.M.; Javanmardi, S.; Jahanbanifard, M.; Martynenko, A.; Verbeek, F.J. Detection of mulberry ripeness stages using deep learning models. *IEEE Access* **2021**, *9*, 100380–100394. [CrossRef]
18. Guo, P.; Li, T.; Gao, H.; Chen, X.; Cui, Y.; Huang, Y. Evaluating calibration and spectral variable selection methods for predicting three soil nutrients using Vis-NIR spectroscopy. *Remote Sens.* **2021**, *13*, 4000. [CrossRef]
19. Ye, S.; Wang, D.; Min, S. Successive projections algorithm combined with uninformative variable elimination for spectral variable selection. *Chemom. Intell. Lab. Syst.* **2008**, *91*, 194–199. [CrossRef]
20. Zhan, B.; Li, P.; Li, M.; Luo, W.; Zhang, H. Detection of Soluble Solids Content (SSC) in Pears Using Near-Infrared Spectroscopy Combined with LASSO–GWF–PLS Model. *Agriculture* **2023**, *13*, 1491. [CrossRef]
21. Sohn, S.I.; Oh, Y.J.; Pandian, S.; Lee, Y.H.; Zaukuu, J.L.Z.; Kang, H.J.; Ryu, T.H.; Cho, W.S.; Cho, Y.S.; Shin, E.K. Identification of Amaranthus species using visible-near-infrared (vis-NIR) spectroscopy and machine learning methods. *Remote Sens.* **2021**, *13*, 4149. [CrossRef]
22. Ryu, D.S.; Noh, S.H.; Hwang, I.G. Preprocessing effects on on-line SSC measurement of Fuji apple by NIR spectroscopy. *Korean Soc. Agric. Mach.* **2000**, *11*, 560–568.
23. Cheng, T.; Guo, S.; Pan, Z.; Fan, S.; Ju, S.; Xin, Z.; Zhou, X.; Jiang, F.; Zhang, D. Near-infrared model and its robustness as affected by fruit origin for 'dangshan' pear soluble solids content and pH measurement. *Agriculture* **2022**, *12*, 1618. [CrossRef]
24. Liu, Y.; Sun, X.; Ouyang, A. Nondestructive measurement of soluble solid content of navel orange fruit by visible–NIR spectrometric technique with PLSR and PCA-BPNN. *LWT* **2010**, *43*, 602–607. [CrossRef]

25. Chen, Y.; Li, Y.; Williams, R.A.; Zhang, Z.; Peng, R.; Liu, X.; Xing, T. Modeling of soluble solid content of PE-packaged blueberries based on near-infrared spectroscopy with back propagation neural network and partial least squares (BP–PLS) algorithm. *J. Food Sci.* **2023**, *88*, 4602–4619. [CrossRef]
26. Tian, S.; Liu, W.; Xu, H. Improving the prediction performance of soluble solids content (SSC) in kiwifruit by means of near-infrared spectroscopy using slope/bias correction and calibration updating. *Food Res. Int.* **2023**, *170*, 112988. [PubMed]

Applied Thermal Engineering 272 (2025) 126437

Contents lists available at ScienceDirect

Applied Thermal Engineering

journal homepage: www.elsevier.com/locate/apthermeng

Research Paper

Detection and grading of oxidation for copper–water heat pipe wicks based on the machine learning methods

Xiaojun Guo[a], Yong Li[a,*], Guangwen Huang[b,*], Rui Tang[c], Fan Yang[a,d], Zhifeng Xin[d], Bowen Wu[a]

[a] School of Mechanical and Automotive Engineering, South China University of Technology, Guangzhou 510640, China
[b] College of Engineering, South China Agricultural University, Guangzhou 510642, China
[c] China Mobile (Chengdu) Information Telecommunication Technology Co.,Ltd., Chengdu 610041, China
[d] Lenovo (Beijing) Limited, Beijing 100094, China

ARTICLE INFO

Keywords:
Copper–water heat pipe
Wick
Oxidation detection
Machine vision
Machine learning

ABSTRACT

Wicks are core components of heat pipes, and the oxidation of wicks can directly lead to a decrease in the performance or failure of heat pipes. Traditional oxidation detection methods have their own advantages and disadvantages and cannot be directly used for oxidation detection of heat pipe wicks in actual production. In this study, experiments are combined with machine vision and machine learning methods to detect the oxidation on copper–water heat pipe wicks, and a machine learning grading model is constructed. The results show that the colour characteristics, the capillary climb performance of the wick, the heat transfer performance of the heat pipe can be used to characterize the degree of oxidation of the wick. Using the colour characteristics and images of the wick separately as inputs for the model can achieve oxidation grading of the wick, and the average grading accuracies reach over 80% and 85%, respectively. Compared with models that rely on colour features for oxidation grading, models that use images as input and extract the image features through convolution for oxidation grading of the wicks can extract more advanced features in addition to colour features; this results in higher grading accuracy of the model. In addition, using the colour features of the wick and the image together as the model inputs, the colour features are concatenated with the image convolution features, and an attention mechanism is introduced into the model and greatly improves the classification accuracy of the model. The overall classification accuracy of the improved and optimized model in this study reaches over 92%, and the highest reaching over 97% and 95% for the training and testing sets, respectively. Thus, high-precision oxidation classification of the wick is attained, the accuracy of this model can meet the actual production needs.

1. Introduction

The wick is a key component that affects the heat transfer performance of heat pipes [1–3]. In actual production, oxidation of the wick directly causes the wick to change from hydrophilic to hydrophobic, while the capillary pressure decreases [4–6]; this results in a decrease or failure of the heat transfer performance of heat pipes. To ensure the efficient and reliable operation of heat pipes, the semifinished heat pipes often need to be cut after sintering and annealing processes during heat pipe manufacturing. The capillary properties of the internal wick are analysed through capillary climb experiments to determine whether the wick has oxidized. The semifinished heat pipes with oxidized wicks are restricted from entering the next process to ensure heat pipe performance. However, with the continuous improvement in production capacity, the current method of relying on manual observation and analysis of capillary performance to determine the oxidation of wicks is time-consuming, laborious, strongly influenced by subjective factors, and difficult to analyse online. This leads to frequent outflow of semifinished heat pipes with oxidized wicks, greatly limiting production efficiency and reducing heat pipe performance; hence, the needs of actual production can no longer be met. Therefore, seeking a practical method for detecting and grading the oxidation of wicks in heat pipes has become an urgent and particularly important problem that needs to be solved in current heat pipe production.

For oxidation detection methods, the current methods mainly

---

* Corresponding authors at: School of Mechanical and Automotive Engineering, South China University of Technology, Guangzhou 510640, China (Y. Li). College of Engineering, South China Agricultural University, Guangzhou 510642, China (G. Huang).

E-mail addresses: meliyong@scut.edu.cn (Y. Li), huanggw@scau.edu.cn (G. Huang).

https://doi.org/10.1016/j.applthermaleng.2025.126437
Received 21 January 2025; Received in revised form 15 March 2025; Accepted 3 April 2025
Available online 8 April 2025

Nomenclature

Symbols

R	red in the color space
G	green in the color space
B	blue in the color space
m_t	first-order xponential smoothing value of the gradient
$\hat{m}_t$	first-order exponential smoothing value of the modified gradient
$\Delta\theta$	the gradient square update value
η	the global learning rate
β_1	the exponential decay rates
loss	the loss function
w_t	the weight value at time t
H	hue
S	saturation
I	Intensity
v_t	second-order exponential smoothing value of the gradient square
$\hat{v}_t$	second-order exponential smoothing value of the modified gradient
θ_t	the updated parameter
ε	the small constant used for numerical stability
β_2	the exponential decay rates
u	the learning rate
b_t	the bias at time t

include titration, chromatography, and spectroscopy [7]. Among them, the titration method [8–13] is a method of detecting oxidation through oxidation-reduction reactions. Depending on the titrant, titration methods include the iodometric method, sodium nitrite method, potassium permanganate method, potassium dichromate method, cerium content method, potassium bromate method, bromine content method, and potassium periodate method. The titration method can directly determine substances with oxidizing or reducing properties and can indirectly determine substances that undergo quantitative reactions with oxidants or reducing agents. However, its reaction mechanism and process are generally complex, and the reaction rate is slow and often accompanied by side reactions. The medium usually has a significant effect on the reaction process. For metal oxides, quantitative analysis is usually carried out via acid-base titration after dissolution to determine the composition of the substance. Titration method can be used to detect most metal or non-metal oxides, but the oxidation detection method for wicks of heat pipes in production usually requires the following characteristics: fast detection speed, high accuracy, low cost, non-destructive testing and does not require professional testing personnel with rich knowledge and skills, so this method cannot be used for oxidation detection of wicks. Chromatography [14,15] is a physical and chemical analysis method that utilizes different intermolecular forces (distribution, adsorption, ion exchange, etc.) between the different solutes and stationary and mobile phases. When the two phases move relative to each other, the solutes undergo multiple equilibrium separations between the two phases, and oxidation detection is ultimately achieved. Chromatography can be divided into gas chromatography and liquid chromatography according to the type of mobile phase. Gas chromatography [16,17] uses a gas phase (usually hydrogen, nitrogen, helium) as the mobile phase to qualitatively and quantitatively analyse volatile oxidation products. The advantages of this method are high resolution, high sensitivity, and fast detection. The disadvantages are expensive detection equipment, a relatively single detection object, detection of only volatile and semi-volatile compounds, and inability to detect thermally unstable and high-molecular-weight compounds [18–21]. Liquid chromatography [22–24] often uses a liquid phase (usually water, alcohol, and organic solvents) as the mobile phase to detect various types of oxides. The advantages of this method include high efficiency, high sensitivity, and rapid determination of multiple components. The disadvantages are expensive detection equipment, complex operation, and high requirements for sample pretreatment. Overall analysis, although chromatography (gas chromatography and liquid chromatography) has been widely used in oxide detection, but for metal oxides, this method is not entirely applicable, so this method is also not suitable for oxidation detection of wicks. Spectral analysis [25–30] is based on the interaction between matter and light. When light comes into contact with matter, the substance absorbs, emits, or scatters light of specific wavelengths, forming specific spectral features. By analysing and measuring these spectral features, the composition and properties of a substance can be inferred. The spectral regions based on the different wavelengths can generally be divided into visible, near-infrared, far-infrared, and ultraviolet. The types of spectra can be divided into emission, absorption, and scattering. The advantages of spectroscopy include fast detection speed, high accuracy, minimal sample damage, and the ability to simultaneously determine multiple elements or compounds. The disadvantages are the need for professional knowledge and skills, expensive equipment, and lab-based instrumentation for testing and research. For metal oxides, commonly used spectral detection methods mainly include XRS detection, EDX detection, and TEM detection. Among them, X-ray diffraction (XRD) can detect the crystal structure and phase composition of metal oxides [31,32], energy dispersive X-ray (EDX) can detect the morphology and chemical composition of metal oxides [33,34], and transmission electron microscopy (TEM) [35,36] can detect the microstructure and crystal defects of metal oxides. At present, the detection of metal oxides or non-metal oxides mostly adopts spectroscopic methods, but spectral detection methods usually require expensive instruments and professional personnel, according to the detection requirements of wicks in production, so these spectroscopic methods are usually not suitable for oxidation detection of wicks in production. In summary, current oxidation detection methods have their own advantages and disadvantages and different application scenarios and scopes. The advantages of each method complement each other, and they have achieved notable achievements and wide applications in oxidation detection. But the oxidation detection method for wicks of heat pipes in production usually requires the following characteristics: fast detection speed, high accuracy, low cost. Current detection methods (titration, chromatography, and spectroscopy) do not have the above characteristics. Thus, all of them cannot be truly used for oxidation detection of wicks in heat pipe production. Therefore, by drawing on some new technologies and methods to explore the oxidation detection method for wicks of heat pipes in production, and a oxidation detection method that meets the production requirements is proposed, which has theoretical significance and practical value, and is worthy of special research.

Based on the above analysis, a certain number of copper–water heat pipes of different types are designed and manufactured, and samples with different degrees of oxidation using natural oxidation are developed. According to the actual situation and experimental results, the oxidation grading index and standard of the wick are determined (the oxidation grading index of wicks refers to the physical quantity that can characterize the degree of oxidation of the wick, the grading standard for wicks refers to the quantitative relationship between the degree of oxidation of wicks and the physical quantities that characterize the oxidation of wicks). A dataset of wick colour characteristics and an image dataset are established, and machine vision and machine learning methods are combined to examine the oxidation detection grading of heat pipe wicks in production, with the aim to obtain a wick oxidation detection grading method that meets production requirements. This study proposes a new method for detecting the degree of oxidation of wicks, which greatly improves the efficiency and reliability of oxidation detection for wicks of heat pipes, provides guarantees for the production

Table 1
Copper powder information.

Specification	Visual density standard	copper powder mesh percentage(%)				
		>60 mesh	60 ~ 80 mesh	80 ~ 100 mesh	100 ~ 150 mesh	<150 mesh
Coarse powder	1.4 ~ 1.5	58 % ~65 %	≥30 %		other	≤3%
Fine powder	1.6 ~ 1.8	≤3%	other		45 % ~50 %	≤10 %
Mixed powder	1.85 ~ 2.0	≤10 %	60 %~65 %		other	≤8%

of heat pipes, and also provides a new idea for rapid online detection of oxidation of metal products.

2. Methods

2.1. *Raw material selection and samples preparation*

In this study, commonly used oxygen-free copper tubes and copper powder were used as raw materials in the actual production of the heat pipes. Copper powder could be divided into three types according to the mesh size and ratio: coarse powder, fine powder, and mixed powder. The detailed information is listed in Table 1, and the copper powder and copper tube are shown in Fig. 1. In Table 1, the sum of the percentages of copper powders with different mesh sizes is 1, and "othrer" refers to the sum of the percentages of copper powders with 60–80 mesh and 80–100

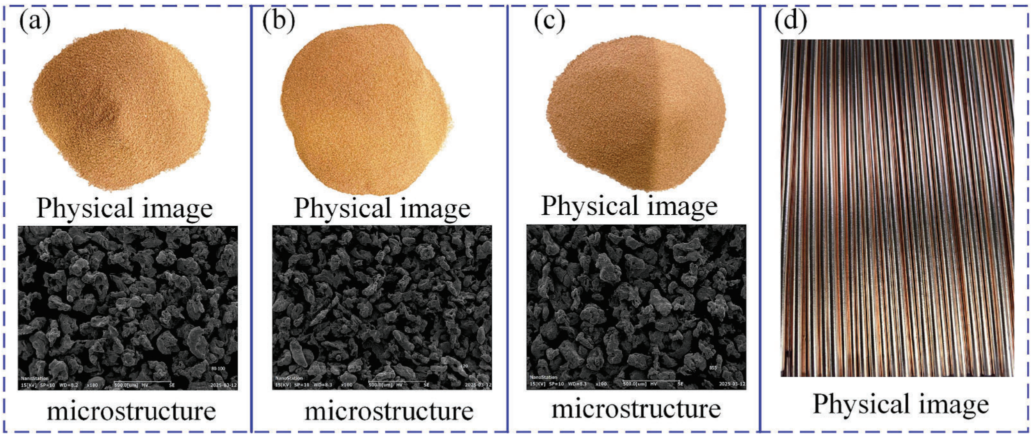

Fig. 1. Schematic diagram of the raw materials: (a) coarse powder, (b) fine powder, (c) mixed powder, and (d) copper tube.

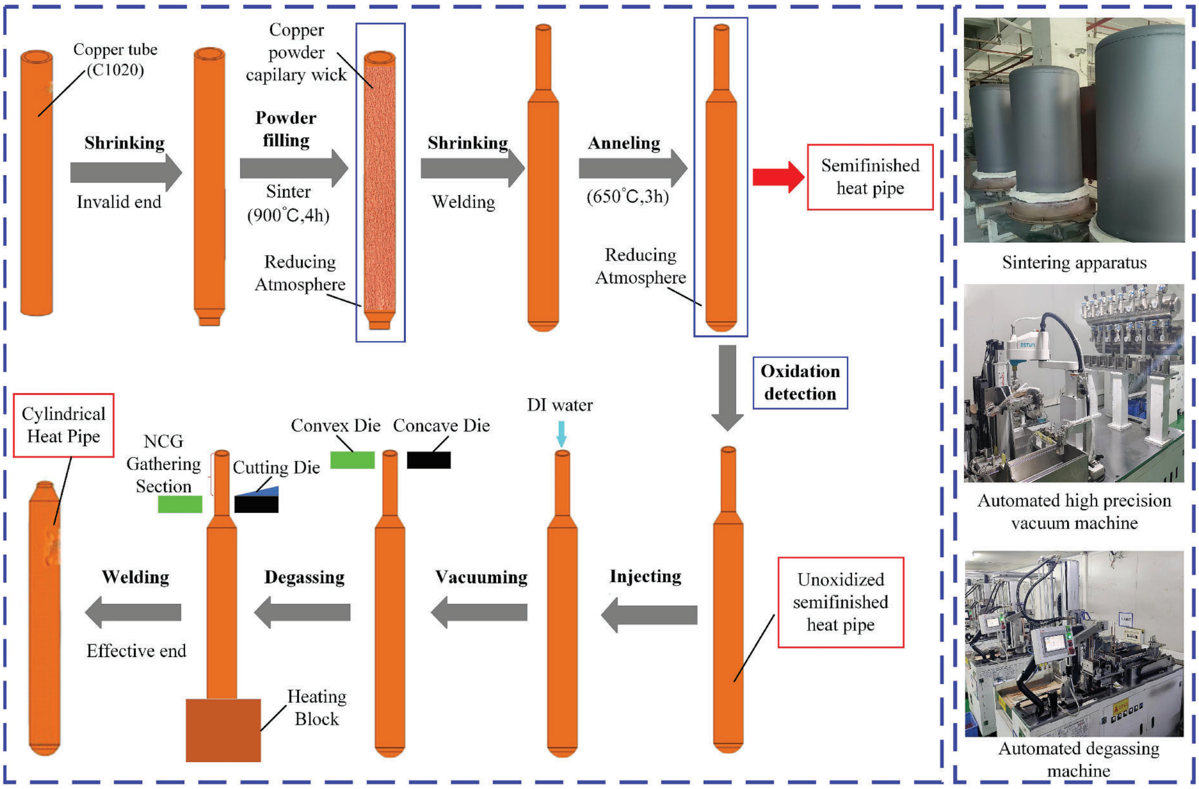

Fig. 2. Heat pipe manufacturing process and main equipment.

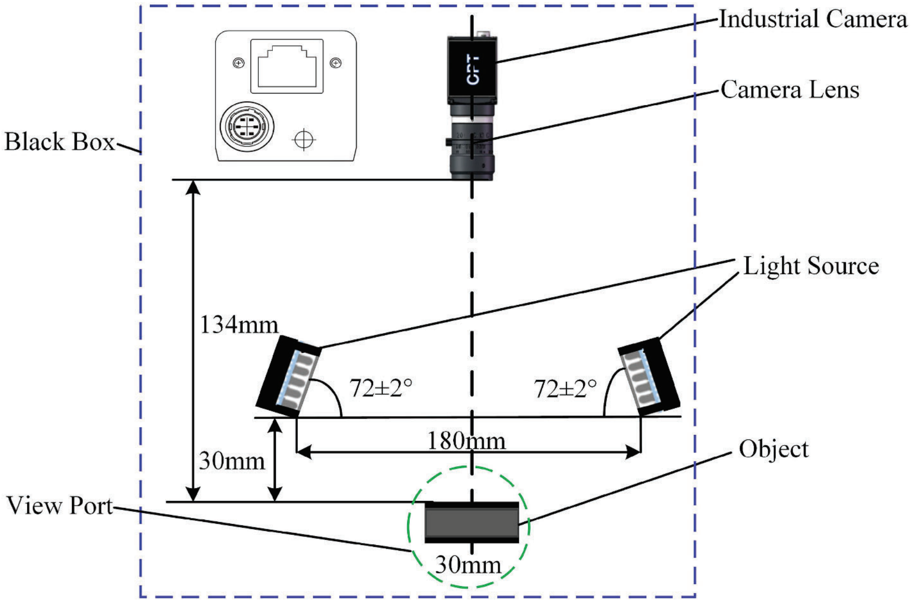

Fig. 3. Schematic diagram of the image acquisition system.

mesh remaining after removing the percentages of copper powders with other mesh sizes. In the production process of the heat pipes [37–39], as shown in Fig. 2, three different wick types (coarse-powder wick, fine-powder wick, and mixed-powder wick) are created by sintering inside oxygen-free copper pipes. The semifinished heat pipes after sintering and annealing were stored as experimental samples for subsequent research. Here, 600 coarse-powder semifinished heat pipes (semifinished heat pipes formed by sintering coarse powder into a wick structure and annealing), 600 fine-powder semifinished heat pipes (semifinished heat pipes formed by sintering fine powder into wick structure and annealing), and 600 mixed-powder semifinished heat pipes (semifinished heat pipes formed by sintering mixed powder into a wick structure and annealing) were prepared. All semifinished heat pipes were 300 ± 0.3 mm long, with an outer diameter of 6 ± 0.03 mm, a powder thickness of 0.85 ± 0.05 mm, and an oxygen-free copper pipe wall thickness of 0.25 ± 0.05 mm.

2.2. Experimental design

The coarse-powder semifinished heat pipes, fine-powder semifinished heat pipes, and mixed-powder semifinished heat pipes were placed in an environment at a constant temperature of 25 °C, and samples with different degrees of oxidation were formed using long-term natural oxidation. Generally, with increasing placement time of the sample, more severe oxidation of the sample occurred. Starting from the completion time of semifinished heat pipe production, samples were collected daily for experiments and collected for a total of 15 days. The experimental data were analysed to determine the oxidation grading index and standard of the wick, and an oxidation grading model was constructed to determine the wick oxidation. After daily sampling, the following experiments were conducted synchronously:

2.2.1. Experiments on the image acquisition and colour feature extraction analysis of wicks

Ten samples were randomly collected from coarse-powder semifinished heat pipes, ten samples were randomly collected from fine-powder semifinished heat pipes, and ten samples were randomly collected from mixed-powder semifinished heat pipes. All the samples were sliced and flattened to obtain wick samples. To facilitate image acquisition, the samples were made into blocks with a length of 100 mm, width of 35 mm, and thickness of 1.1 mm. An image acquisition system was used to obtain RGB images of different types of wick samples; the images were processed and analysed; the colour feature values of R, G, B, H, S, and I were extracted; and the data were recorded and analysed. Among them, RGB is a color model based on the principle of additive color mixing, and its colors are represented by the intensity combination of red, green, and blue channels. Among them, R represents red, G represents green, and B represents blue. The range of intensity values for each channel of R, G, and B is generally 0–255. When the values of R, G, and B are 0, it represents black, and when they are all 255, it represents white. HSI is a color model based on human perception, which decomposes color into three independent components: hue, saturation, and brightness, which is more in line with human intuitive understanding of color. Among them, H represents hue, S represents saturation, and I represents intensity. The value range of H is 0° − 360°, normalized to 0–1, the value range of S is 0–1, and the value range of S is 0–1. When the color is black, the value is 0, and when the color is white, the value is 1. A schematic diagram of the image acquisition system is shown in Fig. 3. The periphery of the system was a dark room structure with a length of 600 mm, width of 600 mm, and height of 600 mm. The inner wall of the dark room was covered with a silver white screen, and four LED strips were arranged at equal distances from the top of the dark room. The dark room was equipped with multifunctional visual support, which could adjust the camera and visual light source at any angle and height. The camera (an OPT-CC1200-GL-16 series industrial camera with a resolution of 4024 × 3036 and an exposure time of 5.5 ms) was placed at the top of the bracket, and the camera lens was approximately 134 mm away from the sample. Two light sources (the OPT-LI11532-W-V4.0U strip light source with a light intensity of 200) were symmetrically placed on both sides of the bracket, approximately 180 mm apart, and complementary to the vertical direction at a 72° angle. The bottom of the bracket was covered with black light absorbing material and had a sample placement area marked for easy sample placement. During the actual operation of the system, the computer was connected to the camera via Ethernet, and the camera was triggered by the software to capture images, and the images were then stored and analysed.

2.2.2. Capillary climbing experiment of wicks

Ten samples were randomly collected from coarse-powder semifinished heat pipes, ten samples were randomly collected from fine-powder semifinished heat pipes, and ten samples were randomly collected from mixed-powder semifinished heat pipes. All the samples

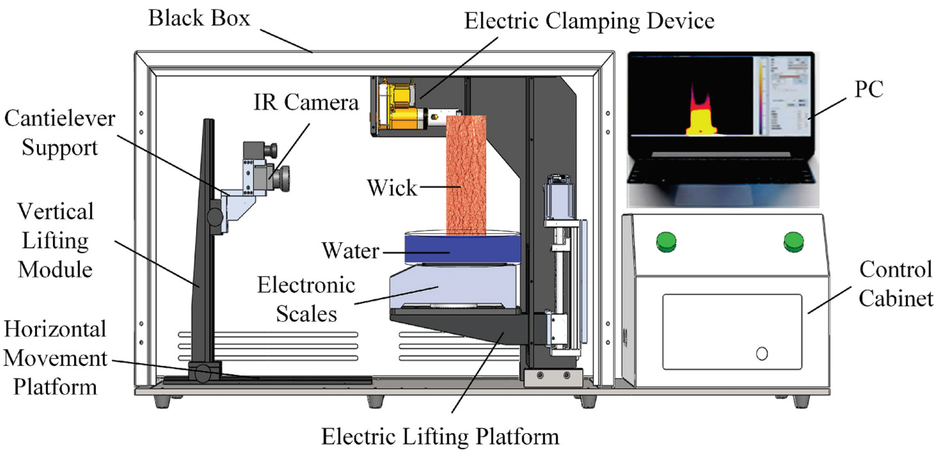

Fig. 4. Schematic diagram of the capillary performance testing system.

Table 2
Basic parameters of the infrared camera.

Camera model	Resolution	Thermal sensitivity	Measuring range	Digital zoom	Pixel spacing	Frame rate
Fotric225s	320 × 240	<50 mk @30 °C	−20 °C°~150 °C	1–8 multiples	17 μm	60 Hz

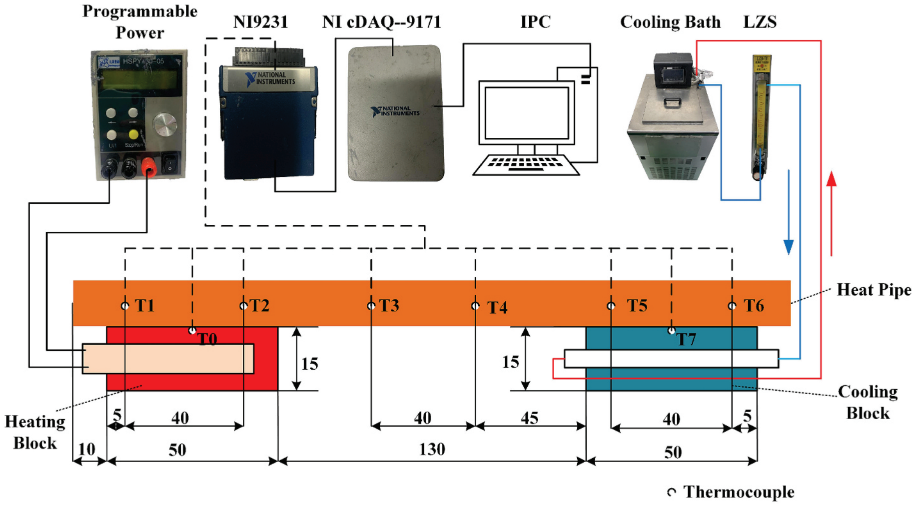

Fig. 5. Schematic diagram of the heat transfer performance testing for heat pipes.

were flattened to obtain the wick samples. The capillary performance testing system was used to obtain the climb height of the working fluid in the wick within 15 s to determine the quality of the capillary performance of the wick. Fig. 4 shows a schematic diagram of the capillary performance testing system for the wicks [40]. The system consists of three parts: a testing module, a recording module, and a control cabinet. The testing module is surrounded by a black box with an adjustable platform inside. The upper cantilever structure can clamp the wick, and the lower container contains a mixture of ice and water as the working fluid. The recording module consists of an infrared camera, a cantilever support platform, a vertical lifting module, a horizontal moving platform, and a computer. The basic parameters of the infrared camera are listed in Table 2. After calibration, the temperature measurement error of the infrared camera is less than 1 °C within the temperature range used in the experiment. The movement of the platform is controlled through the control cabinet. During actual testing, the lower end of the wick is placed 20 mm underwater by adjusting the lifting platform, and the temperature rise of the wick sample is recorded by an infrared camera to examine the capillary performance of the wick.

2.2.3. *Experimental analysis of the heat transfer performance of heat pipes*

Ten samples were randomly collected from coarse-powder semifinished heat pipes, ten samples were randomly collected from fine-powder semifinished heat pipes, and ten samples were randomly collected from mixed-powder semifinished heat pipes. All selected semifinished heat pipes are made into circular straight heat pipes. The actual liquid injection volume of the heat pipe is 85 % of the saturated water absorption capacity of the wick. The heat transfer performance of the heat pipe was tested at different powers (70 W, 75 W, 80 W, 85 W, and 90 W), and the data were recorded and analysed. Fig. 5 shows a schematic diagram of the principle of heat transfer performance testing for the heat pipes. The system consists of three parts: a heating module, a cooling module, and a temperature data acquisition module. The heating module consists of a heating copper block, a heating rod, and a programmable power supply. The heating rod is inserted into the heating copper block, and the heating power is adjusted using the

Table 3
Main components and relevant parameters of the test system.

Component	Model or size	Parameters
Heating tube	Φ8*30 mm	60 V, 200 W
Adiabatic Bakelite	/	0.023 W/(m·K)
Laptop	Lenovo	/
Programmable power supply	HSPY-200–5	output voltage: 0 ~ 200 V output current: 0 ~ 5 A voltage accuracy: 0.3 %+200 mV current accuracy: 0.5 %+3 mA
T-type thermocouple	wire diameter: 0.1 mm	temperature range: −200 °C ~ 200 °C
Temperature acquisition card	NI9213 + cDAQ-9171	acquisition channel: 32 CHs
Thermostatic water tank	FA-0092	accuracy: 0.1 °C
Thermal grease	VK-887	thermal conductivity: 6 W/(m·K) temperature range: −40 °C~+180 °C
Rotameter	LZM-15Z/ZT	range: 1 ~ 11 L/min accuracy: 1 %

programmable power supply. The cooling module consists of a cooling copper block, a constant-temperature water tank, and a rotor flow metre. The cooling copper block is connected to the constant-temperature water tank and the rotor flow metre, and heat is carried away by the cooling water. The cooling water temperature is set to 25℃, and the cooling water temperature error is less than 0.1℃. The temperature data acquisition module mainly consists of a computer, a temperature input module (NI9213 + cDAQ-9171), and 8 T-type thermocouples. The distribution of thermocouples is shown in Fig. 5, where T0 represents the temperature of the heat source and T7 represents the temperature of the cooling water. During actual testing, the head and tail of the heat pipe are horizontally placed on top of the heating copper block and the cooling copper block, respectively. Thermal conductive silicone grease is used to reduce the thermal resistance in the evaporation and condensation areas, and the testing system is insulated. Among them, the insulation material is rubber insulation cotton, with a thermal conductivity of: (0.032–0.040) W/m·K, the thickness of the insulation cotton is 30 mm. When the heat pipe reaches equilibrium, that is, when the temperature change within 30 s is less than 0.3 ℃, the data are recorded. The components and main parameters of the testing system are shown in Table 3. The average temperatures of the evaporation end Te, condensation end Tc, and insulation end Ta of the heat pipe are calculated according to equations (1)-(3), and the thermal resistance R is calculated according to equation (4).

$$T_e = \frac{T_1 + T_2}{2} \tag{1}$$

$$T_a = \frac{T_3 + T_4}{2} \tag{2}$$

$$T_c = \frac{T_5 + T_6}{2} \tag{3}$$

$$R = \frac{T_e - T_c}{P} \tag{4}$$

In equation (4), P represents the heating power.

2.3. Construction of the grading model

In this study, machine learning methods are used to establish a wick oxidation grading model, and the accuracy is selected as the indicator to evaluate the model performance. A higher accuracy correlates to a better model performance. Among the methods, the grading model mainly includes the back propagation (BP) neural network model, transfer learning model, and improved and optimized new model. Each model is shown below, and the accuracy calculation method of the model is shown in equation (5).

$$\text{accuracy} = \frac{TP + TN}{TP + TN + FP + FN} \tag{5}$$

In equation (5), TP represents the number of samples in which the actual oxidation level of the wick belongs to the positive category and the predicted oxidation level of the wick is also positive; TN represents the number of samples of wicks whose actual oxidation level is negative and whose predicted oxidation level is also negative; FP represents the number of samples of wicks whose actual oxidation level belongs to the positive category but whose predicted oxidation level belongs to the negative category; FN represents the number of samples in which the actual oxidation level of the wick belongs to the negative category but the predicted oxidation level of wicks belongs to the positive category.

2.3.1. BP neural network model

The BP neural network [41–43] is a multilayer feedforward neural network that works in two main stages: the first stage is the forward propagation of the signal, from the input layer through the hidden layer and finally to the output layer; the second stage is the backpropagation of the errors. By using a loss function, the weights and biases from the hidden layer to the output layer and from the input layer to the hidden layer are sequentially adjusted to minimize the error between the actual

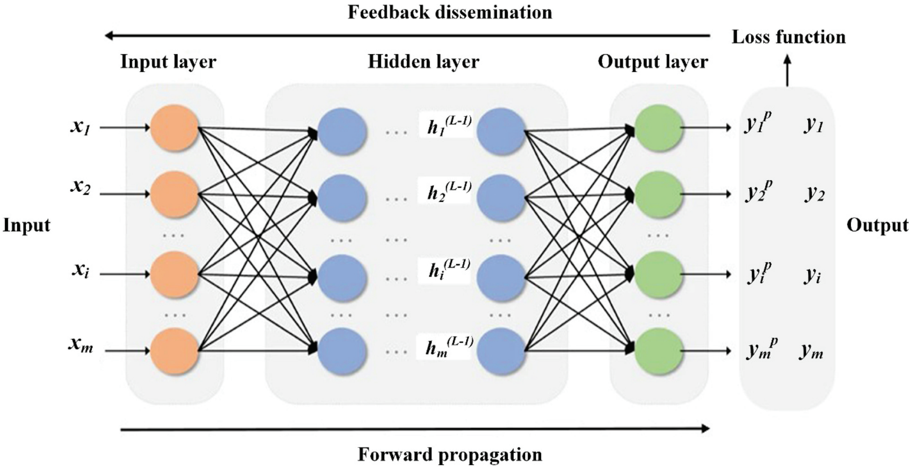

Fig. 6. Schematic diagram of the BP neural network.

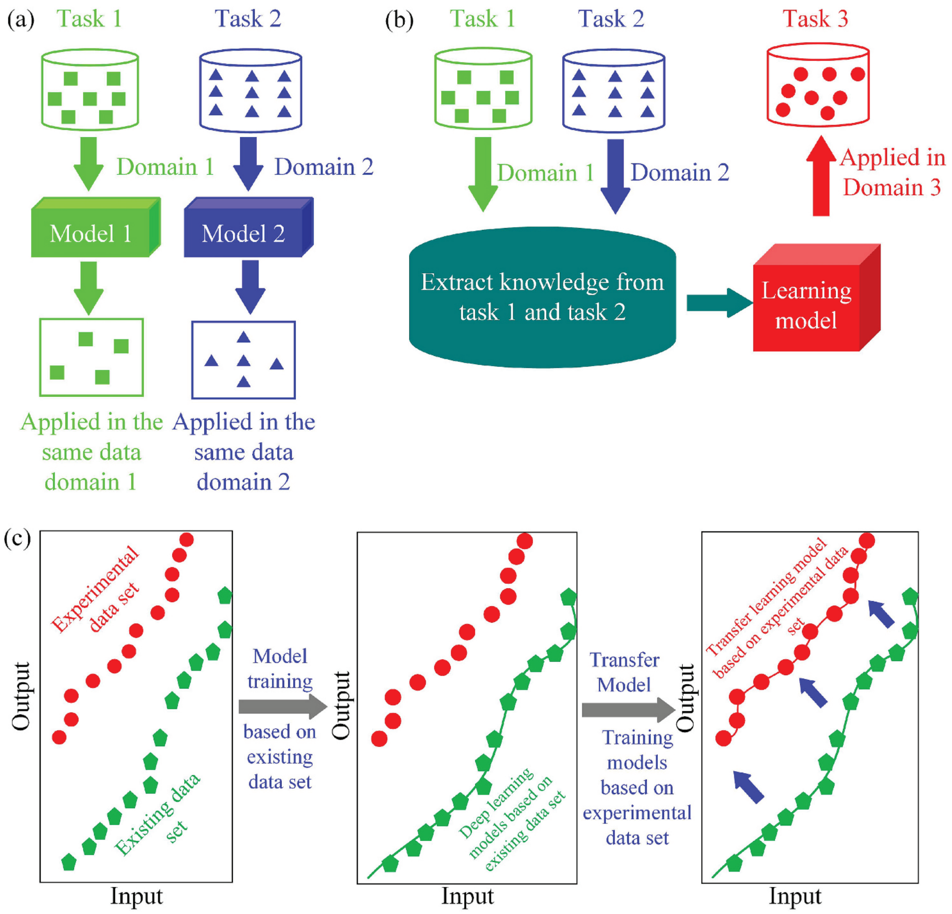

Fig. 7. Transfer learning methods: (a) traditional machine learning methods, (b) commonly used transfer learning methods, and (c) the transfer learning method used in this study.

output and the expected output of the model. The basic principle of the model is shown in Fig. 6. This paper is based on TensorFlow 2.3.0 to construct an oxidation classification model. In terms of data processing and visualization, numpy, pandas, matplotlib and other toolkits were called. In terms of data preprocessing, scikit learn, opencv python and other toolkits were called. The computer RAM uses Kingston HyperX Fury 64 GB (2 x 32 GB) DDR4 2666 MHz, and the GPU uses NVIDIA A100 (40 GB video memory). Among them, the gradient descent algorithm is used to update the weights and biases. The hidden layer of the model is activated using the S-shaped hyperbolic tangent tansig function, the output layer is activated using the purelin function, and the loss function loss is calculated using mean square error. The calculation methods for each activation function, loss function, and gradient update are shown in equations (6)-(10).

$$\mathrm{tansig}(z_j) = \frac{1 - e^{-2z_j}}{1 + e^{-2z_j}} \tag{6}$$

In equation (6), Zj represents the weighted input feature of the jth neuron in the hidden layer.

$$z_j = \sum_{i=1}^{n} w_{ji} x_i + b_j \tag{7}$$

In equation (7), w_{ji} represents the weight connecting the i-th neuron in the input layer and the j-th neuron in the hidden layer, x_i is the output of the i-th neuron in the input layer, and b_j is the bias term of the j-th neuron in the hidden layer.

$$\mathrm{purelin}(x) = x \tag{8}$$

In equation (8), x represents the weighted calculation output feature of the last hidden layer.

$$\mathrm{loss} = \frac{\sum_{i=1}^{n} \left(y_i - y_i^p\right)^2}{n} \tag{9}$$

In equation (9), y_i represents the actual result, and y_i^p represents the predicted output result.

$$w_{t+1} = w_t - u\frac{\partial loss}{\partial w_t} \qquad b_{t+1} = b_t - u\frac{\partial loss}{\partial b_t} \tag{10}$$

In equation (10), w_{t+1} is the weight value at time t + 1, w_t is the weight value at time t, b_{t+1} is the bias at time t + 1, b_t is the bias at time t, u represents the learning rate, and loss is the loss function.

2.3.2. *Transfer learning model*

Transfer learning [44,45] is a machine learning method and has the core concept of transferring knowledge or models learned from one task (source task) to another related task (target task) to improve the performance of the new task. This method fully utilizes existing data and model resources. After establishing a model on the existing data, the model is retrained and fine-tuned using the existing data; this process reduces the dependence of the target task on a large amount of new data, accelerates the model training speed, and improves the model generalization ability. A model with effective problem-solving ability is constructed, and the basic principle is shown in Fig. 7 (a) and (b) [46]. This paper is based on TensorFlow 2.3.0 to construct an oxidation classification model. In terms of data processing and visualization, numpy, pandas, matplotlib and other toolkits were called. In terms of data

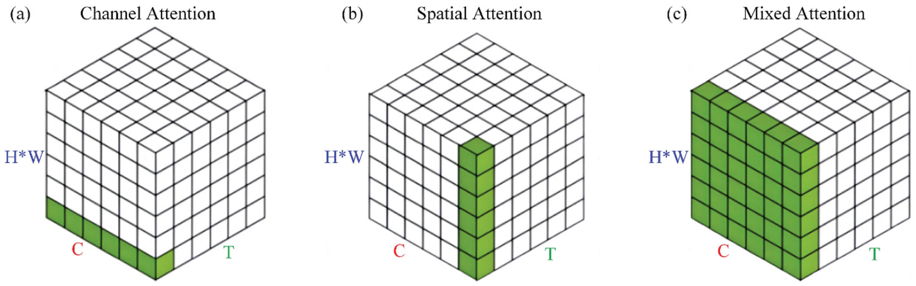

Fig. 8. Attention mechanism methods (C represents the channel, H * W represents the spatial domain, and T represents the temporal domain): (a) Channel attention mechanism, (b) spatial attention mechanism, and (c) mixed attention mechanism.

preprocessing, scikit learn, opencv python and other toolkits were called. The computer RAM uses Kingston HyperX Fury 64 GB (2 x 32 GB) DDR4 2666 MHz, and the GPU uses NVIDIA A100 (40 GB video memory). Among them, the existing deep convolutional models are migrated, some convolutional layers are frozen, and existing experimental data are used to retrain and fine-tune model parameters to achieve oxidation grading. The overall process is shown in Fig. 7 (c). Among them, the convolutional layer of the model adopts Relu activation, the output layer adopts Softmax activation, the loss function loss is calculated using the sparse_category_crossentropy method, and overfitting is suppressed using droupt with a value of 0.2. The Adam algorithm is used to optimize the model. The calculation methods for each activation function, loss function and the process of updating weights using the Adam algorithm are shown in equations (11)-(20), respectively.

$$\mathrm{Relu}(x) = \begin{cases} x, & x \geqslant 0 \\ x, & x < 0 \end{cases} \tag{11}$$

In equation (11), x represents the convolutional feature.

$$\mathrm{softmax}(x_i) = \frac{e^{x_i}}{\sum_{i=1}^{n} e^{x_i}} \tag{12}$$

In equation (12), xi represents the convolutional feature.

$$\mathrm{loss} = -\frac{1}{m}\sum_{i=1}^{m}\sum_{j=1}^{k} p(x_{ij})\log(q(x_{ij})) \tag{13}$$

In equation (13), m represents the number of samples, k represents the category of samples, p(xij) represents the true probability that i belongs to category k, and q(xij) represents the predicted probability that i belongs to category k.

The specific process of updating weights using the Adam algorithm is as follows:

The gradient is calculated as follows:

$$g_t = \nabla_\theta J(\theta_{t-1}) \tag{14}$$

The gradient first-order exponential smoothing is calculated as follows:

$$m_t = \beta_1 m_{t-1} + (1-\beta_1) g_t \tag{15}$$

The gradient second-order exponential smoothing is calculated as follows:

$$v_t = \beta_2 v_{t-1} + (1-\beta_2)(g_t \odot g_t) \tag{16}$$

the corrected first-order exponential smoothing is calculated as follows:

$$\hat{m}_t = \frac{m_t}{(1 - \beta_1^t)} \tag{17}$$

The corrected second-order exponential smoothing is calculated as follows:

$$\hat{v}_t = \frac{v_t}{(1 - \beta_2^t)} \tag{18}$$

The gradient update is calculated as follows:

$$\Delta\theta = \eta \frac{\hat{m}_t}{\left(\varepsilon + \sqrt{\hat{v}_t}\right)} \tag{19}$$

The parameter update is calculated as follows:

$$\theta_t = \theta_{t-1} - \Delta\theta \tag{20}$$

In equations (14)-(20), g_t represents the gradient at time t, m_t represents the first-order exponential smoothing value of the gradient, v_t represents the second-order exponential smoothing value of the gradient square, $\hat{m}_t$ represents the first-order exponential smoothing value of the modified gradient, $\hat{v}_t$ represents the second-order exponential smoothing value of the modified gradient, $\Delta\theta$ represents the gradient square update value, θ_t represents the updated parameter, η represents the global learning rate, ε represents the small constant used for numerical stability, and β_1 and β_2 represent the exponential decay rates and has values ranging from 0 to 1.

2.3.3. *Improving and optimizing the model*

The attention mechanism [47–49] simulates the selective attention of human vision and can automatically focus on the most relevant information in massive data, thereby improving model efficiency and accuracy; thus, this mechanism has become one of the key technologies to enhance model performance. The common attention mechanisms in the visual field include the channel attention mechanism, spatial attention mechanism, and mixed attention mechanism; their working principles are shown in Fig. 8. To further improve the performance of the model, a model with a better grading effect is selected based on the grading results of transfer learning models, and this model is combined with attention mechanism methods to construct a new oxidation grading model, which is called the improved and optimized model. A model is built on TensorFlow 2.3.0, and the model is trained and tested.

3. Results and discussion

3.1. *Analysis of the colour feature parameters of the wick images*

Machine vision systems are used to collect images of different types of wicks, the color feature parameters of the three channel image of the wick were extracted through digital image processing methods. The specific process is as follows: image acquisition of the wick, image enhancement, image segmentation, image binarization, image morphological changes, edge detection, image recombination, and feature parameter calculation. Calculate the average color feature values of the wick images obtained daily, and analyze the changes in color feature values with sampling time. The results are shown in Fig. 9.

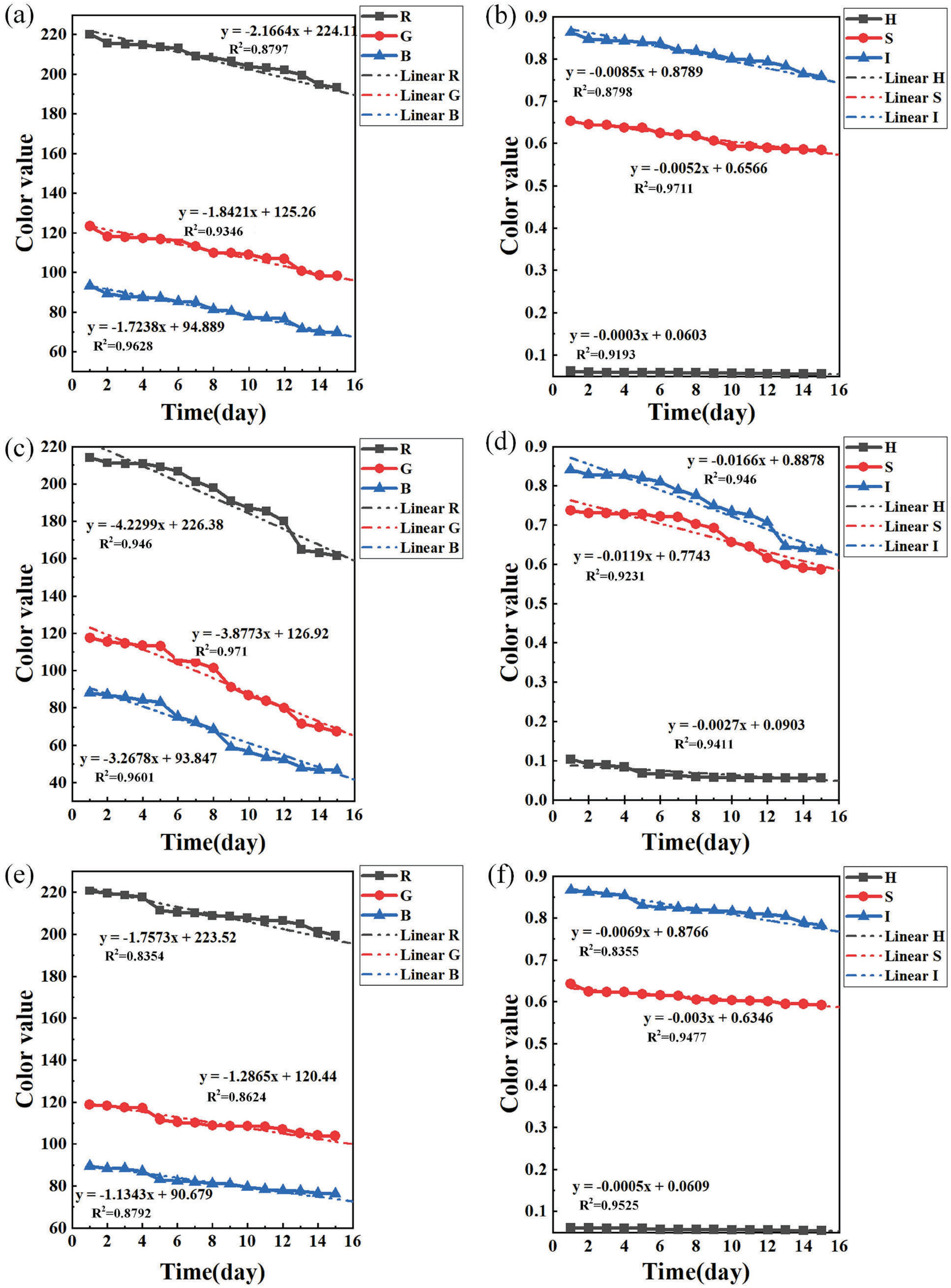

Fig. 9. Changes in the colour characteristics of wicks with sampling time: (a) RGB colour characteristics of the coarse-powder wicks, (b) HSI colour characteristics of the coarse-powder wicks, (c) RGB colour characteristics of the fine-powder wicks, (d) HSI colour characteristics of the fine-powder wicks, (e) RGB colour characteristics of the mixed-powder wicks, (f) HSI colour characteristics of the mixed-powder wicks.

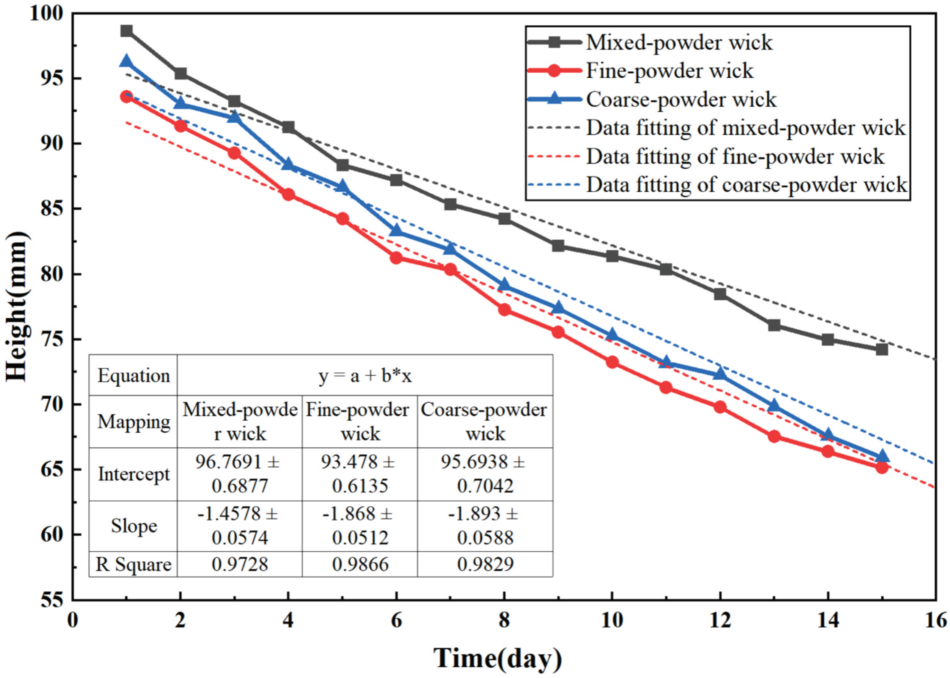

Equation	y = a + b*x		
Mapping	Mixed-powder wick	Fine-powder wick	Coarse-powder wick
Intercept	96.7691 ± 0.6877	93.478 ± 0.6135	95.6938 ± 0.7042
Slope	-1.4578 ± 0.0574	-1.868 ± 0.0512	-1.893 ± 0.0588
R Square	0.9728	0.9866	0.9829

Fig. 10. Experimental results of the capillary climb performance of wicks.

As shown in Fig. 9, the colour characteristics (R, G, B, H, S, I) of the images of the coarse-powder wick, fine-powder wick, and mixed-powder wick samples all show decreasing trends with increasing sampling time, and each colour characteristic is negatively correlated with the sampling time. Among them, the value range of the R, G, and B colour features is between 0–255, and the value range of the H, S, and I colour features is between 0–1. The differences between the maximum and minimum values of each colour feature (R, G, B, H, S, and I) in the coarse-powder wick image are 46.63, 36.24, 32.18, 0.007, 0.082, and 0.182, respectively. The differences between the maximum and minimum values of each colour feature (R, G, B, H, S, and I) in the fine-powder wick image are 68.02, 54.99, 45.51, 0.051, 0.155, and 0.266, respectively. The differences between the maximum and minimum values of each colour feature (R, G, B, H, S, and I) in the mixed-powder wick image are 40.03, 28.01, 24.86, 0.060, 0.642, and 0.865, respectively. The maximum values of all color features are obtained at the beginning of the experiment, and the minimum values are obtained at the end of the experiment. The reason is that when the heat pipe is exposed in the air, the copper-powder wick inside the heat pipe is easily oxidized with oxygen in the air, generating copper oxide. Under light irradiation, different substances generally have different colors. The color of oxygen free copper is generally purple red, with high color characteristic values such as R, G, B, H, S, and I. Copper oxide is generally black, with lower color characteristic values such as R, G, B, H, S, and I. As the sampling time increases, the wick will eventually change from copper to copper oxide and remain stable, and the color of the wick will gradually darken and turn black. Therefore, as the sampling time increases, all six color features of the wick image will show a significant decrease, indicating that color features are specific manifestations of different degrees of oxidation of the wick.

3.2. Analysis of the capillary performance test results for wicks

The average capillary climb height of wicks obtained every day was calculated, and the variation of capillary climb height of wicks with sampling time was analyzed, the results are shown in Fig. 10. 10.

As shown in Fig. 10, the capillary climb heights of the coarse-powder wick, fine-powder wick, and mixed-powder wick all decrease with increasing sampling time. When the sampling time is the same, the capillary performance from good to poor is as follows: mixed-powder wick > coarse-powder wick > fine-powder wick. At the initial stage, the capillary performance of the coarse-powder wick, fine-powder wick, and mixed-powder wick is optimal, with climbing heights of 96.22 mm, 93.57 mm, and 98.63 mm, respectively. At the end of the sampling, the capillary performance of the three types of wicks is the worst, with climbing heights of 60.36 mm, 58.36 mm, and 70.28 mm, respectively. Through comprehensive analysis, it can be concluded that the capillary climb height of coarse-powder wicks, fine-powder wicks, and mixed-powder wicks is linearly negatively correlated with sampling time. The capillary climb height of wick can directly reflect the quality of wick with different degrees of oxidation.

3.3. Analysis of heat transfer performance of the heat pipes

The heat transfer performance of the heat pipes made every day is analyzed. The changes in the heat source temperature and thermal resistance of the coarse-powder heat pipe, fine-powder heat pipe, and mixed-powder heat pipe with sampling time are shown in Fig. 11.

As shown in Fig. 11, when the power is constant, the heat source temperature and thermal resistance of the coarse-powder heat pipe, fine-powder heat pipe, and mixed-powder heat pipe increase with increasing sampling time. At the initial moment, the heat source temperature and thermal resistance reach their minimum values, and at the termination moment, they reach their maximum values. To investigate the reasons, when the power is constant, as the sampling time increases, the wicks inside the coarse-powder heat pipe, fine-powder heat pipe, and mixed-powder heat pipe will undergo oxidation reactions with air, resulting in changes in the surface material of the wick, producing substances such as copper, cuprous oxide, or cuprous oxide. Given that copper is hydrophilic and cuprous oxide is hydrophobic, when the wick undergoes oxidation, its hydrophilicity and hydrophobicity will change, leading to a decrease in capillary pressure and a gradual decline in the performance of the heat pipe. When the sampling time is constant, the heat source temperatures of the coarse-powder heat pipe, fine-powder heat pipe, and mixed-powder heat pipe all increase with increasing heating power, and the thermal resistance initially decreases and then increases with

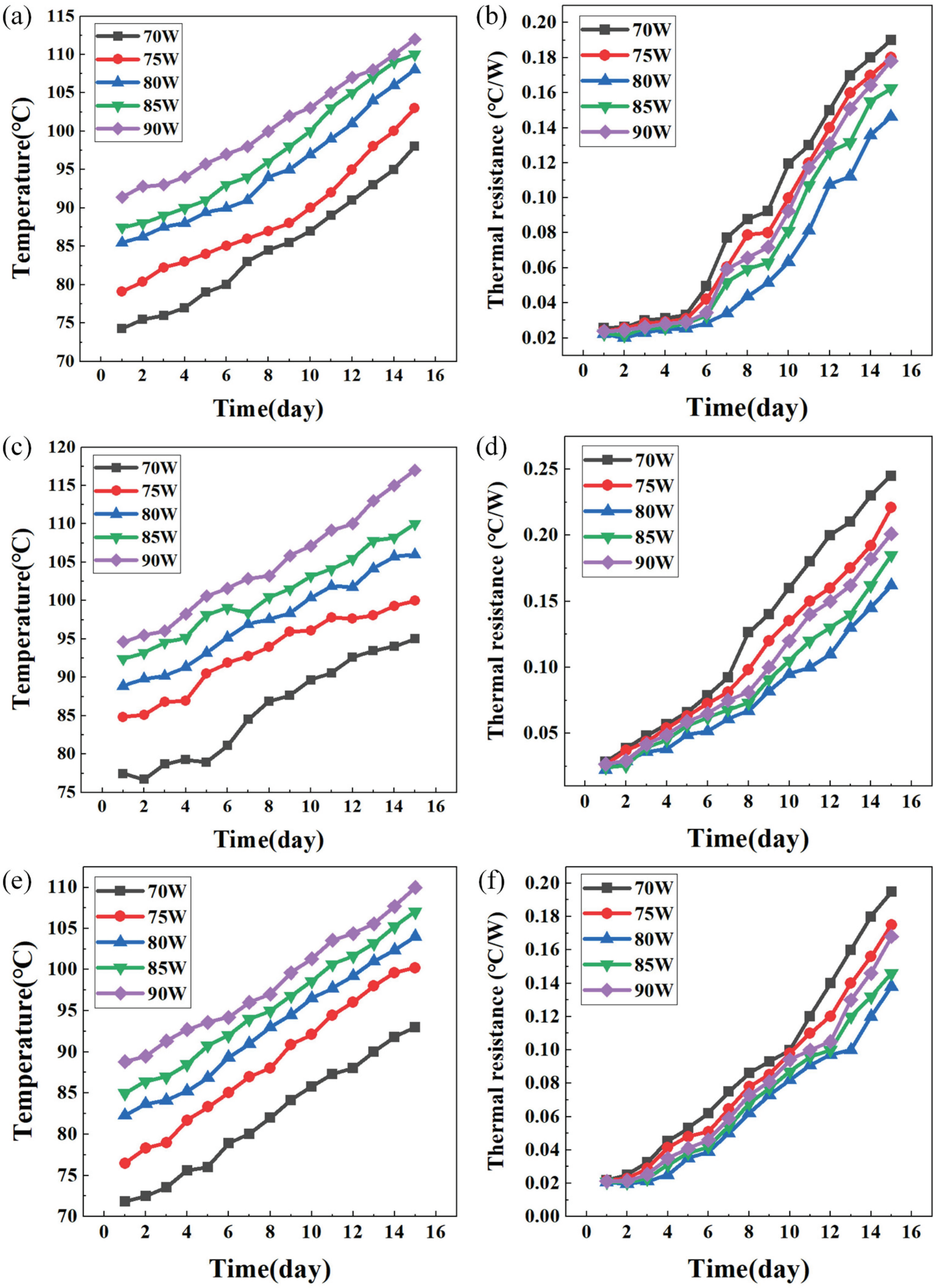

Fig. 11. Variation in the heat transfer performance of the heat pipes with sampling time: (a) the heat source temperature of the coarse-powder heat pipes, (b) the thermal resistance of the coarse-powder heat pipes, (c) the heat source temperature of the fine-powder heat pipes, (d) the thermal resistance of the fine-powder heat pipes, (e) the heat source temperature of the mixed-powder heat pipes, and (f) the thermal resistance of the mixed-powder heat pipes.

Table 4
Oxidation grading standards for wicks.

Temperature difference ΔT	Classification level
$0^{\circ} \leq \Delta T < 2^{\circ}$	1
$2^{\circ} \leq \Delta T < 3^{\circ}$	2
$3^{\circ} \leq \Delta T < 5^{\circ}$	3
$\Delta T \geq 5^{\circ}$	4

Table 5
Sample quantity of wick.

	Number of samples			
	Level 1	Level 2	Level 3	Level 4
Coarse-powder wick	200	200	200	200
Fine-powder wick	200	200	200	200
Mixed-powder wick	200	200	200	200

increasing heating power. The average temperature of the heat source is the lowest at 70 W, and the average temperature of the heat source is the highest at 90 W. At 80 W, the thermal resistance reaches its minimum value, and the performance of the heat pipe reaches its optimal level. To investigate the reasons, when the power is constant, as the power increases, the heat flux density of the coarse-powder heat pipe, fine-

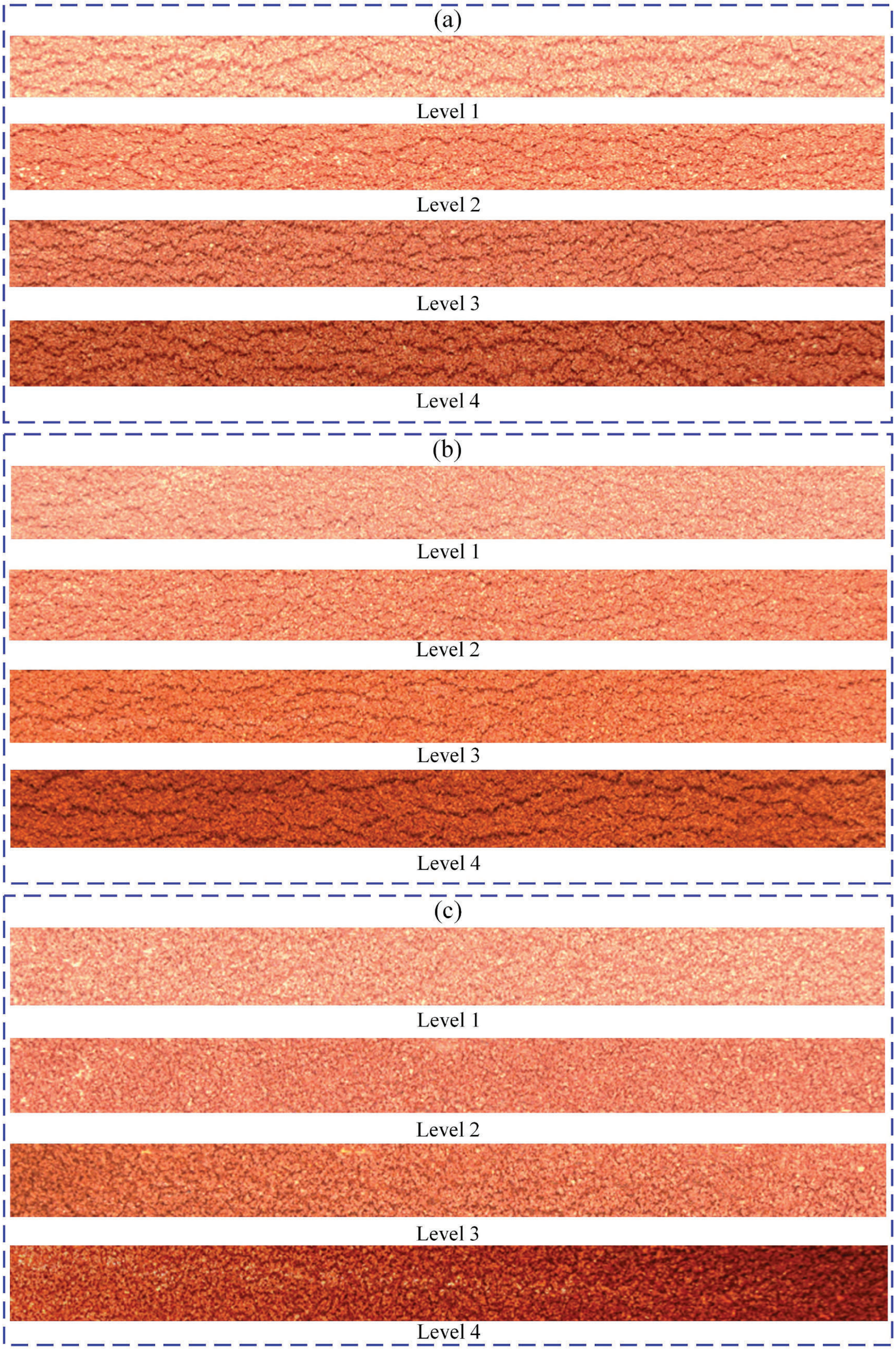

Fig. 12. Wick image dataset: (a) coarse-powder wick image dataset, (b) fine-powder wick image dataset, and (c) mixed-powder wick image dataset.

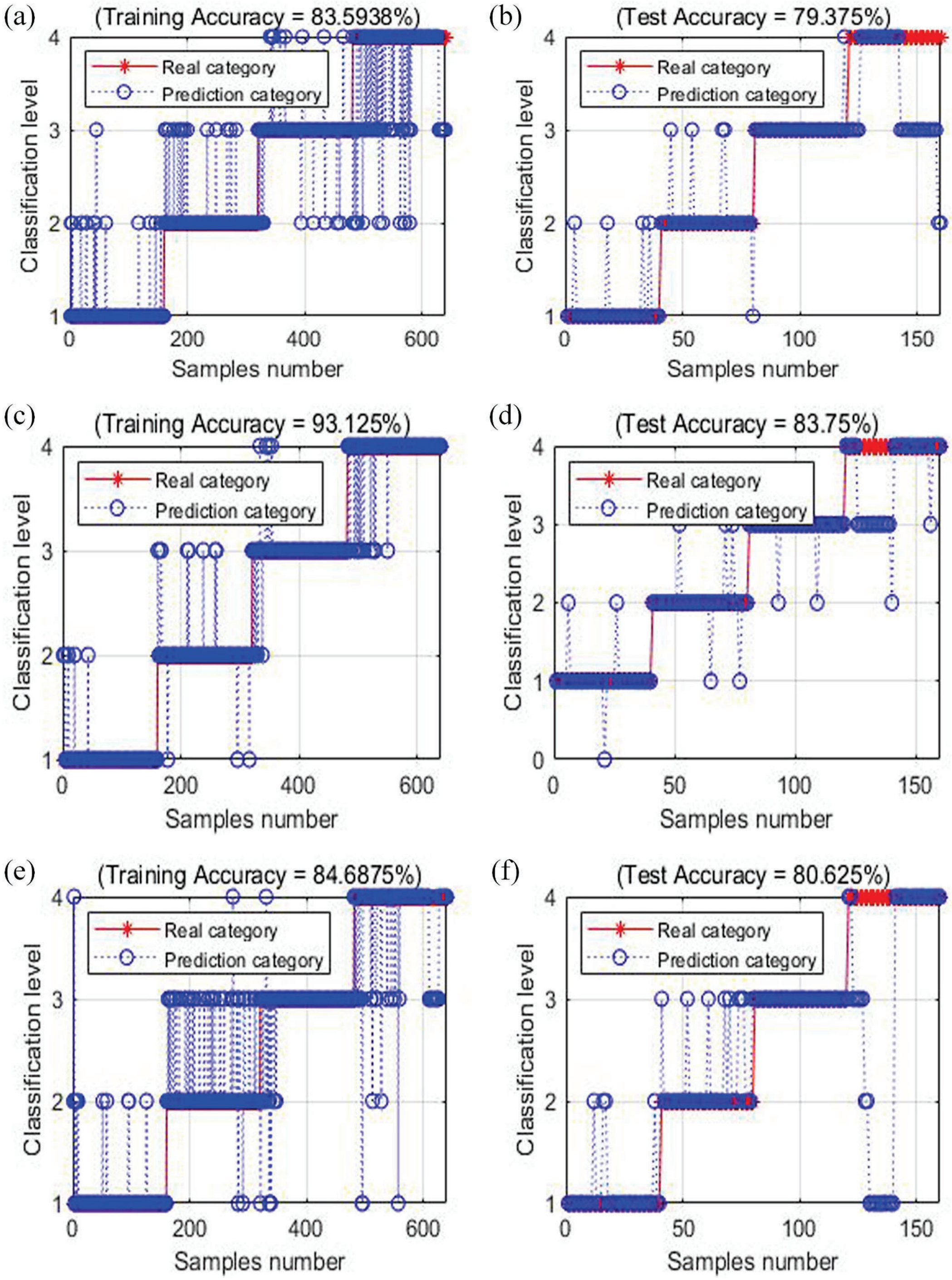

Fig. 13. BP neural network grading results: (a) grading accuracy of the coarse-powder wick training set, (b) grading accuracy of the coarse-powder wick test set, (c) grading accuracy of the fine-powder wick training set, (d) grading accuracy of the fine-powder wick test set, (e) grading accuracy of the mixed-powder wick training set, and (f) grading accuracy of the mixed-powder wick test set.

powder heat pipe, and mixed-powder heat pipe gradually increases, and the steam temperature gradually increases. When the heat dissipation conditions are constant, the heat source temperature of the heat pipe gradually increases. Under the same testing conditions, thermal resistance is generally related to water volume. At low power, the working fluid inside the tube cannot evaporate completely, and liquid will accumulate at the bottom of the wick, resulting in a higher thermal resistance. At high power, due to the rapid evaporation of the working fluid, it is not possible for the working fluid to reflux back to the evaporator, resulting in a sharp increase in the thermal resistance of evaporation and an increase in the total thermal resistance. Therefore, when the water volume is constant, the thermal resistance generally decreases first and then increases with the increase of power. Under the same conditions, the performance of heat pipes from good to poor is as follows: mixed-powder heat pipe > coarse-powder heat pipe > fine-powder heat pipe. To investigate the reasons, when coarse-powder, fine-powder, and mixed-powder are simultaneously sintered into a wick structure, the permeability of the coarse-powder wick is high with low capillary force, while the permeability of the fine-powder wick is low with high capillary pressure. The wick of the mixed-powder combines

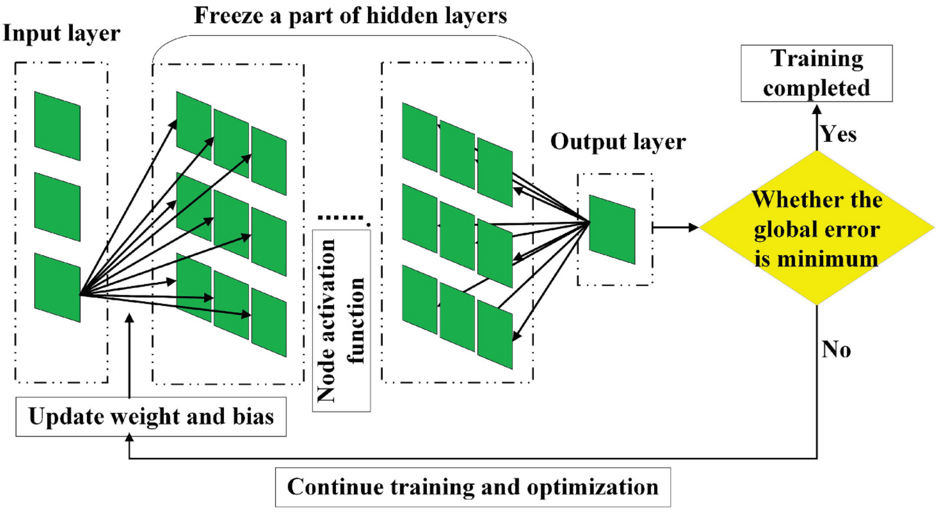

Fig. 14. Schematic diagram of the transfer learning model framework.

Table 6
Model hyperparameters after migration.

Transfer model	Input	Number of hidden layers	Number of nodes (number of channels/fully connected layer)	Output dense
VGG16 [51]	[(None, 300, 300, 3)]	16	64 → 512/4096 → 4096	(None, 4)
VGG19 [51]		19	64 → 512 / 4096 → 4096	
Xception [52]		71	64 → 2048	
ResNet50 [53]		50	64 → 2048	
InceptionV3 [54]		48	32 → 2048	
InceptionResNetV2 [55]		164	32 → 1536	
DenseNet121 [56]		121	64 → 1024	

the advantages of both coarse-powder wicks and fine-powder wicks, with good capillary force and permeability. Therefore, the performance of the mixed-powder heat pipe is optimal. Comprehensive analysis shows that the performance of coarse-powder heat pipes, fine-powder heat pipes, and mixed-powder heat pipes is negatively correlated with sampling time. That is, the longer the sampling time, the more severe the oxidation degree of the wick, and the worse the performance of the heat pipe. Therefore, the performance of the heat pipe can indirectly reflect the quality of the wick with different degrees of oxidation.

3.4. Selection of the oxidation grading index and determination of grading standards for wicks

The oxidation of the wick significantly affects the performance of the heat pipe. To ensure the performance of the heat pipe, the quality of the wick of the annealed semifinished heat pipe needs to be tested and graded, and the number of wicks with more severe oxidation needs to be limited moving forward to the next process. Therefore, selecting appropriate wick oxidation grading indicators and determining grading standards are crucial. Previous studies have shown that the colour characteristics of wick images can intuitively reflect the severity of wick oxidation; therefore, image features are specific manifestations of the wick oxidation and are not suitable as grading indicators. The capillary climb height and heat transfer performance of the heat pipe both have the ability to reflect the quality of the wick with different degrees of oxidation. However, in actual production, the wick is a necessary rather than sufficient condition to ensure the performance of the heat pipe. Obtaining high-performance heat pipes is the ultimate goal. Therefore, using heat pipe performance as a separate indicator is more reasonable and in line with reality. The characterization indicators of the heat transfer performance of heat pipes mainly include the heat source temperature, temperature difference, and thermal resistance; among these, the thermal resistance is the comprehensive indicator of the quality of heat pipes. Research has shown that the heat pipe used in this experiment had the lowest thermal resistance at 80 W, and the heat pipe performance reached its optimum. Therefore, in this study, the thermal resistance of the heat pipe at 80 W was selected as the grading index for the oxidation level of the wick. For the convenience of the experiment, the thermal resistance was converted into a temperature difference ΔT (the difference in temperature between the evaporation end and the condensation end of heat pipe). Based on the actual production, the standard for the oxidation grading of the wick was determined according to the temperature difference range, as shown in Table 4.

Based on the above standards, according to the range of the average temperature difference of the heat pipes manufactured every day, the wick grade was calibrated at the same sampling time, and image datasets were established for the different types of wicks with different oxidation levels. The detailed number of wick samples is provided in Table 5, and the wick images with different levels are shown in Fig. 12.

3.5. Analysis of the BP neural network model grading results

In this study, a BP neural network model is used to perform oxidation classification on the wicks. Six colour feature values (R, G, B, H, S, I) of three different types of wicks are used as input features, and oxidation levels are used as output results to establish an oxidation classification model. The model consists of one input layer, three hidden layers, and one output layer. The number of input layer nodes is 6, the number of nodes in the three hidden layers is 4, 16, and 16, respectively, and the number of output layer nodes is 1. The network target error is set to 0.01, the learning rate is 0.005, and the number of network iterations is 1000 epochs. The model was trained and tested using 75 % of the sample data of each wick type as the training set and 25 % as the validation set. The model grading results are shown in Fig. 13.

According to Fig. 13, the classification accuracies of the coarse-powder wick, fine-powder wick, and mixed-powder wick methods on the training set are 83.59 %, 93.12 %, and 84.68 %, respectively. The accuracies on the test set are 79.37 %, 83.75 %, and 80.62 %, respectively. The classification accuracy of the model for different types of wicks, from high to low, is as follows: fine-powder wick, mixed-powder wick, and coarse-powder wick. Overall, using colour features as inputs for the oxidation grading of wicks is feasible, and the average grading

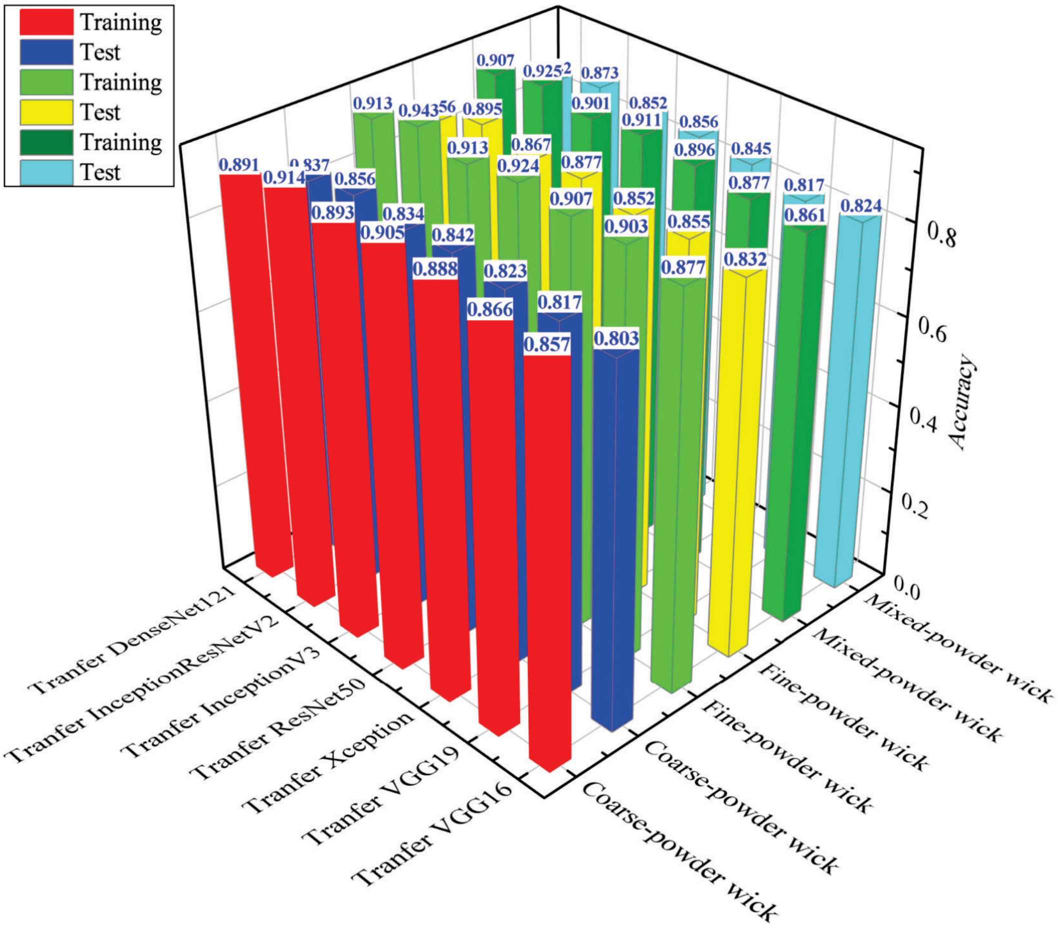

Fig. 15. Grading results of the transfer learning models.

accuracy is 80 %. However, for actual production, the classification accuracy of this model still needs to be improved.

3.6. Analysis of the grading results of the transfer learning models

In this study, the architecture and weights of existing models are transferred, the wick images are used as inputs, and a convolution operation is used to extract the image features and achieve wick oxidation grading. The basic framework of the model [50] is shown in Fig. 14, and the hyperparameters of each model after transfer are listed in Table 6. The input image size is set to 300 × 300 × 3, with 1000 network iterations. The model was trained and tested using 75 % of the sample data of each wick type as the training set and 25 % as the validation set. The model grading results are shown in Fig. 15.

As shown in Fig. 15, the average grading accuracy of the transfer learning models for different types of wicks reaches approximately 85 %. Among many models, the Transfer InceptionResNetV2 model has the best grading effect, with oxidation grading accuracies of 85 %, 89 %, and 87 % for different types of wicks. Compared with the grading results of the BP network models, the overall grading accuracy of the transfer learning models is greater. The results indicate that the transfer learning model can use images as inputs and can extract the image features using convolution to perform oxidation grading on wicks. Convolutional kernels can extract more advanced features in addition to colour features, and compared with oxidation grading models that rely solely on colour features, transfer learning models have higher accuracy.

3.7. Analysis of the grading results for the improved and optimized model

To further improve the accuracy of grading, it is necessary to improve and optimize the model. The basic structure of the improved and optimized model is as follows: using color features and wick images as inputs, the InceptionResNetV2 model with good grading performance is selected and combined with attention mechanism. Channel attention mechanism is added after the stem layer, spatial attention mechanism is added after the Reduction-A layer, and mixed attention mechanism is added after the Reduction-B layer. The attention mechanism guides the model to focus on representative features, improving the accuracy of model grading. The basic composition of the improved and optimized model is shown in Fig. 16, and the detailed structure of the improved InceptionResNetV2 model is shown in Fig. 17. The convolutional layers of the improved and optimized model are activated using Relu, the output layer is activated using SoftMax, and the loss function is calculated using the sparse_category_crossentropy function. The model is optimized using the Adam algorithm, and overfitting is suppressed using droupt with a value of 0.2. The calculation methods for each activation function, loss function, and Adam algorithm update weight process are the same as before. The input image size is set to 300 × 300 × 3, with 1000 network iterations. The model is trained and tested using 75 % of the sample data from various types of wicks as the training set and 25 % as the validation set. The model grading results are shown in Fig. 18.

As shown in Fig. 18, the overall accuracy of the coarse-powder wick, fine-powder wick, and mixed-powder wick on the training and testing sets of the improved and optimized model has reaches over 92 %, with the highest reaching over 97 % and 95 % for the training and testing sets, respectively. Compared with the BP neural network model and the

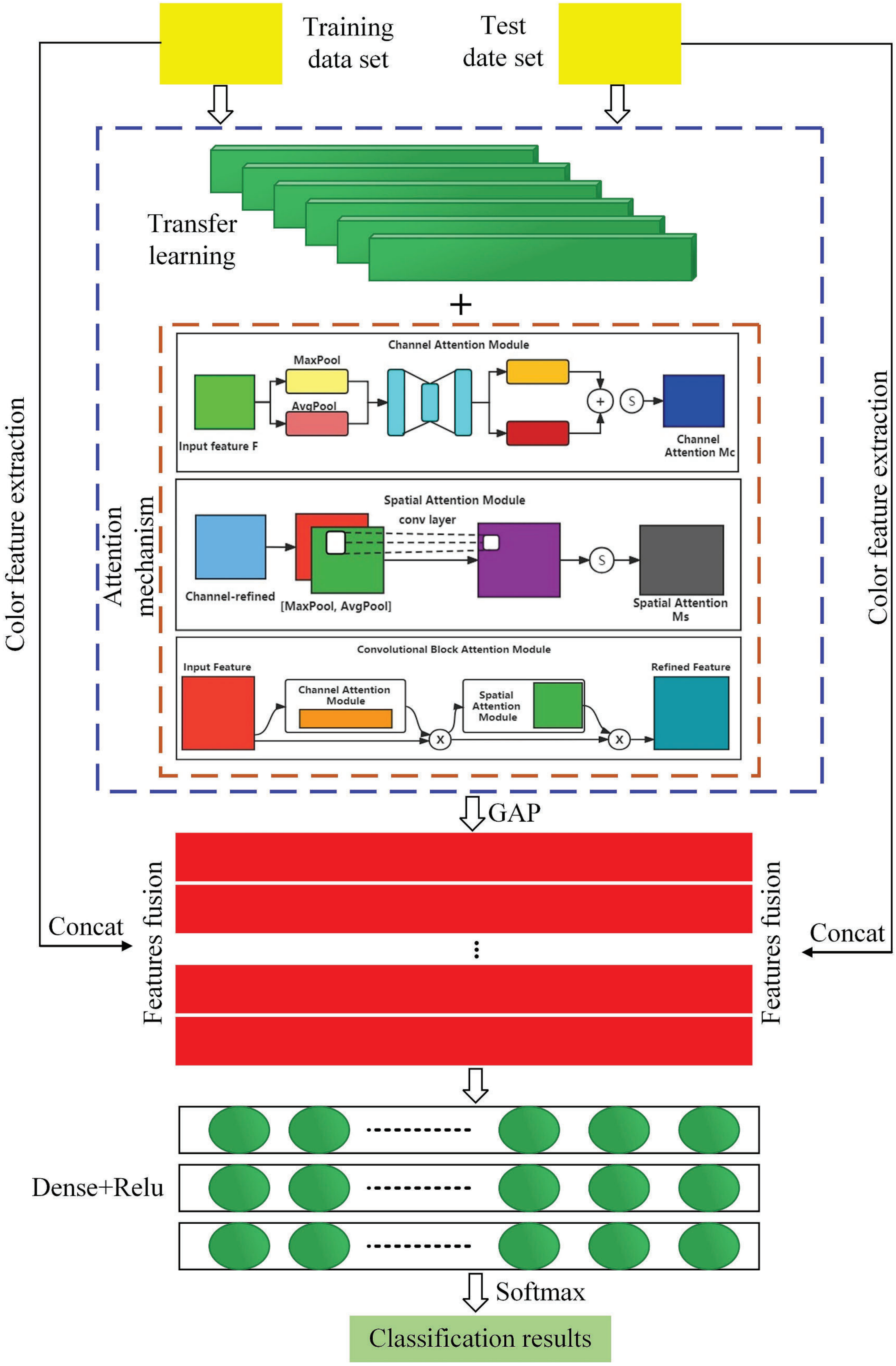

Fig. 16. Schematic diagram of the composition of the improved and optimized model.

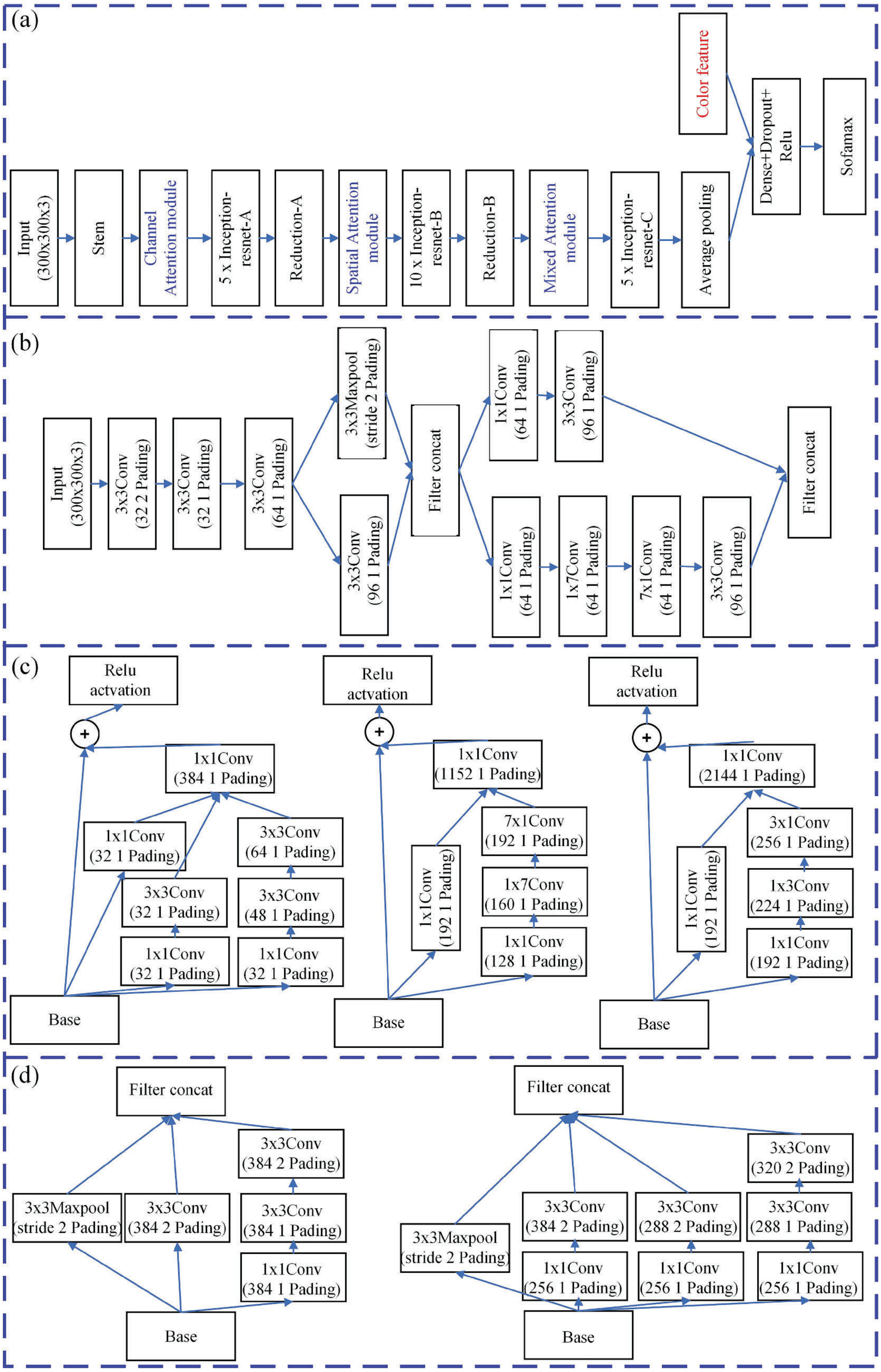

Fig. 17. Detailed structure of the improved model.

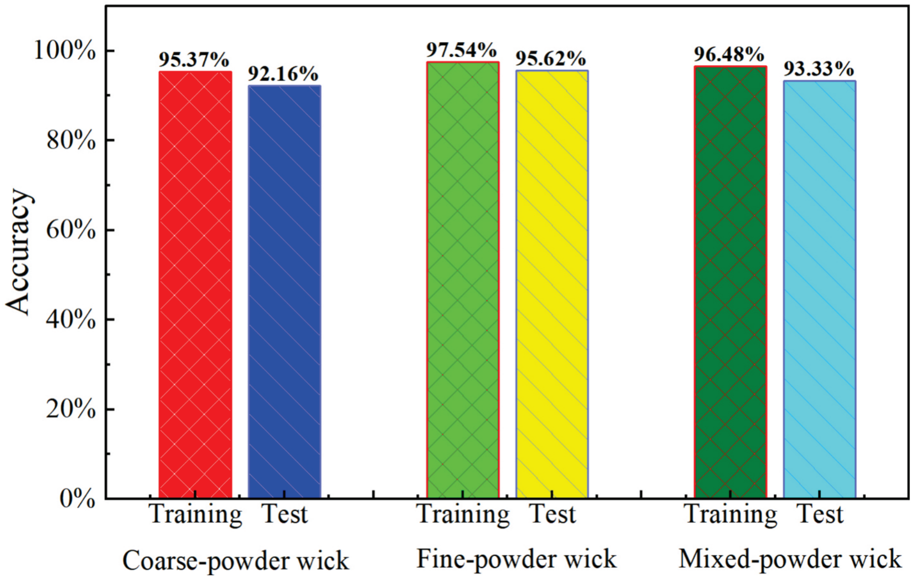

Fig. 18. Grading results of the improved and optimized models.

transfer learning model, the improved and optimized model has the best performance. The results indicate that using the colour features and wick images as inputs, extracting image features through convolutional kernels, and concatenating colour features with image features can provide a richer and larger feature set for the model. Moreover, due to the introduction of attention mechanisms, the model focuses more on the representative features, and the classification accuracy of the model is greatly improved. The model was packaged and used on the production line of the heat pipe. Production data showed that the actual prediction error of the model was about 8 %. Compared with the discrimination error relying on manual detection in the past, the prediction error of the model was smaller, which can meet the current needs of actual production.

4. Conclusions

As the core component of a heat pipe, the oxidation of the wick directly affects the performance of the heat pipe. The focus of this study is on the classification and detection of oxidation for heat pipe wicks in actual production. The relationships among the colour characteristics of the wick, capillary climb height of the wick, heat transfer performance of the formed heat pipe, and degree of oxidation of the wick were analysed through various experiments. The thermal resistance was selected as the index for the oxidation grade of the wick, and an oxidation grade standard for the wick was established. Oxidation detection and classification of wicks were attained using machine learning methods. The main conclusions are as follows:

(1) The colour characteristics and capillary climb height of the wick and the heat transfer performance of the heat pipe vary with the degree of oxidation of the wick, and these factors can be used to characterize the degree of oxidation of the wick. Among them, the colour characteristics and capillary climb height of the wick decrease with increasing degree of wick oxidation, whereas the heat source temperature and thermal resistance of the heat pipe increase with increasing wick oxidation degree.

(2) Using the colour characteristics and images of the wick separately as inputs for the model can achieve oxidation grading of the wick. The average grading accuracies using the colour characteristics and images reach over 80 % and 85 %, respectively. Compared with models that rely on colour features for oxidation grading, models that use images as input and extract image features through convolution for oxidation grading of wicks can extract more advanced features in addition to colour features; this results in higher grading accuracy of the model.

(3) Using the colour features of the wick and the image together as inputs for the model, image features are extracted through convolutional kernels, and the colour features are concatenated with the image features. Moreover, an attention mechanism is introduced into the model and can greatly improve the classification accuracy of the model. Here, the colour characteristics of the wick and the images are used as the model inputs, and the attention mechanism is combined with the model. The overall classification accuracy of the improved and optimized model has reaches over 92 %, with the highest reaching over 97 % and 95 % for the training and testing sets, respectively. Thus, high-precision oxidation classification of the wick is attained, the accuracy of this model can meet the actual production needs.

Declaration of competing interest

The authors declare that they have no known competing financial interests or personal relationships that could have appeared to influence the work reported in this paper.

Acknowledgements

This research was supported by the Natural Science Foundation of Guangdong Province (Grant No. 2023A1515011635, 2022A1515110724), the Key Research and Development Plan of Guangxi Province (Grant No. 2024AB08167), the National Natural Science Foundation of China (Grant No. 52305258), and the Project of the Guangzhou Science and Technology Plan (Grant No. 2024A04J4133). Thanks for Guangdong Newidea Technology Co., Ltd. (http://www.863cn.com) providing a valuable platform for the design, manufacture and performance testing of heat pipes in this research.

Data availability

Data will be made available on request.

References

[1] R. Zhong, W. Feng, Y. Ma, J. Deng, Y. Liu, S. Ding, X. Wang, Y. Liang, G. Yang, Experimental study of heat pipe start-up characteristics and development of an enhanced model considering gas diffusion effects, Appl. Therm. Eng. 257 (2024) 124460, https://doi.org/10.1016/j.applthermaleng.2024.124460.

[2] Y. Li, Z. Li, C. Chen, Y. Yan, Z. Zeng, B. Li, Thermal responses of heat pipes with different wick structures under variable centrifugal accelerations, Appl. Therm. Eng. 96 (2016) 352–363, https://doi.org/10.1016/j.applthermaleng.2015.11.016.

[3] J. Yu, Y. Li, Z. Xin, Z. Chen, L. Deng, X. Guo, H. Chen, H. He, Experimental investigation on the thermal characteristics of ultrathin vapour chamber with in-plane bending, Appl. Therm. Eng. 217 (2022) 119175, https://doi.org/10.1016/j.applthermaleng.2022.119175.

[4] A. Kumar, S. Singh, R. Kumar, A.K. Das, Evaluation of thermo-fluidic performance of micro pulsating heat pipe with and without evaporator side surface structures, Appl. Therm. Eng. 249 (2024) 123470, https://doi.org/10.1016/j.applthermaleng.2024.123470.

[5] Y. Li, W. Zhou, J. He, Y. Yan, B. Li, Z. Zeng, Thermal performance of ultra-thin flattened heat pipes with composite wick structure, Appl. Therm. Eng. 102 (2016) 487–499, https://doi.org/10.1016/j.applthermaleng.2016.03.097.

[6] J. Yu, Y. Li, Z. Chen, Q. Luo, H. Chen, X. Tang, Effect of the passage area ratio of wick on an ultra-thin vapour chamber with a spiral woven mesh wick, Appl. Therm. Eng. 196 (2021) 117282, https://doi.org/10.1016/j.applthermaleng.2021.117282.

[7] Y. Lu, R. Xiong, Y. Tang, N. Yu, X. Nie, L. Zhang, X. Meng, An overview of the detection methods to the edible oil oxidation degree: Recent progress, challenges, and perspectives, Food Chem. 463 (2025) 141443, https://doi.org/10.1016/j.foodchem.2024.141443.

[8] D.E. Wilcox, Isothermal titration calorimetry of metal ions binding to proteins: an overview of recent studies, Inorganica Chim. Acta 361 (4) (2008) 857–867, https://doi.org/10.1016/j.ica.2007.10.032.

[9] J.L. Tay, Z. Li, C. Xu, Z. Zhou, A systematic review of the safety and efficacy of rapid titration of quetiapine running header: rapid titration of Quetiapine- A systematic review, Psychiatry Res. 281 (2019) 112557, https://doi.org/10.1016/j.psychres.2019.112557.

[10] I.D. Lima Cavalcanti, F.H. Xavier Junior, N.S. Santos Magalhães, M.C.D.B. Lira Nogueira, Isothermal titration calorimetry (ITC) as a promising tool in pharmaceutical nanotechnology, Int. J. Pharm. 641 (2023) 123063, https://doi.org/10.1016/j.ijpharm.2023.123063.

[11] N. Zhang, Y. Li, S. Wen, Y. Sun, J. Chen, Y. Gao, Analytical methods for determining the peroxide value of edible oils: a mini-review, Food Chem. 358 (2021) 129834, https://doi.org/10.1016/j.foodchem.2021.129834.

[12] J. Chen, D. Cai, Y. Zhang, Rapid determination of lipid peroxidation using a novel pyridoxamine-participating ferrous oxidation-sulfosalicylic acid spectrophotometric method, Food Chem. 211 (2016) 637–644, https://doi.org/10.1016/j.foodchem.2016.05.106.

[13] P. Avramidis, K. Nikolaou, V. Bekiari, Total Organic Carbon and Total nitrogen in sediments and soils: a comparison of the wet oxidation-titration method with the combustion-infrared method, Agric. Agric. Sci. Procedia 4 (2015) 425–430, https://doi.org/10.1016/j.aaspro.2015.03.048.

[14] A. Cafaro, S. Barco, F. Pigliasco, C. Russo, M. Mariani, A. Mesini, C. Saffioti, E. Castagnola, G. Cangemi, Therapeutic drug monitoring of glycopeptide antimicrobials: an overview of liquid chromatography-tandem mass spectrometry methods, J. Mass Spectrom. Adv. Clin. Lab (2023), https://doi.org/10.1016/j.jmsacl.2023.12.003.

[15] L. Chen, B. Dean, X. Liang, A technical overview of supercritical fluid chromatography-mass spectrometry (SFC-MS) and its recent applications in pharmaceutical research and development, Drug Discov. Today Technol. 40 (2021) 69–75, https://doi.org/10.1016/j.ddtec.2021.10.002.

[16] T.M. Gröger, U. Käfer, R. Zimmermann, Gas chromatography in combination with fast high-resolution time-of-flight mass spectrometry: technical overview and perspectives for data visualization, TrAC Trends Anal. Chem. 122 (2020) 115677, https://doi.org/10.1016/j.trac.2019.115677.

[17] M. Jalali-Heravi, H. Parastar, H. Sereshti, Towards obtaining more information from gas chromatography-mass spectrometric data of essential oils: an overview of mean field independent component analysis, J. Chromatogr. A 1217 (29) (2010) 4850–4861, https://doi.org/10.1016/j.chroma.2010.05.026.

[18] L. Zhang, J. Chen, X. Zhao, Y. Wang, X. Yu, Influence of roasting on the thermal degradation pathway in the glucosinolates of fragrant rapeseed oil: Implications to flavour profiles, Food Chem.: X 16 (2022) 100503, https://doi.org/10.1016/j.fochx.2022.100503.

[19] Y. Li, M. Driver, E. Decker, L. He, Lipid and lipid oxidation analysis using surface enhanced Raman spectroscopy (SERS) coupled with silver dendrites, Food Res. Int. 58 (2014) 1–6, https://doi.org/10.1016/j.foodres.2014.01.056.

[20] J.A. Custodio-Mendoza, J. Aja-Macaya, I.M. Valente, J.A. Rodrigues, P.J. Almeida, R.A. Lorenzo, A.M. Carro, Determination of malondialdehyde, acrolein and four other products of lipid peroxidation in edible oils by Gas-Diffusion Microextraction combined with Dispersive liquid-liquid Microextraction, J. Chromatogr. A 1627 (2020) 461397, https://doi.org/10.1016/j.chroma.2020.461397.

[21] C.A. Whitman, J.T.O. Flynn, A.J. Rayner, S.F. Corbin, Determining the oxidation behavior of metal powders during heating through thermogravimetric and evolved gas analysis using a coupled thermogravimetry-gas chromatography-mass spectrometry technique, Thermochim. Acta 638 (2016) 124–137, https://doi.org/10.1016/j.tca.2016.06.019.

[22] V. Alampanos, V. Samanidou, An overview of sample preparation approaches prior to liquid chromatography methods for the determination of parabens in biological matrices, Microchem J. 164 (2021) 105995, https://doi.org/10.1016/j.microc.2021.105995.

[23] B.P. Vempatapu, J. Kumar, B. Upreti, P.K. Kanaujia, Application of high-performance liquid chromatography in petroleum analysis: Challenges and opportunities, TrAC Trends Anal. Chem. 177 (2024) 117810, https://doi.org/10.1016/j.trac.2024.117810.

[24] J. Velasco, A. Morales-Barroso, M.V. Ruiz-Méndez, G. Márquez-Ruiz, Quantitative determination of major oxidation products in edible oils by direct NP-HPLC-DAD analysis, J. Chromatogr. A 1547 (2018) 62–70, https://doi.org/10.1016/j.chroma.2018.03.014.

[25] D.F. Barbin, A.L.D.S. Felicio, D. Sun, S.L. Nixdorf, E.Y. Hirooka, Application of infrared spectral techniques on quality and compositional attributes of coffee: an overview, Food Res. Int. 61 (2014) 23–32, https://doi.org/10.1016/j.foodres.2014.01.005.

[26] N. Luo, D. Xu, B. Xing, X. Yang, C. Sun, Principles and applications of convolutional neural network for spectral analysis in food quality evaluation: a review, J. Food Compos. Anal. 128 (2024) 105996, https://doi.org/10.1016/j.jfca.2024.105996.

[27] M.M. Abd-Elhady, M.A. Elhendawy, M.S. Abd-Elmajeed, R.B. Rizk, Enhancing photovoltaic systems: A comprehensive review of cooling, concentration, spectral splitting, and tracking techniques, Next Energy 6 (2025) 100185, https://doi.org/10.1016/j.nxener.2024.100185.

[28] Y.A. Eltbaakh, M.H. Ruslan, M.A. Alghoul, M.Y. Othman, K. Sopian, M.I. Fadhel, Measurement of total and spectral solar irradiance: overview of existing research, Renew. Sustain. Energy Rev. 15 (3) (2011) 1403–1426, https://doi.org/10.1016/j.rser.2010.10.018.

[29] R. Zhu, J. Gao, Q. Tian, M. Li, Q. Gao, X. Wu, S. Xu, Y. Zhang, Optical chemical gas sensor based on spectral autocorrelation: A method for online detection of nitric oxide and ammonia in exhaled breath, Sens. Actuators B 422 (2025) 136694, https://doi.org/10.1016/j.snb.2024.136694.

[30] L. Yao, Z. Fu, Q. Duan, M. Wu, F. Song, H. Wang, Y. Qin, Y. Bai, C. Zhou, X. Quan, J. Lee, An intelligent spectral identification approach for the simultaneous detection of endocrine-disrupting chemicals in aquatic environments, Journal Pre-Proof (2024), https://doi.org/10.1016/j.envres.2024.120368.

[31] F. Xiang, Y. He, S. Kumar, Z. Wang, L. Liu, Z. Huang, J. Liu, K. Cen, Influence of hydrothermal dewatering on trace element transfer in Yimin coal, Appl. Therm. Eng. 117 (2017) 675–681, https://doi.org/10.1016/j.envres.2024.120368.

[32] H. Zhang, Z. Wang, S. Li, Y. Jiao, J. Wang, Q. Zhu, X. Li, Correlation between structure, acidity and activity of Mo-promoted Pt/ZrO2-TiO2-Al2O3 catalysts for n-decane catalytic cracking, Appl. Therm. Eng. 111 (2017) 811–818, https://doi.org/10.1016/j.envres.2024.120368.

[33] C. Cardell, I. Guerra, An overview of emerging hyphenated SEM-EDX and Raman spectroscopy systems: applications in life, environmental and materials sciences, TrAC Trends Anal. Chem. 77 (2016) 156–166, https://doi.org/10.1016/j.trac.2015.12.001.

[34] P. Wang, W. Gu, L. Lei, Y. Cai, Z. Li, Micro-structural and components evolution mechanism of particular matter from diesel engines with non-thermal plasma technology, Appl. Therm. Eng. 91 (2015) 1–10, https://doi.org/10.1016/j.applthermaleng.2015.08.010.

[35] U. Meissner, A.G. Martin, B. Schwarz, M. Stohr, W. Gebauer, J.R. Harris, J. Markl, 3-D reconstruction of hemocyanins and other invertebrate hemolymph proteins by cryo-TEM: an overview, Micron 35 (2004) 7–9, https://doi.org/10.1016/j.micron.2003.10.003.

[36] E. Yildirim, E. Jimenez-Melero, B. Dacus, C. Dennett, K.B. Woller, M. Short, P. M. Mummery, Elucidating the thermal response of W-Ta alloys with Transient Grating Spectroscopy, TEM and atomistic simulation, Fusion Eng. Des. 208 (2024) 114676, https://doi.org/10.1016/j.fusengdes.2024.114676.

[37] W. Zhou, Y. Li, Z. Chen, L. Deng, Y. Gan, Ultra-thin flattened heat pipe with a novel band-shape spiral woven mesh wick for cooling smartphones, Int. J. Heat Mass Transf. 146 (2020) 118792, https://doi.org/10.1016/j.ijheatmasstransfer.2019.118792.

[38] W. Zhou, Y. Li, Z. Chen, L. Deng, Y. Gan, A novel ultra-thin flattened heat pipe with biporous spiral woven mesh wick for cooling electronic devices, Energy Conv. Manag. 180 (2019) 769–783, https://doi.org/10.1016/j.enconman.2018.11.031.

[39] W. Zhou, Y. Li, Z. Chen, L. Deng, Y. Gan, Effect of the passage area ratio of liquid to vapor on an ultra-thin flattened heat pipe, Appl. Therm. Eng. 162 (2019) 114215, https://doi.org/10.1016/j.applthermaleng.2019.114215.

[40] X. Guo, Y. Li, W. Zhou, R. Tang, Y. Tian, A. Gao, Y. Yang, Experimental study on the failure mechanism of the heat transfer performance under the action of oxygen of a copper–water vapour chamber without structural damage, Appl. Therm. Eng. (2025), https://doi.org/10.1016/j.applthermaleng.2025.125619.

[41] H. Alshannaq, A.M. Aly, Review of Artificial Neural Networks for Wind Turbine Fatigue Prediction, Structural Durability & Health Monitoring 18 (6) (2024) 707-737. 10.32604/sdhm.2024.054731.

[42] S. Huang, R. Wei, L. Lian, S. Lo, S. Lu, Review of the application of neural network approaches in pedestrian dynamics studies, Heliyon 10 (10) (2024), https://doi.org/10.1016/j.heliyon.2024.e30659.

[43] M. Soori, B. Arezoo, R. Dastres, Artificial neural networks in supply chain management, a review, Journal of Economy and Technology 1 (2023) 179–196, https://doi.org/10.1016/j.ject.2023.11.002.

[44] M. Hakim, A.A.B. Omran, A.N. Ahmed, M. Al-Waily, A. Abdellatif, A systematic review of rolling bearing fault diagnoses based on deep learning and transfer learning: Taxonomy, overview, application, open challenges, weaknesses and recommendations, Ain Shams Eng. J. 14 (4) (2023) 101945, https://doi.org/10.1016/j.asej.2022.101945.

[45] Z. Zhang, Y. Wang, X. Ruan, X. Zhang, A federated transfer learning approach for lithium-ion battery lifespan early prediction considering privacy preservation, J. Energy Storage 102 (2024) 114153, https://doi.org/10.1016/j.est.2024.114153.

[46] G. Zhu, S. Liu, D. Zhang, W. Chen, J. Li, T. Wen, Transfer learning model to predict flow boiling heat transfer coefficient in mini channels with micro pin fins, Int. J. Heat Mass Transf. 220 (2024) 125020, https://doi.org/10.1016/j.ijheatmasstransfer.2023.125020.

[47] K. Hu, K. Xu, Q. Xia, M. Li, Z. Song, L. Song, N. Sun, An overview: Attention mechanisms in multi-agent reinforcement learning, Neurocomputing 598 (2024) 128015, https://doi.org/10.1016/j.neucom.2024.128015.

[48] B. Hu, J. Liu, Y. Xu, A novel multi-scale convolutional neural network incorporating multiple attention mechanisms for bearing fault diagnosis, Measurement 242 (2025) 115927, https://doi.org/10.1016/j.measurement.2024.115927.

[49] X. Dong, L. Zhang, C. Xu, Q. Miao, J. Yao, F. Liu, H. Liu, Y. Lu, R. Kang, B. Song, Detection of pine wilt disease infected pine trees using YOLOv5 optimized by attention mechanisms and loss functions, Ecol. Indic. 168 (2024) 112764, https://doi.org/10.1016/j.ecolind.2024.112764.

[50] K. Kim, H. Lee, M. Kang, G. Lee, K. Jung, C.R. Kharangate, M. Asheghi, K. E. Goodson, H. Lee, A machine learning approach for predicting heat transfer characteristics in micro-pin fin heat sinks, Int. J. Heat Mass Transf. 194 (2022) 123087, https://doi.org/10.1016/j.ijheatmasstransfer.2022.123087.

[51] K. Simonyan, A. Zisserman, Very deep convolutional networks for large-scale image recognition, ICLR (2015) https://arxiv.org/abs/1409.1556.

[52] F. Chollet, Xception: deep learning with depthwise separable convolutions, CVPR (2017) https://arxiv.org/abs/1610.02357.

[53] K. He, X. Zhang, S. Ren, J. Sun, Deep residual learning for image recognition, CVPR (2016) https://arxiv.org/abs/1512.03385.

[54] C. Szegedy, V. Vanhoucke, S. Ioffe, J. Shlens, Z. Wojna, Rethinking the inception architecture for computer vision, CVPR (2016) https://arxiv.org/abs/1512.00567.

[55] C. Szegedy, S. Ioffe, V. Vanhoucke, A. Alemi, Inception-v4, Inception-ResNet and the Impact of Residual Connections on Learning, AAAI, 2017. DOI: https://arxiv.org/abs/1602.07261.

[56] G. Huang, Z. Liu, L. van der Maaten, K.Q. Weinberger, Densely connected convolutional networks, CVPR (2017) https://arxiv.org/abs/1608.06993.

证书号第8313117号

专利公告信息

发明专利证书

发 明 名 称：适用农业机械装卸转场的轨道运输机及其装卸转场方法

专 利 权 人：华南农业大学

地　　　址：510640 广东省广州市天河区五山路483号

发　明　人：李君;熊世杰;徐怀伟;黄光文

专　利　号：ZL 2023 1 0032275.2　　授权公告号：CN 115959430 B

专利申请日：2023年01月09日　　授权公告日：2025年09月30日

申请日时申请人：华南农业大学

申请日时发明人：李君;熊世杰;徐怀伟;黄光文

国家知识产权局依照中华人民共和国专利法进行审查，决定授予专利权，并予以公告。

专利权自授权公告之日起生效。专利权有效性及专利权人变更等法律信息以专利登记簿记载为准。

局长

申长雨

申长雨

2025年09月30日

证书号第23479412号

专利公告信息

实用新型专利证书

实用新型名称：一种复合吸液芯及超薄均热板

专利权人：华南农业大学;广东新创意科技有限公司

地址：510642 广东省广州市天河区五山路483号

发明人：黄光文;马宇辰;韩国跃;邓善鹏;李君;罗远强;周文杰
何柏林;李勇;陈韩荫

专利号：ZL 2024 2 2927104.9

授权公告号：CN 223500205 U

专利申请日：2024年11月29日

授权公告日：2025年10月31日

申请日时申请人：华南农业大学;广东新创意科技有限公司

申请日时发明人：黄光文;马宇辰;韩国跃;邓善鹏;李君;罗远强;周文杰
何柏林;李勇;陈韩荫

国家知识产权局依照中华人民共和国专利法进行审查，决定授予专利权，并予以公告。

专利权自授权公告之日起生效。专利权有效性及专利权人变更等法律信息以专利登记簿记载为准。

局长
申长雨

申长雨

2025年10月31日

证书号第23587034号

专利公告信息

实用新型专利证书

实用新型名称：一种角度可调的均热板传质传热性能检测装置

专 利 权 人：华南农业大学

地　　　　址：510642 广东省广州市天河区五山路483号

发　明　人：黄光文;韩国跃;马宇辰;邓善鹏;李君;罗远强;李勇;周文杰
何柏林

专　利　号：ZL 2024 2 3094295.1　　　授权公告号：CN 223611436 U

专利申请日：2024年12月16日　　　授权公告日：2025年11月28日

申请日时申请人：华南农业大学

申请日时发明人：黄光文;韩国跃;马宇辰;邓善鹏;李君;罗远强;李勇;周文杰
何柏林

国家知识产权局依照中华人民共和国专利法进行审查，决定授予专利权，并予以公告。

专利权自授权公告之日起生效。专利权有效性及专利权人变更等法律信息以专利登记簿记载为准。

局长
申长雨

2025年11月28日

华南农业大学2025批次大学生创新训练计划立项项目信息汇总表

编号	所属学院	项目名称	项目类型	拟立项级别	项目负责人	学号	项目其它成员	指导教师	职称	所属学院	备注
101	工程学院	番时捷——ROS赋能的樱桃番茄智选者	创新训练项目	国家级	李雅萱		李熙微(202421120110)，赖炜健(202321210108)，蔡佳芸(202421310201)，洪芷芸(202321120106)，郑依桐(202421110130)	杨丹彤，张亚莉	副教授，副教授	工程学院，工程学院	
102	工程学院	基于光谱技术的茶圆赤星病早期诊断研究	创新训练项目	国家级	卢洁莹		谢铖涛(202321210220)，林子怡(202421110116)，徐悦(202421110124)，陈灿民(202329220101)	吴伟斌，罗霞	教授，高级实验师	工程学院，电子工程学院（人工智能学院）	
103	工程学院	柑橘天眼—基于UAV/UGV协同赋能的柑橘果实生长智能巡检系统	创新训练项目	国家级	黄子文		吴宇航(202321210122)，陈惠志(202321810202)，李辉(202421810106)，崔桁彰(202434510206)	姜锐，施琳琳	助理研究员（自然），讲师	工程学院，工程学院	
104	工程学院	基于无人机遥感的烟草冠层实时检测与精准打顶系统研发	创新训练项目	国家级	张梓源		邹雄峰(202421810230)，林填(202421510411)，陈鸿(202421510202)	马锐军	讲师	工程学院	
105	工程学院	AgroVisor：基于多模态感知的果园智慧巡检机器人	创新训练项目	国家级	罗东宇		陈钲烨(202321120103)，吴诗瑶(202321120122)，陈嘉乐(202421210302)，陈杰(202421210202)，成祯(202421210205)	马锐军	讲师	工程学院	卢永根书院专项
106	工程学院	基于智能传感器的植保无人机雾滴漂移实时监测技术	创业实践项目	省级	卢奕铭		林峻锋(202321810115)，张舒宝(202321810130)，陈佳洲(202219110401)，陈键斌(202321810103)，潘载轩(202321140119)	吕佳，申遂愿	讲师，副教授	工程学院，工程学院	
107	工程学院	巴戟天全自动化分拣抽芯一体机	创新训练项目	省级	张烨婷		高炳业(202228110506)，王琅川(202421510326)，林佳霓(202421510316)，关双魁(202318410106)	孙振刚，孔莲芳	副教授，讲师	工程学院，工程学院	
108	工程学院	果园荔枝串果智能采收机器人开发	创新训练项目	省级	李思槿		陈业(202221510304)，曾华(202221510126)，庄善精(202321110230)，朱晨(202421510430)，杨立成(202421810224)	黄光文	讲师	工程学院	
109	工程学院	AI Agent 领航：多模态数据融合打造水稻机械化生产大数据智慧管理平台	创新训练项目	省级	陈玥		黄柔洁(202334310107)，陈正方(202334610203)，曹冰燕(202421120101)，周童(202421110229)	廖娟	助理研究员（自然）	工程学院	
110	工程学院	稻田水渠清淤机器人	创新训练项目	省级	李籽昂		吴韦翰(202321210219)，梁凯棱(202421810213)，王雨阳(202421110217)，吴小钰(202421110218)	赵润茂，胡炼	副教授，研究员（自然）	工程学院，工程学院	
111	工程学院	丰收利器·割前脱粒水稻收获机器人	创新训练项目	省级	吴子牛		陈灿辉(202221410101)，孟娟(202221410122)，贺知礼(202221410205)，张丽萍(202421410232)，苏子杰(202421410124)	杨文武	副教授	工程学院	
112	工程学院	基于气象监测与智能调度的陈皮全程生晒系统	创新训练项目	省级	何金城		邱智恒(202321810224)，杨安(202321810226)，杨子健(202321810228)，李金榜(202421810211)	周锡恩，莫嘉嗣	实验师，副教授	工程学院，工程学院	
113	工程学院	棕榈果多场景智能识别与品质分级系统设计	创新训练项目	省级	郭雨妍		冯嘉燕(202321310204)，黄荣浩(202321810210)，仲伯伦(202221510228)	李杰浩	副教授	工程学院	
114	工程学院	基于图谱融合和深度学习的名优茶芽精准识别研究	创新训练项目	省级	李子豪		叶靖锋(202221140127)，黄凯祥(202321510110)，邱子钊(202433140112)	吴伟斌，罗霞	教授，高级实验师	工程学院，电子工程学院（人工智能学院）	
115	工程学院	基于无人机的高陡边坡的复绿装置研制	创新训练项目	省级	黄文涛		陈智源(202334210104)，尹学明(202421510125)，黄立煊(202421510208)	郑峰	讲师	工程学院	
116	工程学院	基于蜚蠊触须感知的仿生垄间跟随采运机器人	创新训练项目	省级	林炳钿		曾梓颖(202421110221)，黄展鸿(202321110106)，钱梓涵(202321120118)	钟南	教授	工程学院	
117	工程学院	基于束带机构的香蕉套袋机构设计	创新训练项目	省级	林康敏		张振凯(202221510329)，李庆东(202321810215)，陶旺强(202421810121)	王慰祖，段洁利	副教授，教授	工程学院，工程学院	
118	工程学院	基于无人机航拍图的甘蔗导航播种作业评估	创新训练项目	省级	梁倩怡		李怡程(202323610213)，王浩然(202228110318)，陈长鑫(202321410203)，赖珈琦(202423220109)	张智刚	副教授	工程学院	
119	工程学院	用于荔枝采摘的绳驱机械臂的结构设计与运动控制	创新训练项目	省级	陈静宁		陈锐(202321510202)，严甜甜(202421510425)，黄冰婷(202421510404)，王奇英(202421510419)，吴章硕(202413220121)	程碧懿，王红军	副教授，教授	工程学院，工程学院	
120	工程学院	稻海智驭——再生稻种收协同高效低损智能装备	创业实践项目	省级	郭博文		郭嘉涛(202421210306)，陈炜佳(202421210304)，曹雅淇(202321110201)，曾志豪(202422210127)	曾山，卢家欢	研究员（推广型），副教授	工程学院，工程学院	
121	工程学院	基于ROS与智能监测的鸽棚自主换料机器人	创新训练项目	校级	罗康雅		包宇翔(202321120101)，张沁(202425610230)，程荣杰(202421120105)，廖一飞(202421120114)	杨丹彤，吕辉雄	副教授，教授	工程学院，资源环境学院	
122	工程学院	基于北斗定位的多功能绿豆播种管理机	创新训练项目	校级	许峻威		罗晓蓝(202321510318)，张凤仪(202421510426)，许朝阳(202421510120)	甄文斌	正高级实验师	工程学院	
123	工程学院	基于光谱技术的茶园土壤养分与重金属快速检测技术研究	创新训练项目	校级	钟培伟		施博森(202421210321)，黄靖伦(202325710405)，黄相茗(202221210213)	罗远强，高婷	副研究员（自然），高级实验师	工程学院，资源环境学院	
124	工程学院	模块化播种器研制：气固耦合效应驱动的快换排种盘的设计与验证	创新训练项目	校级	梁心怡		陈锦弘(202421210101)，江东升(202421810208)，杨家祺(202421410128)，刘雅雯(202421310216)	尹选春	副教授	工程学院	卢永根书院专项
125	工程学院	双极行星排拖拉机无极变速系统设计与制造	创新训练项目	校级	朱静怡		陈欣然(202321210203)，宋锦浩(202321210314)，陈皓月(202439020102)	肖博一	讲师	工程学院	
126	工程学院	基于mppt算法与多能互补的鼢鼠振动干扰系统	创新训练项目	校级	邓锦途		张钊珲(202421110225)，张坤鹏(202321120127)，李耿怡(202321120109)	贾瑞昌	讲师	工程学院	
127	工程学院	基于农用无人机的高效低飘粉状物料播撒装置	创新训练项目	校级	王旭楠		李响(202421510109)，孙洪(202434410118)，李心玥(202421120109)，廖康宁(202421510112)	周志艳	教授	工程学院	卢永根书院专项
128	工程学院	坡地自动导航行驶模拟试验平台系统	创新训练项目	校级	覃桦升		梁宇浩(202321310212)，吴嘉明(202321310223)，植秀炫(202421210328)	张闻宇	助理研究员（自然）	工程学院	
129	工程学院	基于乡村品牌赋能的双百行动助农产品包装设计开发	创新训练项目	校级	蓝鑫		黄韵雯(202321410109)，刘泓佐(202321410215)，毛帅(202321410116)，程乐乐(202421410203)	郭涵	副教授	工程学院	

11UMIC

“华中数控杯”
第十一届全国大学生机械创新设计大赛决赛

获奖证书

证书编号：2024111089-4

作品名称 智能化自主管理莴笋播种机

作品类型 兴农机械

获奖等级 一等奖

获奖者 学生 陈剑华、伍家东、谢 攀、邢 岳、李培基

指导老师 王慰祖、黄光文

参赛学校 华南农业大学

全国大学生机械创新设计大赛组委会
2024年7月17日

证书编号
FETIC2024030107

获 奖 证 书

参赛学校：华南农业大学

参赛作品：智能化自主管理莴笋播种机

指导老师：王慰祖 黄光文

参赛学生：陈剑华 伍家东 谢攀 邢岳 李培基

在2024年第十一届全国大学生机械创新设计大赛慧鱼组竞赛暨慧鱼工程技术创新大赛中荣获

一等奖

特发此证，以资鼓励！

主办单位：
全国大学生机械创新设计大赛组委会

承办单位：
北京中教仪人工智能科技有限公司
杭州电子科技大学

工程学院 2024 年教职工年度考核结果公示

根据各系（室）提交的教职工 2024 年年度考核初步结果，学院考核工作小组对各类考核人员结果进行了审核，经学院党委、党政联席会议讨论，确定了工程学院 2024 年教职工年度考核结果，拟报学校审批。现予以公示，公示时间从 2025 年 2 月 25 日至 2025 年 2 月 27 日止。

以下名单按姓氏笔画排序。

一、师德考核结果

参与考核的教工师德考核结果均为合格。

二、年度考核结果

（一）优秀等次人员名单（18 人）

任永志　李玉荣　李成杰　李雨桐　李莎莎　何　杰
张建瓴　陈学深　周学成　周锡恩　赵　新　钟　南
莫嘉嗣　徐凤英　黄光文　黄燕娟　廖　娟　黎志宏

（二）合格等次人员名单（109 人）

丁　凡　马巧智　马锐军　马瑞峻　王　珏　王　昱
王在满　王红军　王慰祖　文　晟　方　成　尹选春
孔莲芳　古维杰　可欣荣　卢家欢　申遂愿　付　函
冯　骁　邢　航　吕　佳　吕　娟　吕恩利　吕盛坪
朱　昀　刘天湖　刘庆庭　刘妍华　许细薇　许俊云
孙　焱　孙振刚　牟英辉　李　庆　李　灿　李亚慧
李杰浩　李继宇　杨丹彤　杨文武　杨秀丽　杨慧珠
肖博一　吴　迪　吴双龙　吴伟斌　邱亚龙　辛伯来

汪沛　汪隽　汪博文　张烨　张永博　张亚莉
张明华　张建莉　张闻宇　张焕林　张智刚　张增学
陈瑜　陈震　武涛　林冰冰　林彩霞　罗阔
罗远强　罗菊川　金济　金鸿　金莫辉　周志艳
郑峰　赵祚喜　赵润茂　胡仁俊　胡志锋　段洁利
施琳琳　姜锐　姜焰鸣　秦伟　贾瑞昌　夏红梅
徐宁　徐兴　卿艳梅　郭涵　郭晓燕　郭嘉明
涂任　涂团鹏　黄世醒　黄培奎　梅宏玉　梅慧兰
曹亚超　龚浩　蒋寅龙　辜松　程碧懿　曾山
曾文　曾小晖　曾志雄　甄文斌　蔡位子　臧英
漆海霞

（三）不定等次人员名单（2人）

贾志文　黄成杰

若对以上考核结果有异议，请向学院党政办反映。

联 系 人：李玉荣　85280783
　　　　　沈创之　85280225

工程学院
2025 年 2 月 25 日

华南农业大学
工程学院

中国教育工会华南农业大学委员会
The Trade Union of South China Agricultural University

关于工程学院部门工会换届
选举结果的批复

工程学院部门工会：

你会《工程学院部门工会换届选举结果的报告》收悉。经研究，批复如下：

同意你会换届选举结果及委员分工。具体如下：

主　　席：张亚莉　　　副 主 席：黄光文
宣教委员：郭晓燕　　　文体委员：莫嘉嗣
女工委员：吕　娟
生活（财务）委员：蔡位子
组织（青工）委员：黄成杰

此复。

中国教育工会华南农业大学委员会
二〇二四年十二月三十日

专任教师参与考核人员	54	机制教研室		金莫辉	教学科研型	讲师	11	132	12	
	55	机制教研室		甄文斌	实验技术	高级实验师	15	180	12	实验中心副主任
	56	机制教研室		段洁利	教学科研型	教授	20	240	12	
	57	机制教研室		黄光文	教学科研型	讲师	11	132	12	2年新进教工2022.04入职/学科秘书2023.01-至今
	58	机制教研室		曹亚超	教学科研型	讲师	11	132	12	2年新进教工2022.07入职
	59	机制教研室		卢家欢	教学科研型	首聘副教授	15	180	12	2年新进教工2023.09入职